1-1-1987

Structure formation in solutions of rigid polymers undergoing a phase transition/

Yachin Cohen
University of Massachusetts Amherst

STRUCTURE FORMATION IN SOLUTIONS OF RIGID POLYMERS UNDERGOING A PHASE TRANSITION

A Dissertation Presented

by

YACHIN COHEN

Submitted to the Graduate School of the
University of Massachusetts in partial fulfillment
of the requirements for the degree of

DOCTOR OF PHILOSOPHY

February 1987

Polymer Science and Engineering

STRUCTURE FORMATION IN SOLUTIONS OF RIGID POLYMERS

UNDERGOING A PHASE TRANSITION

A Dissertation Presented

by

YACHIN COHEN

Approved as to style and content by:

Edwin L. Thomas, Chairperson of Comittee

Richard J. Farris, Member

Murugappan Muthukumar, Member

Richard S. Stein, Member

Edwin L. Thomas, Department Head

Polymer Science and Engineering

ACKNOWLEDGEMENTS

I wish to thank Professor Edwin L. Thomas for guiding me in the course of this research, and for his support and encouragement. I also wish to thank Professors Richard S. Stein, Richard J. Farris, and M. Muthukumar for serving on my dissertation committee and for their interest and advice.

I thank Professor Y. Talmon of the Technion, Israel, for his help and encouragement. I gratefully acknowledge helpful discussions with Dr. C.G. Vonk and Professors E.D.T. Atkins and P.A. Monson.

It is a pleasure to thank my friends and colleagues for creating a stimulating and supportive environment. I am grateful for the friendship and assistance of: J. Brady, D. Gobran, H. Marand, D. Martin, L. Raboin, Drs. A. Boudet, T. Granier, C. Henkee, D. Kinning, B. Wood, and all the members of my research group. I wish to thank Herb Frost and Steven DeTeresa for their friendship and counsel. Many thanks to my friends Ravi Saraf, Yang Chen, and Paula Hahn for friendly support and constructive criticism. I would like to thank Dianne Peterson for typing this manuscript.

This work was supported by the Air Force Wright Aeronautical Laboratories and the Air Force Office of Scientific Research. I gratefully acknowledge helpful interactions with the scientists of the polymer branch at AFWAL. Special thanks are extended to Dr. W.W. Adams for his advice and encouragement.

My deepest feelings are expressed to my family--the source and object of any accomplishment I may have.

ABSTRACT

STRUCTURE FORMATION IN SOLUTIONS OF RIGID POLYMERS

UNDERGOING A PHASE TRANSITION

February 1987

Yachin Cohen, B.S., Technion-Israel Institute of Technology

M.S., Weizmann Institute of Science

Ph.D., University of Massachusetts

Directed by: Professor Edwin L. Thomas

The development of morphology, when solutions of rigid polymers are transformed from the liquid to the solid state, was studied in two particular cases: coagulation of a monodomain nematic solution and gelation of a dilute isotropic solution. Direct observation of the morphology by electron microscopy (E.M.) was augmented by measurements of small-angle X-ray scattering (SAXS). A theoretical framework for the analysis of SAXS measurements from oriented systems using a slit-collimated incident beam was developed.

The first case is realized in the coagulation stage of the spinning process of high performance fibers and films from solutions of rigid macromolecules. A monodomain nematic solution of poly(p-phenylene benzobisthiazole) [PBT] in polyphosphoric acid [PPA] undergoes a transition to the solid state by the action of a non solvent (water). The morphology of coagulated PBT fibers and films was studied by E.M. and SAXS, after impregnation with an epoxy resin. The basic structure formed during coagulation was observed to be an interconnected network

of oriented microfibrils, having a typical width about 100Å and irregularly shaped cross-sections. The mechanism of structure formation is postulated to be nucleation and growth, whereby the width of the microfibrils is controlled by the nucleation density.

A novel crystal-solvate phase was formed when the PBT/PPA solution is coagulated in a mixture of phosphoric acid (85%) and water. It is a three-dimensionally ordered, solid phase which melts at 250°C. The crystal-solvate is composed of PBT chains and PPA oligomers packed parallel to each other.

For the second case, gelation of an isotropic solution of poly(γ-benzyl-L-glutamate), induced by a decrease in temperature, was studied. A disordered cluster of microfibrils, on the length scale of 10^2-10^3Å, was observed by E.M. using a freeze-fracture replication technique. In the same range, SAXS measurements indicated that the morphology can be described as a self-similar fractal of dimensionality about 2.5. Direct visualization by E.M. of rapidly frozen thin films revealed inhomogeneities on the length scale of 0.5-5.0μm, which reflect an inhomogeneous distribution of the microfibrillr clusters. These observations suggest that gelation occurs by a diffusion-limited aggregation process.

TABLE OF CONTENTS

LIST OF TABLES

LIST OF FIGURES

CHAPTER I

INTRODUCTION

1.1 An Overview of the Dissertation and Its Objectives

The utilization of rigid polymers in structural and connective elements is abundant in nature, from the networks of microfilaments and microtubules of the cytoskeleton--the structural foundation of individual cells, to the network of chitin microfibrils comprising the cuticle of insects--the elaborate body and wings which are considered to be the secret of their evolutionary success. It is therefore not surprising that synthetic rigid polymers have been developed, from which high performance fibers and films can be fabricated.

The success of both natural and synthetic materials in fulfilling their structural function lies in the combination of chain rigidity on the molecular level, and suitable arrangement of chains on the supramolecular scale. The nature and origin of the morphological features at the scale of 50-1000Å are not well understood. In many cases involving both natural and synthetic rigid polymers, the microstructure is formed by a phase transition from a solution to a solid state having the desired structure and properties. Such phase transitions are the focus of this dissertation.

The objective of this thesis is to study the microstructure formed as a result of a phase transition in two well-defined cases of solutions of a rigid polymer. A correlation of the morphology with the phase equilibria and the kinetics of the phase transition is sought.

The state of the solution prior to the transition is an important consideration. Solutions of rigid polymers exhibit a wide variety of mesophases and textures which may influence the formation of structure in a complicated way. In this thesis the two simplest cases are considered: an isotropic solution and a monodomain nematic solution.

A sound microstructural characterization is best approached by combining the direct visualization, provided by electron microscopy, albeit perturbed by the method of sample preparation, with appropriate scattering measurements, which do not uniquely determine the structure and require a model for interpretation. The guiding principle is therefore to utilize specific electron microscopy techniques suitable for the systems under study to provide structural models which can be tested by small-angle x-ray scattering (SAXS) measurements. The experimental techniques used are summarized in Chapter II. The theoretical framework for the interpretation of SAXS measurements from oriented fibrils is derived in Chapter III.

The major part of the thesis is a study of the coagulation stage in the spinning process of poly(p-phenylene benzobisthiazole) (PBT) fibers and films, which have been developed under the U:S. Air Force Ordered Polymers Program. Previous studies were centered on the heat treatment and drying stages of the spinning process, and related the excellent tensile properties achieved by optimization of these processes to an increase in chain orientation along the fiber axis and to improved lateral packing between neighboring chains. Yet the compressive properties remain relatively poor and cannot be enhanced by either post-treatment.

It is in the coagulation stage that the monodomain nematic solution undergoes a transformation to the solid state by the action of a non-solvent. In Chapter IV, the basic structural elements of PBT fibers and films formed in the coagulation process, which may be largely responsible for their compressive properties, are characterized. An intermediate crystal-solvate phase which may occur during coagulation by co-crystalization of polymer and solvent is described, and the effect of its formation on the final microstructure is discussed.

Synthetic polypeptides behave as rigid rods when dissolved in solvents which induce a helical conformation of the polymer. Such solutions are useful model systems due to the availability of polymers with well characterized molecular weights having reasonably narrow distributions. Solutions of poly(γ-benzyl-L-glutamate) (PBLG) in helicogenic solvents exhibit a gelation transition upon a decrease in temperature from both isotropic and ordered solutions, even at concentrations as low as 0.05%. The structure of the gel, as well as the mechanism of its formation, are not well understood. The morphology of a PBLG gel formed from a dilute isotropic solution is characterized in Chapter V. Cryogenic methods allow observation of the gel microstructure by electron microscopy, and are augmented by SAXS measurements.

Chapter VI concerns the relationship between phase equilibria, the kinetic mechanism of the phase transition, and the ensuing morphology. A nucleation and growth mechanism, controlled either by nucleation or diffusion, as well as spinodal decomposition, are considered with respect to both gelation of an isotropic PBLG solution and coagulation of

a monodomain nematic PBT solution. The relevance of the crystal-solvate phase to structure formation in both cases is discussed.

The conclusions of this study are summarized in Chapter VII, as well as recommendations for future studies.

1.2 Phase Equilibria in Solutions of Rigid Polymers

1.2.1 The Lattice Theory of Flory

Due to their rod-like nature, a solution of rigid polymers can become ordered above a certain critical concentration. The ordered, liquid crystalline phase is characterized by a high degree of orientational order but very little positional order, and is thus intermediate between the isotropic fluid and crystalline solid phases. Early theories due to Onsager [1] and Isihara [2] were able to predict the critical concentration and pointed out the possibility of a first order transition based on purely entropic grounds, in the absence of attractive interactions between the rods. In 1956 Flory presented a lattice model for solutions of semiflexible [3] and rigid [4] polymers by which the equilibrium between the isotropic and ordered phases may be predicted as a function of the molecular axial ratio and temperature. This theory was found to be in agreement with experimental results of several different systems and has been subsequently refined and extended, as reviewed recently by Flory [5]. For the purposes of this thesis, the original theory [4] is sufficient.

Flory considered the rigid molecule as situated in a cubic lattice having one of its axes parallel to the direction of preferred

orientation, and the cells of which have a dimension equal to the width of the rod-like polymer. To consider different orientations of a rod, it is divided into submolecules which are parallel to the preferred axis as shown in Figure 1.1. The number of submolecules (y_i) is determined by the inclination angle of the rod relative to the axis of preferred orientation (Ψ_i):

$$y_i = x\sin\Psi_i \tag{1.1}$$

where x is the axial ratio of the rod-like polymer. An average disorientation parameter can be defined as

$$\bar{y} = (\frac{4}{\pi}) \; x \; <\sin \Psi_i> \tag{1.2}$$

which serves as an order parameter whereby $\bar{y}=x$ denotes an isotropic system ($<\sin\Psi>=\pi/4$), and $\bar{y}=1$ denotes a state of perfect order.

The entropy of mixing is calculated by evaluating the total partition function for a system of n_p rod-like polymer molecules and n_s solvent molecules. It is given as a product of a combinatorial term and an orientational term. The former accounts for the number of configurations available for placement in the lattice of n_p rods having an average orientation $\bar{y}$, and n_s solvent molecules. The latter term accounts for the number of orientations available for each rod. The configurational entropy for a given rod concentration is shown to be maximized at an average disorientation parameter $\bar{y}$ which satisfies:

$$v_p = [x/(x-\bar{y})][1-\exp(-2/\bar{y})] \tag{1.3}$$

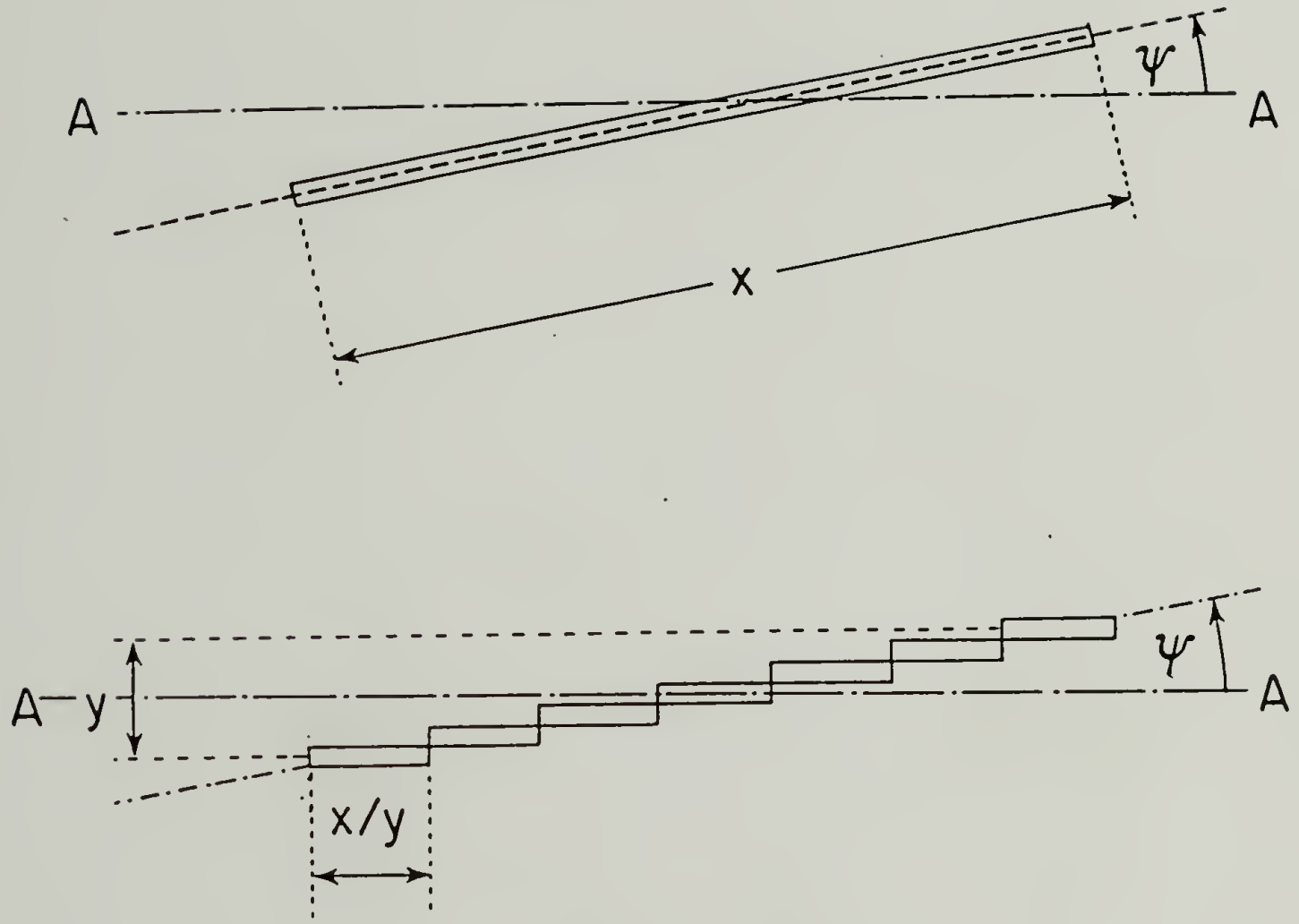

Figure 1.1. Representation of a rod by means of submolecules in a lattice (Following P. J. Flory, ref. [4]).

where v_p is the polymer volume fraction

$$v_p = xn_p/(n_s+xn_p) \tag{1.4}$$

A useful approximation for the critical concentration for the incipience of metastable order (v_p^*) is obtained from the minimal volume fraction for which a solution to equation (1.3) exists:

$$v_p^* = (8/x)(1-2/x) \tag{1.5}$$

If the interactions between the rods to not depend on their mutual orientation, the enthalpy of mixing can be taken into account using the Flory-Huggins χ-parameter, as in the case of flexible polymers [6]. The free energy of mixing is thus given as:

$$\Delta G_m/kT = n_s \ell n v_s + n_p \ell n v_p - (n_s+yn_p)\ell n[1-v_p(1-y/x)]$$
$$-n_p[\ell n(xy^2)-y+1] + \chi x n_p v_s \tag{1.6}$$

In the case of perfect alignment ($\bar{y}=1$) equation (1.6) reduces to that of a regular solution (ideal entropy), whereas for complete disorder ($\bar{y}=x$) it reduces to the Flory-Huggins equation for a solution of a flexible polymer [6] with an additional disorientation entropy term. The chemical potentials of the solute and solvent in the isotropic and ordered phases are obtained by differentiation of equation (1.6), using the value of $\bar{y}$ that satisfies equation (1.3) for the ordered phase or $\bar{y}=x$ for the isotropic phase. The coexistence curves are derived by equating the chemical potentials of each component in the isotropic and ordered phases.

The phase diagram predicted by Flory's 1956 theory, as shown in Figure 1.2 for an axial ratio x=100, exhibits unique features. At

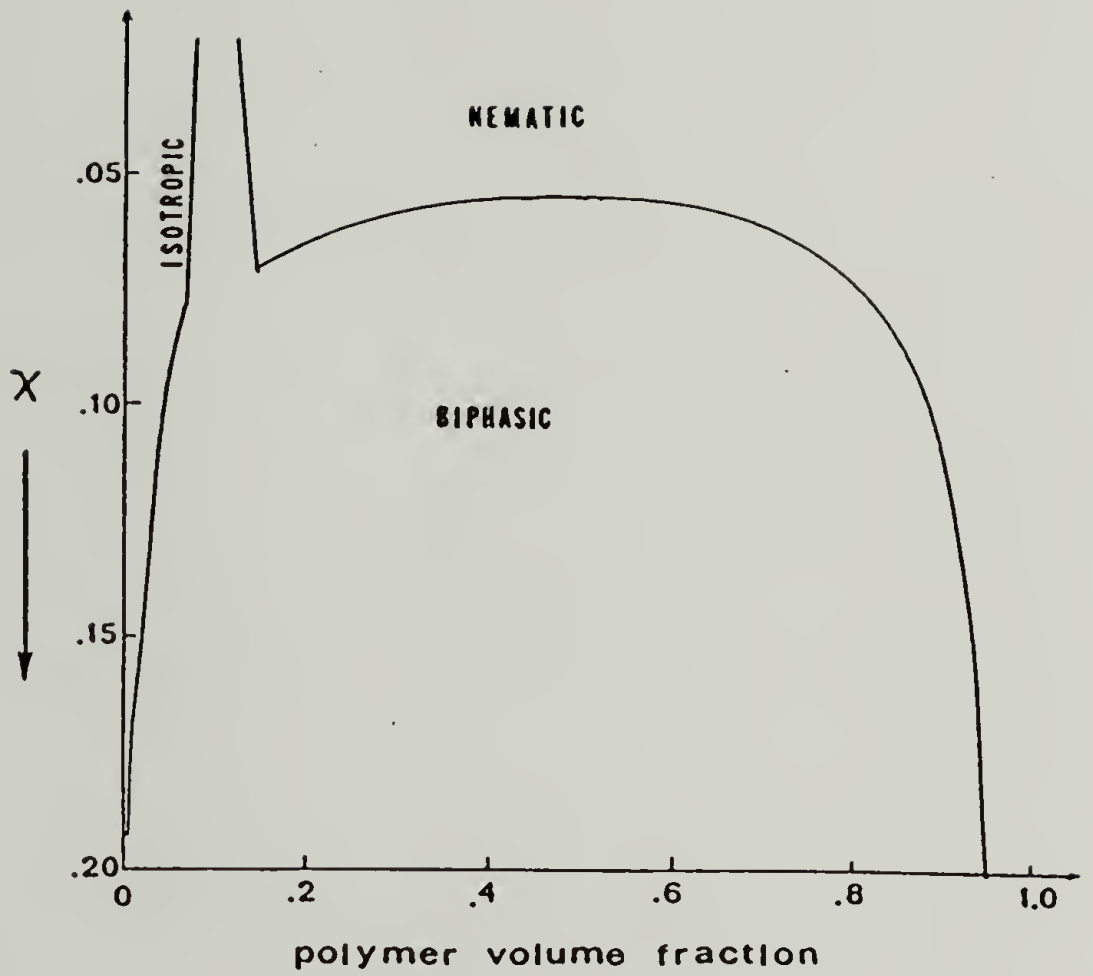

Figure 1.2. Phase diagram predicted by Flory's theory (1956), for a solution of a rigid polymer, having axial ratio x=100.

negative χ (or high temperatures) a narrow biphasic region ("chimney region"), the boundaries of which depend on the axial ratio but very little on χ, abruptly changes at slightly positive χ (lower temperature) to a wide biphasic region separating a very dilute isotropic phase and a concentrated ordered phase.

1.2.2 Modifications Due to Crystallization at High Polymer Concentrations

Flory's original theory [4] and its subsequent modifications were successful in predicting the phase equilibria of several experimental systems at low polymer concentrations [5]. Krigbaum and Ciferri [7,8] have recognized the importance of a transition from the liquid phase (either isotropic or ordered) to a crystalline phase, in view of the extremely high melting temperature of rigid-polymer crystals. In particular, the concentrated ordered liquid phase, which is predicted by Flory's theories to exist at the boundary of the wide biphasic region, is considered to be metastable relative to an ordered crystalline phase. Melting point depression relationships, of both ordered and isotropic solutions of rigid polymers, have been deduced. For example, the phase boundary of the ordered solution with respect to formation of a crystalline solid has been predicted [7], based on Flory's original theory [4] to follow:

$$\frac{1}{T_m} - \frac{1}{T_m^\circ} = \frac{kx}{\Delta H_f}\left\{-\frac{1}{x}\left[\ell n \frac{V_p}{x} + (y-1)V_p - \ell n y^2\right] + 2 - \chi V_s^2\right\} \quad (1.7)$$

where T_m° and ΔH_f are the melting temperature and the heat of fusion per mole of the crystaline polymer, and y conforms to equation (1.3). This

relation has been found to be in qualitative agreement with the behavior of solutions of poly (benzamide) [PBA] [9].

Papkov and coworkers [10,11] have promoted the concept of a crystal-solvate phase. This is a crystalline solid phase formed by co-crystallization of polymer and solvent molecules in a distinct composition and crystal structure. The crystal-solvate phase has been observed in many solutions of rigid polymers [11]. In general several crystal-solvate phases, having different polymer/solvent compositions, may be formed in a particular system. Gardner et al. [12] reported the phase behavior and crystal structure of poly(p-phenylene-terephathalamide) [PPTA]/sulfuric acid crystal solvates. The crystal transformations and thermal behavior of the PBA/N,N-dimethyl acetamide/LiCl system have been described [13,14]. Investigations of the crystal solvate phase of PBT will be described in section 1.3.2. These studies indicate that the crystal solvate phase has much lower melting temperature and heat of fusion as compared to the crystalline polymer, the melting of which is often inaccessible due to the onset of decomposition at very high temperatures. A generalized phase diagram [10], in which equilibria with respect to a crystalline polymer phase as well as a crystal solvate phase are superimposed on the liquid-liquid phase equilibria predicted by Flory [4], is shown in Figure 1.3. For clarity, only one crystal-solvate phase is considered.

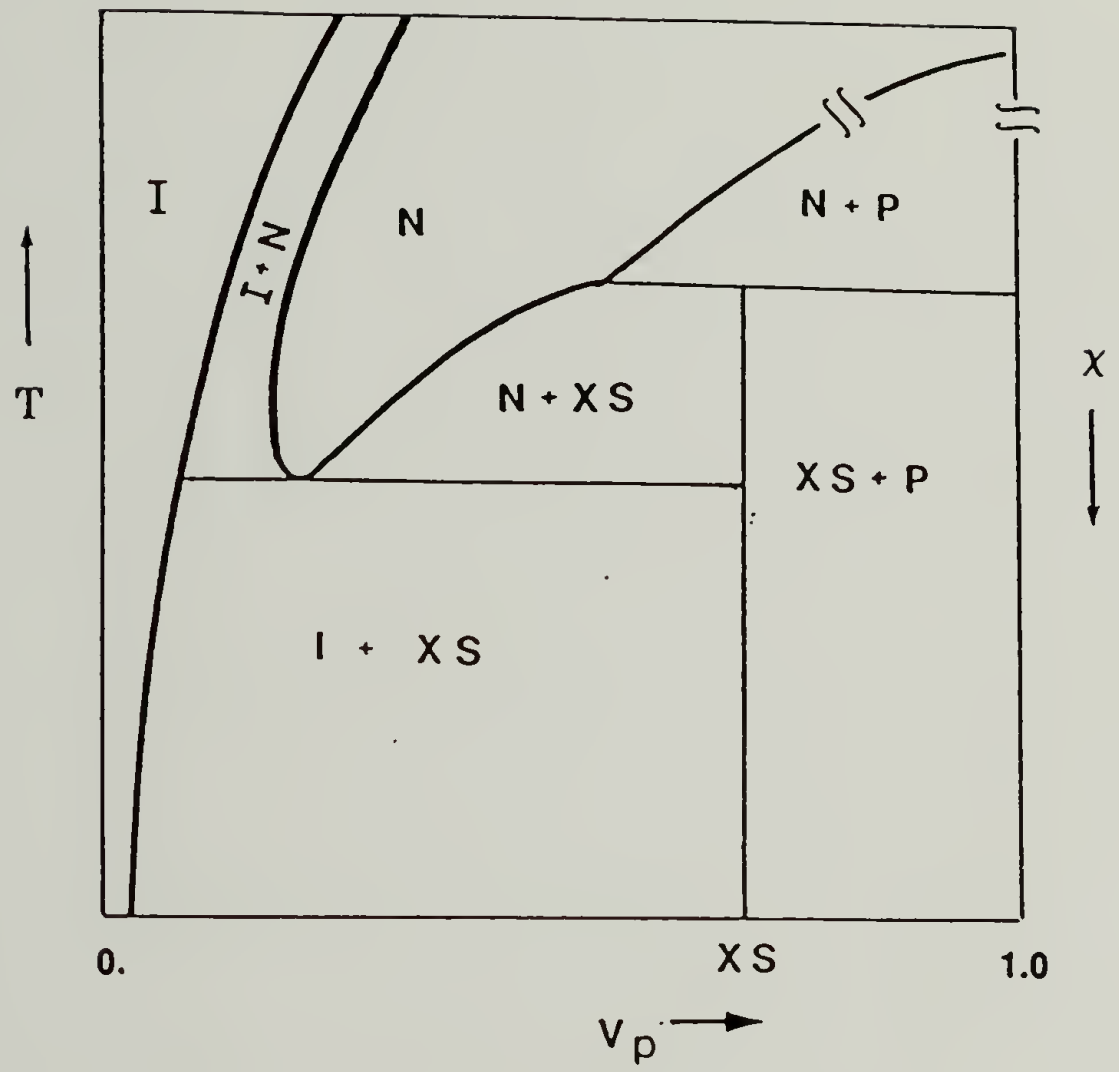

Figure 1.3. A schematic phase diagram of a solution of a rigid polymer. I - isotropic solution, N - nematic solution, XS - crystal-solvate, P - crystalline polymer, v_p - polymer volume fraction.

1.3 Poly(p-phenylene benzobisthiazole)-PBT

1.3.1 A Review of Processing, Structure and Properties of PBT Fibers and Films

PBT has the chemical structure given below:

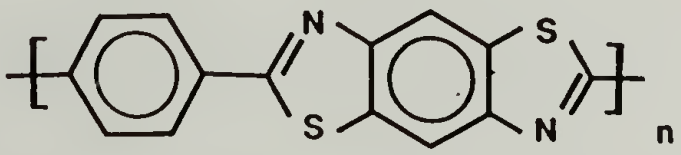

It is synthesized by condensation polymerization in polyphosphoric acid (PPA) [15]. The Mark-Howink relation for PBT in methane-sulfonic acid (MSA) has been reported as [16]:

$$[\eta] = 1.25 \times 10^{-7} M_w^{1.8} [d\ell/g] \qquad (1.8)$$

Polymers having intrinsic viscosities up to 47 dℓ/g, corresponding to a molecular weight about 58,000, have been synthesized. A molecular weight distribution having $M_w/M_n \sim 1.3$ has been reported [17]. A lower bound of its persistence length in chlorosulfonic acid (CSA) has been estimated as 640Å [18], thus PBT in solution behaves essentially as a rigid rod-like molecule. PBT dissolves only in strong acids (PPA, MSA, CSA), in which the nitrogen atom in the PBT repeat unit is protonated to form a rod-like polycation [16,19]. Solutions of PBT in such acids exhibit an isotropic-nematic phase transition, which has been observed by optical microscopy and viscosity measurements [20-24]. The shape of the coexistence curves is characteristic of the narrow biphasic region, the ratio of the polymer concentration in the coexisting phases being about 1.04 [20]. The coexistence curves shift towards higher polymer concentrations at elevated temperatures [20,21].

Fibers and films are spun from PBT solutions in a process which involves a succession of operations. The polymer solution is extruded through a die into an air gap, where it is extended in an elongational flow, and is introduced into a coagulation bath, where a phase transition to the solid state is induced by a non solvent (typically water). The coagulated fiber or film is then dried (at which point it is termed "as-spun") and subsequently heat-treated under tension [25]. The ability to induce elongational flow in PBT/PPA solutions prior to coagulation is essential to maximize the degree of uniaxial orientation of the PBT molecules. Spin draw ratios up to 30:1 have been achieved, thus ensuring that coagulation takes place in essentially a monodomain nematic state.

The crystal structure of PBT has been studied by x-ray diffraction and electron microscopy [25-28]. The diffraction pattern of heat treated fibers exhibits sharp equatorial reflections and diffuse meridional streaks, which have been interpreted as resulting from an ordered lateral packing of the polymer chains with random translational disorder along the chain axis. Both a primitive (Z=1) and nonprimitive (Z=2) monoclinic unit cells have been proposed for the lateral packing of PBT chains [26,27], which are slightly different versions of a basic primitive cell having the following dimensions [28]:

$$a = 5.97\text{Å} \qquad b = 3.62\text{Å} \qquad c = 12.45\text{Å} \qquad \gamma = 95.2°$$

Lattice images of PBT have been obtained [29], revealing fringes originating from equatorial (5.97Å) and meridional (12.45Å) reflections. This indicates the existence of regions having a high degree of coherent

packing of chains. The observation of lattice fringes originating from meridional reflections is evidence that these regions have a three-dimensional crystalline order. The distribution of intensity along the layer lines has been shown recently to be inconsistent with the model of a random axial shift disorder. New models are currently being evaluated [30].

PBT fibers are noted for their excellent tensile properties, as well as high thermal stability. Tensile modulus greater than 300 GPa and strength exceeding 3 GPa have been reported [31,32], yet the transverse and compressive properties are considerably lower. The compressive strength is less than 0.3 GPa, failure invariably occurring by buckling [33].

Previous studies have focused on the heat treatment [31] and drying [32] processes, where under suitable conditions a twofold increase in the tensile modulus and tensile strength has been achieved. This has been attributed to enhancement of the chain orientation along the fiber axis and to better lateral packing of the chains. The lateral dimension of regions of coherently scattering PBT chains has been estimated by dark-field electron microscopy imaging [34] and from the breadth of the equatorial x-ray diffraction maxima [35]. An increase in the dimension of lateral coherence from 10-20Å in the as-spun state to about 100Å after tensional heat treatment has been observed. Since the compressive strength in the as-spun and heat-treated states is comparable [32,33], it is evident that the degree of lateral packing, which is determined in

the drying and heat-treatment processes, does not control the compressive properties.

In a study of the spinning process of PBT fibers from PPA solutions it has been observed that the diameter of the solution stream does not change appreciably during the coagulation process, whereas it decreases during drying to about 30% of its value in the wet-coagulated state [33]. Despite the fact that the wet-coagulated fiber may contain more than 90% water, its ability to sustain a tensile force is equivalent to that of the dry (as-spun) fiber [33,35]. This indicates that the basic structural features responsible for the mechanical properties are set in the coagulation process.

1.3.2 The "Crystal-Solvate" Phase-PBT/Solvent Co-crystals

The formation of the crystal-solvate phase in solutions of PBT in MSA was first studied by Frost [37,38]. A dilute, isotropic solution of low molecular weight PBT ($[\eta] = 2 d\ell/g$ in MSA) was allowed to coagulate slowly between a microscope slide and a cover glass by absorption of atmospheric moisture. After several days a solid phase developed, in the form of spherulites observed by optical microscopy, as shown in Figure 1.4. As the principal polarizability of PBT is along the chain axis, the fact that the spherulites are optically negative indicates that the PBT chains are oriented in the tangential direction. This is verified by electron microscopy of the system after removal of the acid, in which a lamellar morphology is observed as shown in Figure 1.5. Electron diffraction indicates that the extended PBT chains are packed with the chain axis perpendicular to the lamella.

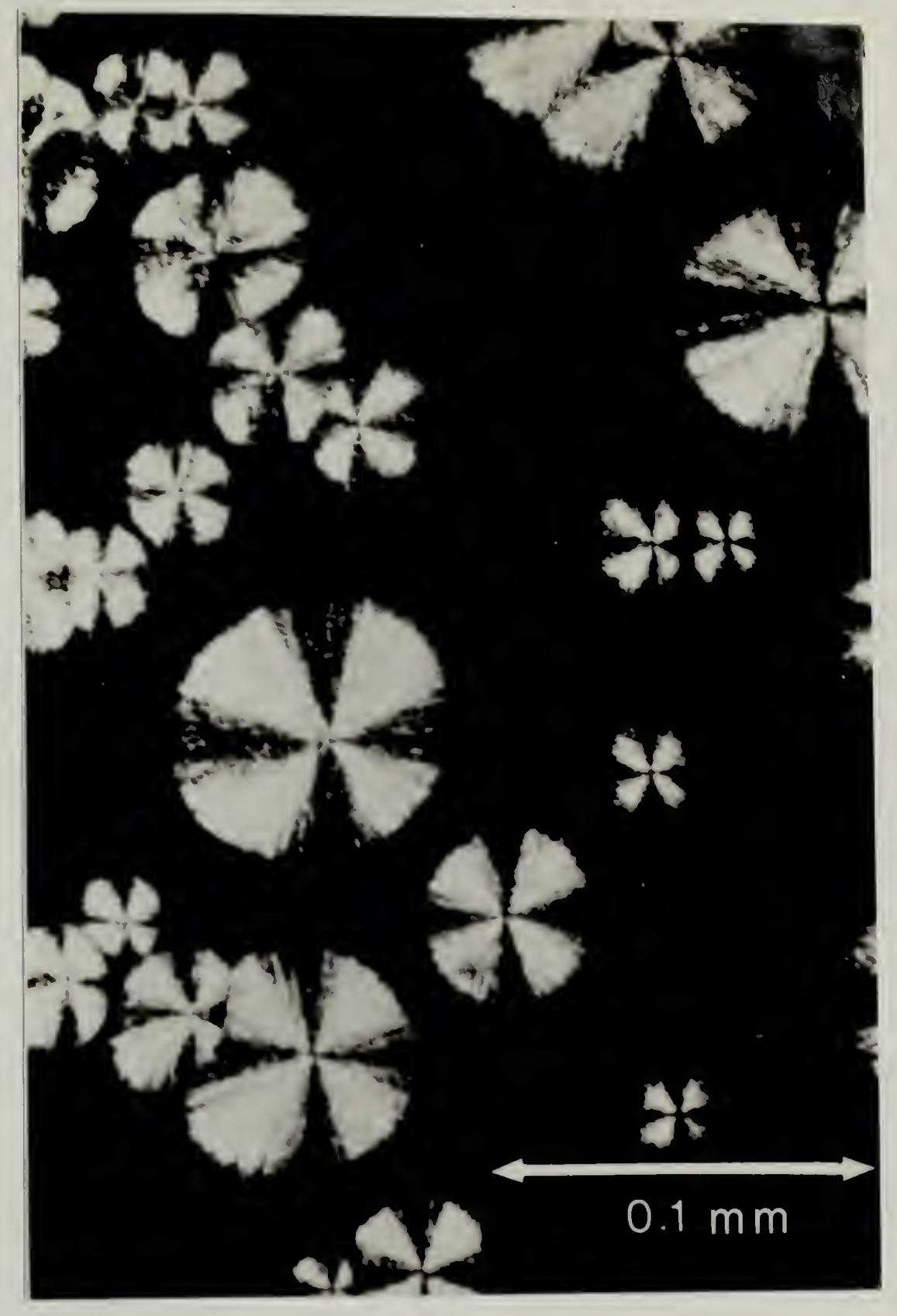

Figure 1.4. Optical micrograph of spherulites formed by slow coagulation of an isotropic solution of PBT in MSA, viewed between crossed polarizers (from ref. [37]).

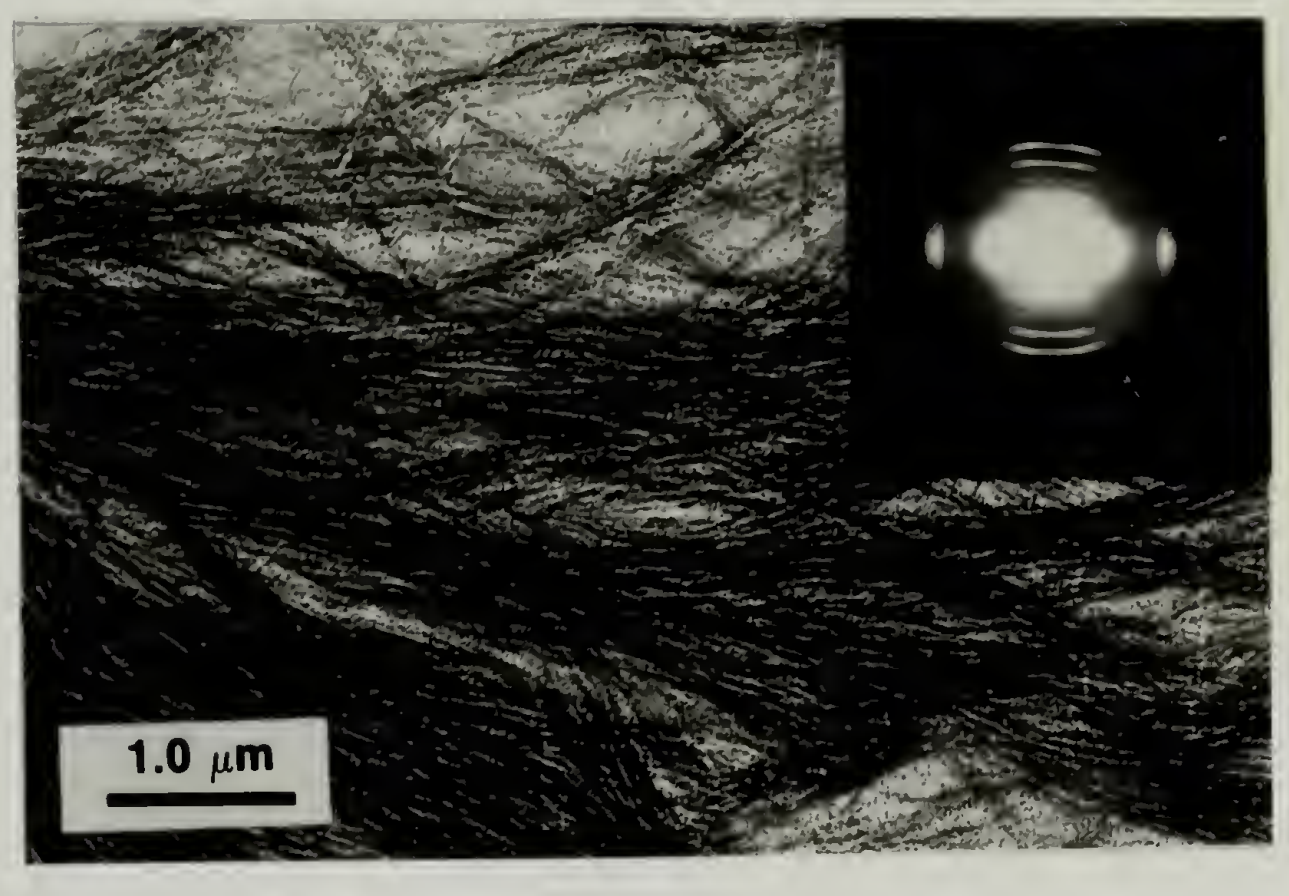

Figure 1.5. Electron micrograph of the slowly coagulated PBT. Inset: electron diffraction pattern taken from an area in the center of the image (from ref. [37]).

The nature of the phase formed in the slow coagulation experiment has been deduced on the basis of its thermal transitions, and from its x-ray diffraction pattern. Three endothermic transitions were observed between 90°C and 240°C, in the slowly coagulated PBT/MSA/water system, by differential scanning calorimetry (DSC). Corresponding transitions were observed by optical microscopy using a hot stage. Solid PBT fibers or films do not exhibit thermal transitions below about 650°C [25].

The X-ray diffraction pattern of the slowly coagulated material exhibits rings, characteristic of an unoriented material, the spacings of which are different than those of the PBT fiber diffraction pattern. The observed spacings can be fitted to a monoclinic unit cell having the following dimensions [31]:

$a = 6.5\text{Å}$ $b = 5.3\text{Å}$ $c = 12.5\text{Å}$ $\gamma = 101°$

These dimensions indicate a larger unit cell in the slowly coagulated PBT-MSA-water system as compared with solid PBT.

On the basis of these results, it has been concluded that the solid phase formed by slow coagulation is a crystal-solvate phase, i.e., co-crystals of the protonated PBT and the acid anion [37,38].

1.4 Poly(γ-benzyl-L-glutamate) - PBLG

1.4.1 Phase Equilibria and Gelation in PBLG Solutions

Studies of PBLG have had an essential role in understanding the structure and solution properties of polypeptides and lyotropic polymers in general. The α helix model of Pauling was first verified by crystallographic studies on PBLG fiber by Perutz [39], and liquid crystallinity

in a synthetic polymer solution was first observed by Robinson with PBLG [40]. Since the early studies, PBLG was found as a most useful model system for rigid-rod polymers [41].

PBLG can be synthesized, with a narrow molecular weight distribution, by anionic polymerization using the N-carboxyanhydride method. The chemical structure of PBLG is given below.

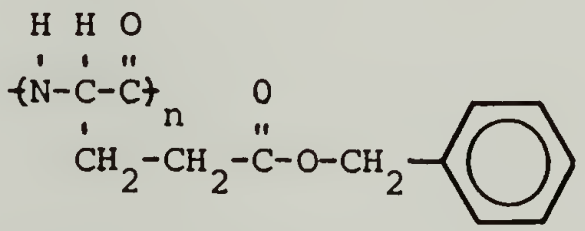

In very polar solvents, such as halogenated carboxylic acids, PBLG assumes a coiled conformation, whereas in moderately polar solvents a helical conformation is favored [41]. SAXS measurements by Luzzati et al. [42] suggest that the type of helix (3_{10} or α helix) is both solvent and concentration dependent. The helical conformation, stabilized by intramolecular hydrogen bonds, affords a rigid-rod nature to the molecule, as verified in many experiments such as viscosity and light-scattering measurements [43]. At higher molecular weights and increased temperature some flexibility of the helix is observed [41].

The rods are rendered soluble by the mixing of the flexible side groups with the solvent. The presence of benzyl side groups together with polar end groups in the rods allows for different molecular aggregation even in dilute solution. While the rods are molecularly dispersed in dimethyl formamide (DMF), benzyl alcohol or m-cresol, evidence exists for aggregation in a side by side antiparallel manner in benzene

and dioxane [44], or head to tail aggregation in ethylene dichloride and toluene [45].

At higher polymer concentrations, PBLG solutions form a cholesteric liquid crystalline phase with a relatively long pitch (up to 100 um), as evidenced by the characteristic "fingerprint" pattern observed by optical microscopy between crossed polarizers [40]. A scattering peak, due to the inter-rod spacing in the cholesteric phase, is observed in SAXS measurements, and the peak position shifts to smaller spacings as the polymer concentration increases [42]. The phase diagram of PBLG in DMF exhibits both the narrow and the wide biphasic regions [46] and was found to be in good agreement with Flory's theory [3,5].

At even higher concentrations (e.g., above about 20% in DMF) formation of a so called "complex" phase, characterized by turbid appearance and sharp x-ray reflections independent of concentration, has been reported [42]. The crystal structure of this phase, in which the unit cell is larger than that of the solid PBLG fiber, has been determined [47]. It involves parallel single helices enjoined by a complex stacking of benzene rings from the side groups of neighboring helices. The nature of this phase is still controversial. Russo and Miller [48] attributed its formation to the presence of water, a non-solvent, in the PBLG/DMF system.

Cooling a PBLG solution, from either the isotropic or liquid crystalline phase, results in formation of a self-supporting gel [49-53]. Gelation may occur at polymer concentrations as low as 0.05% (w/w) [49,50,52], and it can be induced by addition of a non solvent [48,50,

51]. Gelation of solutions of PBLG in DMF, DMF/water and toluene were studied by Miller and coworkers [48-51], and in benzyl alcohol by Sasaki et al. [52,53] and Murthy et al. [54], who also reported the dependence of the gelation temperature on polymer concentration and molecular weight, in the respective systems. Miller suggested that gelation is associated with phase separation in the wide biphasic region [49].

Rheological measurements indicated the predominantly elastic nature of PBLG gels: the storage modulus, in oscillatory shear deformation, is much larger than the loss modulus, and is independent of frequency [50, 51,54]. The modulus of gels formed from the isotropic phase was fairly independent of temperature, up to the vicinity of the transition temperature. Different results were reported for the concentration dependence of the modulus. In the concentration range of 0.25% (w/w) in toluene to 75% in DMF, the modulus appears to be nearly constant, scaling with the concentration to a power less than 0.2 [50]. For gels of PBLG ($MW \sim 1.5 \times 10^5$) in benzyl alcohol, the modulus was reported to scale with polymer concentration (C) as $C^{1.3}$ below 0.5% (w/w) and $C^{2.6}$ between 0.5% and 10% (w/w) [52]. In any case the scaling power was much less than C^5, as predicted by Doi and Edwards [55-57] for an entangled "log-jam" of rigid rods.

More pronounced effects of temperature and concentration were observed in gels having polymer concentrations in the vicinity of the isotropic-cholesteric transition in the high temperature liquid state [54]. The modulus of the gel went through a maximum near the critical concentration of the transition, reflecting a memory effect for the

state of high temperature phase from which it was formed. Evidently a unique morphology, which is controlled by the kinetics of the gelation process, is responsible for these rheological characteristics.

1.4.2 The Morphology of PBLG and Its Gels

A wide variety of morphologies have been observed in PBLG precipitated from very dilute solutions, which strongly depend on the nature of the solvent [58,59]. Of interest here are the fibrillar morphologies observed to be composed of microfibrils [58] and "star-shaped" clusters in which several fibrils project radially from a common center [59].

The morphology of PBLG gels in DMF [60] and toluene [49] has been visualized by electron microscopy using a freeze-fracture replication technique. A network of interconnected microfibrils, about 100Å in width, has been observed [60]. Miller has proposed that such a morphology is formed by a spinodal decomposition mechanism in which separation into dilute isotropic and concentrated ordered phases, which are interconnected, is followed by solidification of the polymer in the concentrated phase. Thus a stable interconnected network is obtained, the structure of which is controlled by the spinodal decomposition process. This model is supported by time-resolved light scattering measurements in which an exponential increase in the scattered intensity is observed initially, whereas an apparent radius of gyration remains constant [51,61]. Observation of the gelation process by optical microscopy using fluorescent-labelled PBLG indicated the appearance of large polymer-rich domains which occupy a larger fraction of the solution than

warranted by the polymer concentration [61]. This has been interpreted as a nucleation-free phase separation of isotropic phases. It is then postulated that the polymer-rich isotropic phase undergoes a glass transition as its concentration increases, thus frustrating further separation or ordering. The gel is thus envisaged as composed of interconnected isotrophic phases, the higher concentration one being in a non-equilibrium glassy state.

Sasaki et al. [52,53] observed that the melting temperature and X-ray diffraction patterns of PBLG gels in benzyl alcohol were dependent on the method by which the gels were formed. Quenching a liquid crystalline solution to small undercooling results in a gel whose diffraction pattern is interpreted as that of a crystal-solvate. Repeated cycles of quenching to low temperature and heating to near the melting point results in a gel of higher melting point and whose diffraction pattern is interpreted as that of crystalline PBLG.

The morphological issues, especially in the case of gels formed from dilute isotropic solutions, are thus:

(a) What is the nature of the local order on the scale of 100Å? Are the chains disordered or packed in a fibrillar crystal (or crystal-solvate)?

(b) Are there inhomogeneities on a larger scale (1-10 μm), and what is their origin?

The basic enigma which underscores the morphological questions is the mechanism of the gelation process.

CHAPTER II

EXPERIMENTAL METHODS

2.1 PBT

2.1.1 Materials and Processing

PBT solutions in polyphosphoric acid (PPA), its polymerization medium, were obtained from Dr. J. Wolfe of Stanford Research Institute, who furnished the characterization of intrinsic viscosity and concentration. All solutions were in the nematic state.

Fibers were spun by L. Pottick [32] by extrusion through a circular die 0.18mm in diameter, extension in an air gap and coagulation in water. The wet fibers were kept submerged under water for further studies. Using the same apparatus, films were extruded through a rectangular die, 1.0mm in width, by S. Wicklieff.

Uncoagulated samples of an oriented PBT/PPA solution, in a monodomain nematic state, were obtained from Foster Miller Inc. The solution was extruded through a tubular die having a gap of 2.0mm and diameter 38.1mm. The extruded tube, after a 20:1 extension, was collapsed between teflon sheets by the take-up rollers, and kept subsequently dessicated below 0°C.

Details of the PBT solutions used and their processing are given in Table 2.1.

The oriented PBT/PPA solution was used to study the morphology formed under different coagulation conditions. Segments of the oriented film, about 5cm long, were coagulated either in water or in 85%

Table 1. Processing Conditions of PBT Solutions

Type	Fiber	Film	Film
PBT/PPA Solution			
SRI Lot No.	2859-64	2895-64	5103-53
Concentration (wt. %)	5.5	5.5	13.7
Intrinsic velocity[a] (dℓ/g)	18[b]	18[b]	25[c]
P_2O_5 content of PPA (wt. %)	not available		82.6
Processing			
die geometry	circular	rectangular	tubular
dimension (mm)	0.18 (diam.)	1.0 (gap)	2.0 (gap)
extrusion temp. (°C)	25	25	120
draw ratio	3:1	3:1	20:1
coagulant	water	water	(a) water (b) 85%H_3PO_4
Notation	FB	FM1	(a) FM2W (b) FM2P

[a] In MSA; approximate molecular weights, using equation (1.8) are: (b) 34,000; (c) 41,000.

phosphoric acid (15% water) obtained from Eastman Kodak Chemicals. The samples were not constrained during coagulation. All handling of the uncoagulated films, and the films coagulated in phosphoric acid, were done in a glove bag under dry nitrogen. In order to prepare samples for electron microscopy and SAXS, as described below, some films coagulated in phosphoric acid were transferred after 24 hours to a water bath for removal of the acid.

Drying of the wet films, for wide-angle X-ray diffraction (WAXD) measurements, was done at 120°C under tension of about 10MPa.

2.1.2 Sample Preparation

In order to study the morphology formed during coagulation it was necessary to avoid the collapse of the structure that would occur during drying of the wet fibers and films. A technique was developed to impregnate the water-swollen fibers and films with an epoxy resin, following Spurr [62]. First, water was gradually replaced with ethanol in the following sequence:

> 20, 40, 60, 95, 3x100% ethanol - 1 hour each, 100% ethanol overnight.

Next, ethanol was gradually replaced with components of the Spurr resin in the sequence:

> 50, 75, 3x100% resin - 3 hours each, 100% resin overnight

The resin composition was:

> vinyl cyclohexene dioxide (ERL-4206) - 10 g.
> nonenyl succinic anhydride (NSA) - 26 g.
> dimethyl amino ethanol (DMAE) - 0.4 g.

After infiltration, short segments of the impregnated fiber or film

(about 0.2x0.2x30mm) were mounted in polyethylene capsules. The capsules were filled with spun resin of a suitable consistency for sectioning with a microtome. It was composed of the resin components in the amounts mentioned above, with the addition of 6 g. flexiblizer (diglycidyl ether of polypropylene oxide - DER 736). The resin was then cured at 70°C for 10-16 hours.

For transmission electron microscopy, sections about 600Å in thickness were obtained using a Sorvall microtome, and a Diatome diamond knife, at room temperature. The sections were floated onto water where their thickness was judged by the interference colors, and picked up on copper grids.

Films for X-ray scattering measurements were obtained by impregnating with the epoxy resin in the manner described above, or by drying at 120°C under tension of about 10MPa.

For wide-angle X-ray diffraction measurements from the oriented PBT/PPA solution and from PBT films coagulated in phosphoric acid, film segments about 0.5x1.0 cm in area were sealed between thin polyimide sheets (Kapton, 1/2 mil thickness), using standard 5-minute epoxy, under dry nitrogen.

2.2 PBLG

PBLG having nominal molecular weight of 210,000 was obtained from Sigma Chemical Co. The solutions used in this study were 1.0% (w/w) in distilled benzyl alcohol (BA) and 0.06% (w/w) in benzene. They were prepared by dissolution of the polymer at 80°C.

The gelation temperature of the PBLG solution in BA was determined by placing about 1ml of an isotropic solution at 70°C, in a sealed glass vial and holding the solution for 2 hours at a fixed temperature. The temperature at which no flow of the solution could be observed, when the vial was overturned was determined as the gelation temperature (40°C for the 1% solution in BA). A gelation temperature of 35°C was determined by Murthy et al. [54] for a 1% solution of PBLG (MW=385,000) in BA, by measuring the elastic shear modulus.

For SAXS measurements, the 1% PBLG solution in BA was transferred at 70°C to a thin-walled (0.01mm) glass capillary, 2mm in diameter. The capillary was sealed, annealed at 70°C for one hour and then cooled to room temperature.

Sample preparation for electron microscopy is described in section 2.3.3.

2.3 Methods of Investigation

2.3.1 Small-Angle X-ray Scattering (SAXS)

Measurements of SAXS patterns were performed using a slit-collimated incident beam. The sample was placed with the extrusion direction parallel to the collimation slit. Copper K_α radiation (λ=1.542Å) was generated at 40kV and 30mA with a Siemens FK60-40 fine-focus tube and K805 generator. CuK_β radiation was removed with a standard Ni filter. A Kratky camera was used, with a collimation block having a 0.04mm entrance slit and beam-limiter separation of 16mm.

The intensity of radiation scattered in a direction perpendicular to the collimation slit was measured with a Braun linear position-sensitive detector, for which a spatial resolution of 0.05mm is estimated [63]. The data was collected with a Canberra Series 35 multichannel analyzer interfaced with a PDP 11/34 computer for analysis. The scattering angle was calibrated using an osmium stained duck tendon, whereby up to twelve orders of the principal reflection, having a spacing of 640Å, could be observed. The sample to detector distance was 53.1cm.

The measured intensity was corrected for parasitic scattering, variations in the sensitivity of the detector wire and absorption by the sample. Its value was scaled to absolute intensity units using a calibrated Lupolen sample [64-66] using the following relation:

$$\tilde{I} = \left[\frac{L}{CTt\tau_s}\right] \frac{\tilde{i}_s}{\tilde{i}_c} \qquad (2.1)$$

where $\tilde{I}$ is the absolute slit-smeared intensity per unit volume of sample [electrons^{2}cm/cm^3], $\tilde{i}_s$ is the slit-smeared intensity [counts/sec.] measured from the sample and $\tilde{i}_c$ is the intensity measured from the calibration standard at an angle equivalent to a spacing of 150Å. T is the Thompson scattering factor (7.94×10^{-26} cm^2), t is the sample thickness, and C a constant characteristic of the specific calibration sample used (C=69.9[electrons^{-2}] for the standard used in this study). τ_s, the transmission coefficient of the sample, is determined from the ratio of the intensities measured by a D-500 diffractometer from the (110) planes

of a polypropylene specimen, before and after the sample was placed on the face of the D-500 detector.

SAXS patterns from a pinhole-collimated incident beam were obtained using a Statton camera and recorded on flat film as described in section 2.3.2. Sample to detector distance was 313mm.

2.3.2 Wide-Angle X-ray Diffraction (WAXD)

X-ray diffraction patterns were recorded on flat film (Kodak DEF-5) in a Statton camera using an incident beam collimated with a pinhole 0.2mm in diameter. The scattering angle was calibrated using a TCNQ powder. Ni filtered CuK_{α} radiation, generated by an Enraf Nonius D583 generator and tube (at 40kV and 32mA), was used.

A Siemens D-500 diffractometer equipped with a Huber goniometer and a proportional scintillation counter was used to scan the equatorial reflections. X-rays were generated as described for the SAXS measurements. The beam was collimated with two 0.3° slits between the source and the sample, and 0.3° and 0.15° slits before the detector, such that the dimensions of the beam incident on the sample were about 15x1.5mm. The diffractometer was interfaced with a PDP 11/34 computer for driving the stepping motors and data acquisition and analysis. The intensity was measured in transmission mode, the samples being placed with the extrusion direction perpendicular to the direction of the collimation slit.

2.3.3 Electron Microscopy

A JEOL 100CX electron microscope operated at 100KV was used throughout this work. Bright-field imaging was performed using an objective operature 40μm diameter (about 5.8×10^{-3} radians). Care was taken to minimize radiation damage by keeping the dose rate less than about 2.5×10^{-3} Amp/cm^2, as estimated from the current reading of the exposure meter. (The screen efficiency has been previously determined by A. Falls as 65% using a Faraday cup.) For typical exposure times of 4-11 seconds the radiation dose is about two orders of magnitude smaller than the critical dose of 1.6 C/cm^2, for which the intensity of the equatorial peak of PBT, at 3.5Å, decreases to 37% of its original value [28,34]. The higher magnification images were usually obtained at a magnification of 26,000. The objective lens was underfocused about 3.4μm in order to enhance phase contrast.

Attempts at dark-field imaging of PBT using its equatorial reflections were unsuccessful. Diffraction contrast was minimal since both the equatorial PBT reflections and the amorphous halos of the epoxy matrix (the major component) appear at similar scattering angles. Dark-field imaging was further inhibited by the small size of PBT crystallites (estimated as 10-20Å for the as-spun state [34]) and compounded by having about 80% of the sample volume comprised of the epoxy matrix.

Electron diffraction patterns were obtained typically at a camera length of 46cm using a selected area diffraction operature of 80 μm diameter (corresponding to a selected area of less than 3 μm on the sample).

The images and diffraction patterns were recorded on Kodak SO-163 film and developed in D-19 diluted 1:2 for 4 minutes. Images of the frozen PBLG gels (proceeding section) were developed in full strength D-19 for 8 seconds, for increased sensitivity.

2.3.4 Cryogenic Methods in Electron Microscopy

Much effort was directed towards visualization of PBLG gels by electron microscopy using cryogenic methods. Results were obtained using two techniques:

(a) cryofixation of thin films and subsequent observation using a cold stage

(b) cryofixation of larger droplets and subsequent observation of a replica of a fracture surface

The first technique was performed under the guidance of Professor Y. Talmon at the Technion in Israel. This procedure involves the following steps: (a) preparation of a thin film of the gel; (b) rapidly freezing the sample; (c) transfer of the frozen specimen to the electron microscope; (d) observation at a controlled (low) temperature.

A copper grid (400 mesh) is suspended vertically at the tip of tweezers held in a plunging apparatus as shown in the photograph in Figure 2.1. A drop of a very dilute solution is placed with a pipette on the front face of the grid and excess solution is blotted by touching filter paper to the rear face of the grid. A thin film of the solution is formed within the copper mesh, partly by drainage of fluid to the bottom of the grid, and mostly by evaporation of the solvent. This process is monitored by viewing the grid with a microscope.

Figure 2.1. Photograph of the cryofixation apparatus.

The objective is to induce gelation by an increase in the polymer concentration due to the evaporation of the solvent. It is also necessary that the gelled film will be of suitable thickness for imaging in the electron microscope (i.e., less than 0.2μm thick). Once a thin film is obtained, as determined by the appearance of interference colors, a mechanism is triggered by which the grid is plunged into supercooled liquid ethane, cooled to below its crystallization temperature by liquid nitrogen (77°K). Using this technique, images of frozen aqueous dispersions in which the water matrix has been successfully vitrified to the amorphous state, have been obtained [67].

Once the film has been frozen, it is transferred under liquid nitrogen into a modified JEOL cold-stage sample holder in a transfer module. The cold stage allows maintenance of the specimen in the microscope at temperatures close to that of liquid nitrogen, and is equipped with a thermocouple and heating element. By means of a temperature controller the sample temperature can be set in the range from about 90°K to room temperature. The specimen assembly in the cold stage is described by Talmon et al. [68], and details of the transfer module and the modified cold stage are given by Perlov, Talmon and Falls [69].

A small modification was made to the transfer module in this study, by replacing the Ni-Cr strip used to heat the O-ring of the cold stage by radiating across a 5mm gap, with a coil of Ni-Cr wire (8.8 Ω/m, 46cm long) embedded in Sauereisen DW-30 electrical cement. This allows operation at a lower current, lower temperature and smaller (1mm) gap.

The ability to form films amenable to study by electron microscopy using this technique depends on a critical combination of viscosity, surface tension and volatility of the solvent. Although microemulsions of several organic liquids have been studied in this way [70], it has not been used previously with pure organic liquids or polymer solutions. It was necessary to screen several solvents, in which PBLG undergoes gelation, for suitability to this technique. The solvents tested were: benzyl alcohol, DMF, benzene, toluene, dioxane, THF, chloroform, and 2-chloroethanol. Several PBLG concentrations were also tested. Thin films suitable for electron microscopy were obtained only with solutions in benzene at an initial concentration between 0.05 and 0.12 wt. percent. The data reported here were obtained with a solution of 0.06 wt. % in benzene, which was heated to 40°C before placement on the vertical grid.

The second method used to image the structure of the PBLG gel was a freeze-etch replication technique, which has been found useful in the case of other polymer gels [71]. A fragment of a PBLG gel formed from a 1% solution in benzyl alcohol was frozen by quenching in dichlorodifluoromethane cooled by liquid nitrogen. The frozen gel was then transferred to a Balzers BAF400D freeze etch replication device. The sample was fractured by a rotating steel knife at -100°C and the fracture surface etched by sublimation of the solvent at -50°C for eight minutes. The etched surface was replicated by shadowing with platinum (from a C/Pt rod) at a 45° angle followed by evaporation of carbon at a 90° angle to form a support film. The PBLG gel was then removed from the

replica by immersion in benzyl alcohol at 100°C. The carbon/platinum replica was washed in ethanol and twice in distilled water, and collected onto a copper grid.

2.3.5 Other Methods

Thermal analysis by differential scanning calorimetry (DSC) were performed using a Perkin Elmer DSC-2 at a scan rate of 20°C/min in the temperature range of 50-330°C. The melting points of indium, lead and tin were used for temperature calibration. Samples of the PBT solution in PPA, coagulated in phosphoric acid, were sealed in gold DSC pans designed for highly volatile materials. All sample handling was done in a glove bag under dry nitrogen.

The density of PBT films impregnated with epoxy resin was determined gravimetrically, their volume being calculated from their measured dimensions. Alternatively, Archimedes' principle was used, comparing their weight in air and in doubly distilled water. Both methods gave similar results.

CHAPTER III

SMALL-ANGLE X-RAY SCATTERING (SAXS) FROM ORIENTED SYSTEMS

The measurement of SAXS using a slit-collimated incident beam, as in the use of a Kratky camera, is a very useful method as it allows for high resolution at small angles as well as accurate intensity measurements at larger angles [72]. Although it is most often used in conjunction with isotropic samples [72], this method has also been applied to the study of oriented systems such as carbon fibers [73-74], and craze fibrils [75-77]. The object of this chapter is to outline the derivation of general relations for a comprehensive interpretation of SAXS patterns obtained from oriented systems using a slit-collimated incident beam.

3.1 The Significance of a Slit-Collimated Incident Beam

The scattering pattern obtained from a pinhole-collimated incident beam is the Fourier transform of the correlation function, as shown by Debye and Bueche [78]. For small-angle X-ray scattering this can be written as:

$$I(\underset{\sim}{s}) = \langle \eta^2 \rangle \int_{-\infty}^{\infty} \gamma(\underset{\sim}{r}) e^{i(2\pi \underset{\sim}{s} \cdot \underset{\sim}{r})} d\underset{\sim}{r}^3 \qquad (3.1)$$

where: $I(\underset{\sim}{s})$ - the absolute scattered intensity per unit volume [electrons^2/cm^3]

$\underset{\sim}{r}(x,y,z)$ - spatial position vector

$\underset{\sim}{s}(s_1,s_2,s_3)$ - a vector in reciprocal space for which:

$$|s| = 2\sin\Theta/\lambda \tag{3.2}$$

where 2Θ is the scattering angle and λ is the wavelength of the scattered radiation.

$\gamma(r)$ is the correlation function, defined as:

$$\gamma(\underset{\sim}{r}) = \langle\eta(\underset{\sim}{r}'+\underset{\sim}{r})\eta(\underset{\sim}{r}')\rangle_{\underset{\sim}{r}'}/\langle\eta^2(\underset{\sim}{r}')\rangle_{\underset{\sim}{r}'} \tag{3.3}$$

where $\eta(\underset{\sim}{r})$ is the fluctuation in electron density $\rho(\underset{\sim}{r})$

$$\eta(\underset{\sim}{r}) = \rho(\underset{\sim}{r}) - \langle\rho(\underset{\sim}{r}')\rangle_{\underset{\sim}{r}'} \tag{3.4}$$

The geometry of a small-angle scattering experiment using a slit-collimated incident beam is shown in Figure 3.1, where the z axis defines the direction of the collimation slit. The correlation function in a cross section plane perpendicular to the z axis is obtained by an inverse Fourier transform of equation (3.1):

$$\gamma(x,y,0) = \frac{1}{\langle\eta^2\rangle}\int_{-\infty}^{\infty}\int_{-\infty}^{\infty}\left[\int_{-\infty}^{\infty} I(s_1,s_2,s_3)\,ds_3\right] e^{-i2\pi(s_1x+s_2y)}\,ds_1\,ds_2 \tag{3.5}$$

The scattered intensity measured at position P on the detector is the sum of contributions from all volume elements of the sample irradiated by the beam. The scattered intensity can be calculated under the following assumptions:

(a) The incident beam is of constant intensity up to a value of $|z^*|$ such that $I(s^*)$ is negligible, where $s^*\simeq z^*/L\lambda$, L being the sample to detector distance.

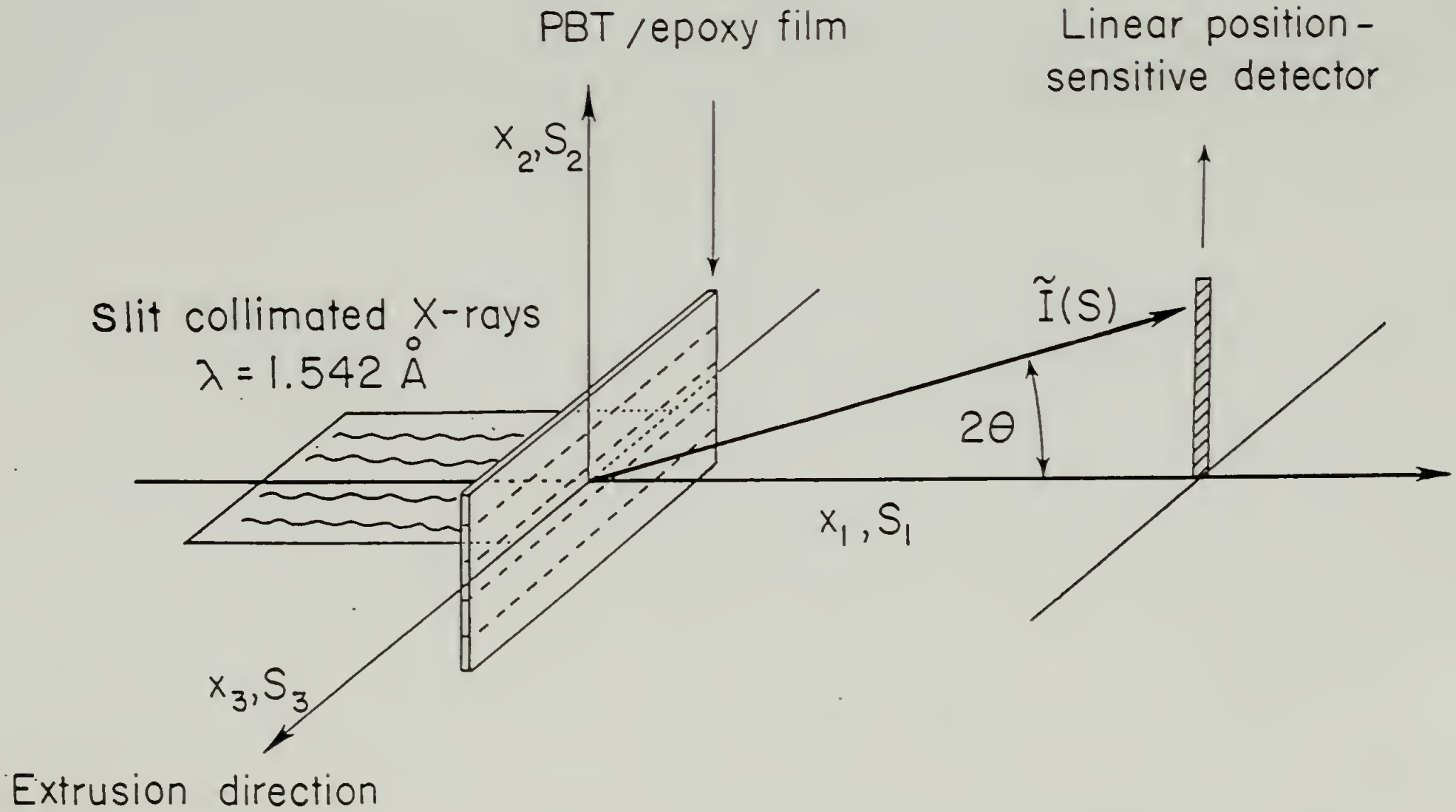

Figure 3.1. The geometry of the small-angle X-ray scattering experiment.

(b) The structure is homogeneous in the z direction, such that in all cross-section planes perpendicular to the z direction the structures are equivalent, having the same correlation function.

Thus for small angle scattering where $s_3 \simeq z/L$, the smeared intensity per unit volume, $\tilde{I}(P)$ [electron^{2}cm/cm^3], is given by

$$\tilde{I}(P) = \int_{-\infty}^{\infty} I(P)dz = L\lambda \int_{-\infty}^{\infty} I(s_1,s_2,s_3)ds_3 \tag{3.6}$$

Substituting (3.6) in (3.5) and Fourier inversion yields:

$$\tilde{I}(\underset{\sim}{S}) = L\lambda\langle\eta^2\rangle \int_{-\infty}^{\infty} \gamma(\underset{\sim}{R}) e^{i(2\pi \underset{\sim}{S}\cdot\underset{\sim}{R})} d\underset{\sim}{R}^2 \tag{3.7}$$

where $\underset{\sim}{R}(x,y)$ and $\underset{\sim}{S}(s_1,s_2)$ are vectors in a cross-section plane perpendicular to z and s_3 respectively. For a structure having cylindrical symmetry about the z axis equation (3.7) becomes [79]:

$$\tilde{I}(S) = L\lambda\langle\eta^2\rangle \int_{0}^{\infty} \gamma(R) J_0(2\pi SR)\, 2\pi R dR \tag{3.8}$$

where $R=|\underset{\sim}{R}|$, $S=|\underset{\sim}{S}|$ and J_0 is the first order Bessel function.

Thus the slit-smeared scattering pattern has been shown [73,75] to be equivalent to the scattering pattern of a two dimensional system, the structure of which is described by the cross section of the three dimensional correlation function in a plane perpendicular to the collimation slit. An effective electron density per unit area, σ, may be assigned to the system, as given by

$$\sigma(x,y) = (L\lambda)^{1/2} \rho(x,y,0) \tag{3.9}$$

The absolute smeared intensity per unit volume of a three dimensional structure is thus equivalent to the absolute intensity per unit area of a two dimensional structure. Defining the fluctuation in the effective two-dimensional electron densities $\zeta(R)$, as

$$\zeta(\underset{\sim}{R}) = \sigma(\underset{\sim}{R}) - \langle\sigma(\underset{\sim}{R}')\rangle_{\underset{\sim}{R}'} \tag{3.10}$$

Equation (3.8) can be rewritten as

$$\tilde{I}(S) = \langle\zeta^2\rangle \int_0^\infty \gamma(R) J_0(2\pi SR) 2\pi R dR \tag{3.11}$$

3.2 The Limit of Large Scattering Angle, and the Scattering Invariant

The relationships between specimen structure and the scattering pattern for a two-dimensional system are now derived, following the classic treatments of Debye, Anderson and Brumberger [80] and of Porod [81] for a three dimensional system.

The treatment of Debye et al. [80] considers the random placement of cords of length R in a structure consisting of two homogeneous phases, and calculates the probability that the ends of the cord are situated in dissimilar phases, as shown in Figure 3.2a. Four proability functions, $\{P_{ij}(R):\ i,j=1,2\}$, are defined by the conditional probability that one end of a cord of length R, placed at random in the material, is in phase j, given that the other end is in phase i. The four conditional probabilities are related by:

$$\text{(a)}\ P_{ii}(R) + P_{ij}(R) = 1 \tag{3.12}$$

$$\text{(b)}\ a_i P_{ij}(R) = a_j P_{ji}(R)$$

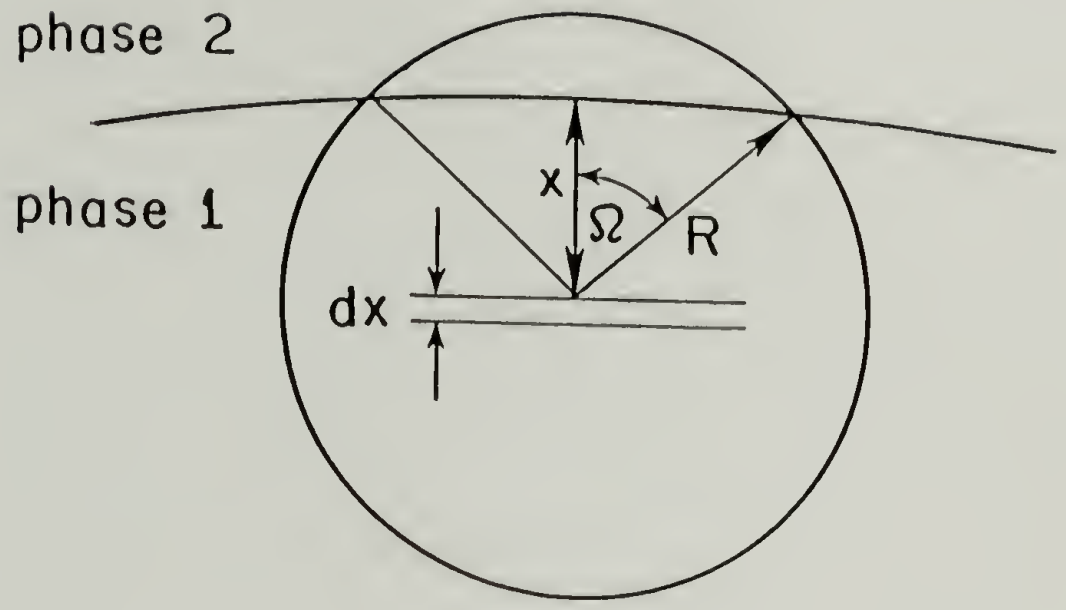

(a)

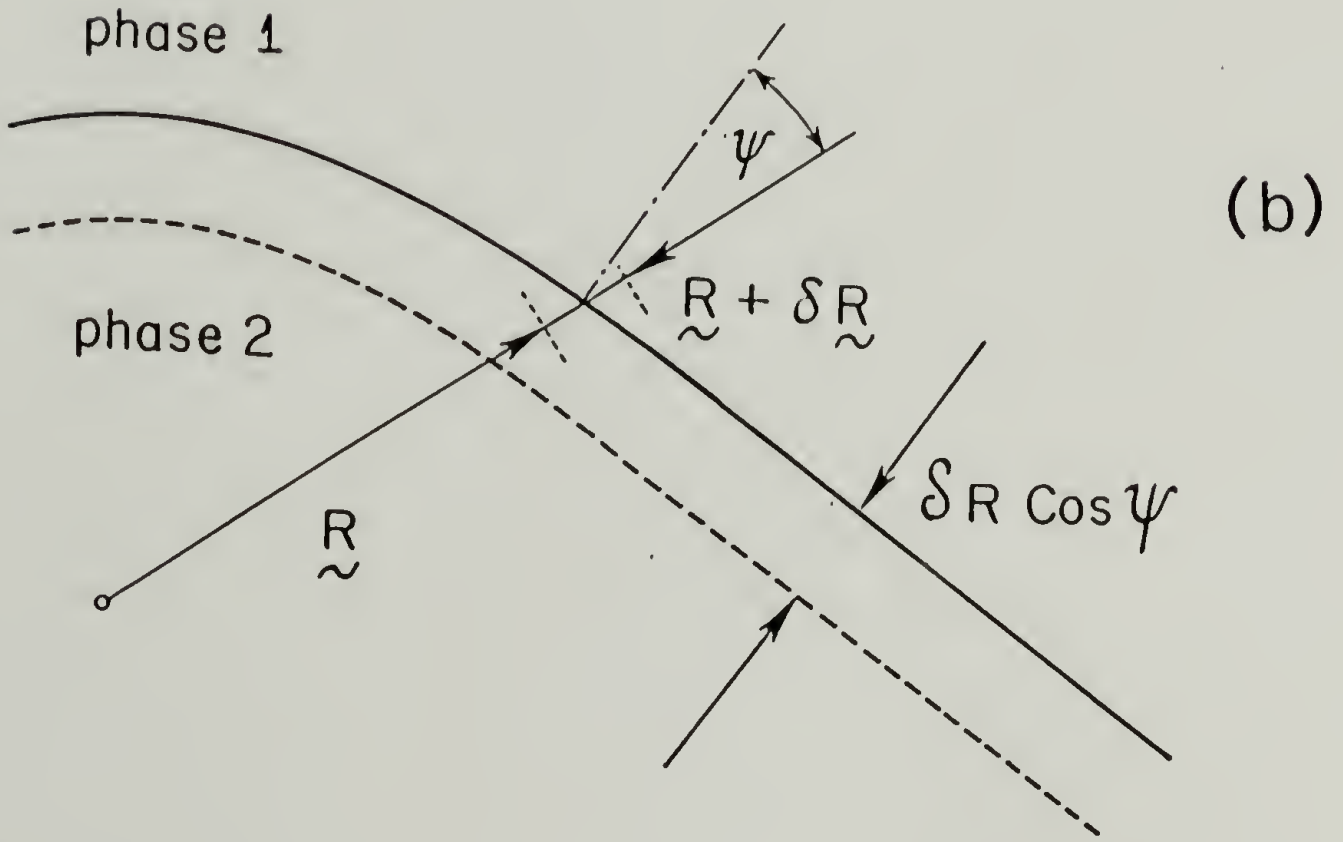

(b)

Figure 3.2. A sketch of an interface between two phases, used in the derivation of scattering laws.

where a_i is the area fraction of phase i, which is also the probability that an end of a rod is in phase i. Equation (3.12b) results from the ends of the cord being indistinguishable. The three relations given in equations (3.12) (for i,j=1,2) allow the four conditional probabilities to be expressed in terms of a single function f(R):

$$\begin{aligned} &\text{(a)}\ P_{12}(R) = (1-a_1)f(R) \\ &\text{(b)}\ P_{21}(R) = a_1 f(R) \\ &\text{(c)}\ P_{22}(R) = 1-a_1 f(R) \\ &\text{(d)}\ P_{11}(R) = 1-(1-a_1)f(R) \end{aligned} \tag{3.13}$$

The probability of dissimilar ends $P_D(R)$ can be calculated using equations (3.12) and (3.13):

$$P_D(R) = a_1 P_{12}(R) + a_2 P_{21}(R) = 2a_1(1-a_1)f(R) \tag{3.14}$$

The correlation function, defined in equation (3.3) irrespective of dimensionality, can be related to the conditional probabilities (3.13) in a system composed of two homogeneous phases with sharp interfaces between them. If σ_i is the electron density of phase i, ζ_i can be calculated using (3.10) as:

$$\zeta_i = (\sigma_i - \sigma_j)a_j \tag{3.15}$$

The average product of the fluctuations in electron density at positions a distance R apart is:

$$\begin{aligned} \langle \zeta(R'+R)\zeta(R') \rangle_{R'} = {} & a_1 P_{11}(R)\zeta_1^2 + a_2 P_{22}(R)\zeta_2^2 + \\ & + [a_1 P_{12}(R) + a_2 P_{21}(R)]\zeta_1\zeta_2 \end{aligned} \tag{3.16}$$

Also: $$\langle \zeta^2(R') \rangle_{R'} = a_1 \zeta_1^2 + a_2 \zeta_2^2 \tag{3.17}$$

Substituting equations (3.13) and (3.15) in (3.16) and (3.17) yields:

$$\langle \zeta(R'+R)\zeta(R') \rangle_{R'} = a_1(1-a_1)(\sigma_1-\sigma_2)^2[1-f(R)] \tag{3.18}$$

and

$$\langle \zeta^2(R') \rangle_{R'} = a_1(1-a_1)(\sigma_1-\sigma_2)^2 \tag{3.19}$$

Using (3.18) and (3.19) in the definition of the correlation function (3.3) yields:

$$\gamma(R) = 1-f(R) \tag{3.20}$$

which substituted in (3.14) yields:

$$P_D(R) = 2a_1(1-a_1)[1-\gamma(R)] \tag{3.21}$$

If the length of the cord, placed randomly within the sample, is allowed to be very small compared to the dimension of the inhomogeneities of the sample, its ends will be situated in dissimilar phases only when they are on different sides of the same interface, as shown in Figure 3.2a. In this case, the probability of dissimilar ends $P_D(R)$ can be expressed as twice the product of the probability that one end is at a distance $0<x<R$ from the interface, with the probability that the cord has the proper orientation to intersect the interface. (The factor of two is again due to the indistinguishability of the ends.)

Let $p_x(x)dx$ be the probability that one end of the cord is at a distance between x and x+dx from the interface. It is the ratio of the area element in which that end can be situated, to the total area of the system. This area element is a band of width dx which follows the contour of the interfacial curve, as shown in Figure 3.2a. The total

length of this band is equal to the total length of the interfacial curve, so that:

$$p_x(x)dx = \frac{C}{A}\,dx \tag{3.22}$$

where C is the length of the interfacial curve per area A.

If one end of the cord is fixed at a distance x from the interface, and if the cord can assume all orientations with equal probability, then the probability that the cord has the proper orientation to intersect the interface is the ratio of the length of the sector ($\alpha\beta$) (in Figure 3.2a) to the circumference of a circle of radius R. Thus the probability that a cord of length R intersects the interface when one of its ends if fixed at a distance x from it is:

$$p_\Omega(R,x) = \frac{(\alpha\beta)}{2\pi R} = \frac{1}{\pi}\,\text{arc}\,\cos(x/R) \tag{3.23}$$

The probability of dissimilar ends is therefore:

$$P_D(R) = 2\int_0^R p_\Omega(R,x)\,p_x(x)\,dx = \frac{2C}{\pi A}\int_0^R \text{arc}\,\cos\left(\frac{x}{R}\right)dx$$

$$P_D(R) = \frac{2CR}{\pi A} \tag{3.24}$$

Equation (3.24) is valid for small values of R only. Accordingly, the value of $P_D(R)$ in the limit of small R can be obtained from equation (3.21) by expanding $\gamma(R)$ in powers of R and neglecting orders of R^2 and higher:

$$P_D(R) = -2a_1(1-a_1)\gamma'(0)R \tag{3.25}$$

The relationship between the length of the interfacial curve per unit

are C/A, to the first derivative of the correlation function at R=0 is obtained by equating (3.24) and (3.25):

$$\frac{C}{A} = -\pi a_1(1-a_1)\gamma'(0) \qquad (3.26)$$

In keeping with the limit of small R, the correlation function in equation 3.11 can be replaced by its Taylor expansion about R=0. A change of variable to u=2πSR yields:

$$\tilde{I}(S) = \frac{\langle\zeta\rangle^2}{2\pi S^2}\left\{\int_0^\infty uJ_0(u)\,du + \frac{\gamma'(0)}{2\pi S}\int_0^\infty u^2J_0(u)\,du + \frac{\gamma''(0)}{8\pi^2S^2}\int_0^\infty u^3J_0(u)\,du + \ldots\right\} \qquad (3.27)$$

Substitution in equation (3.27) of the value of the integrals given in the Appendix, and using (3.19) and (3.26), yields the Porod relationship for the large angle limit of the scattering pattern from a two dimensional structure with sharp interfaces:

$$\tilde{I}(S) = \frac{(\sigma_1-\sigma_2)^2 C/A}{4\pi^3} S^{-3} + O(S^{-5}) \qquad (3.28)$$

The prefactor of the S^{-3} term in equation (3.28) is termed the Porod constant K_p. A similar relationship has been derived by Kirste and Porod [82] in treating the scattering from a system of oriented "infinitely long" elements.

An important characteristic of the scattering pattern is the scattering invariant--a measure of the integrated intensity. It can be related to the mean squared electron density fluctuation by Fourier

inversion of equation (3.8) or (3.11), and substitution of R=0 [81]:

$$Q = \int_0^\infty \tilde{I}(S)\,2\pi S\,dS = L\lambda\langle\eta^2\rangle = \langle\zeta^2\rangle \tag{3.29}$$

where Q is the scattering invariant. Using equation (3.19), its value for a two-phase system with sharp interfaces is [81]:

$$Q = a_1(1-a_1)(\sigma_1-\sigma_2)^2 \tag{3.30}$$

If the scattering elements in the two dimensional structure can be approximated as discs covering an area fraction a_1, their average diameter, $\bar{D}$, can be obtained from the length of the interfacial curve per unit area, using equations (3.28) and (3.30):

$$\bar{D} = \langle D^2\rangle/\langle D\rangle = Q/\pi^3(1-a_1)K_p \tag{3.31}$$

which is the same as derived by Paredes and Fischer [76] for scattering by cylinders.

3.3 Scattering From a Random Two-Phase Structure

The form of the correlation function for a random two-phase structure is obtained following Debye et al. [80], with reference to Figure 3.2b. The conditional probability $P_{22}(R)$ (defined in section 3.2) of having a free end of a cord of length R in phase 2, given that the other end is fixed in phase 2, is considered. A change in $P_{22}(R)$ will occur only if the free end of R is at a distance smaller than $\delta R\cos\Psi$ from the interface, where Ψ is the angle between a given orientation of R and the normal to the interfacial curve in the vicinity of the free end of R.

In such case, a negative contribution to $P_{22}(R)$ will arise from cords having both ends in phase 2, which upon addition of δR to their free end will intersect the interface. Conversely, a positive contribution to $P_{22}(R)$ will arise if the free end is in phase 1, which upon addition of δR will reenter phase 2. The probability that the free end of the cord is located in a band of width $\delta R\cos\Psi$ following the contour of the interface, given that it is located in a specific phase i, is the ratio of the area of the band to the area of the specific phase - $A_i = Aa_i$. Thus:

$$\delta P_{22}(R) = -P_{22}(R)\frac{C}{a_2 A}\,\delta R\langle\cos\Psi\rangle + P_{21}(R)\,\frac{C}{a_1 A}\,\delta R\langle\cos\Psi\rangle \qquad (3.32)$$

where $\langle\cos\Psi\rangle$ is averaged over all possible orientations of the cord which allow it to cross the interface upon addition of δR to its free end:

$$\langle\cos\Psi\rangle = \int_{-\pi/2}^{\pi/2}\cos\Psi d\Psi \Big/ \int_{0}^{2\pi} d\Psi = 1/\pi \qquad (3.33)$$

Using equations 3.13, 3.20 and 3.33 in 3.32 and reverting to differentials in the limit, yields:

$$\frac{d\gamma(R)}{dR} = -\frac{C}{\pi a_1(1-a_1)A}\,\gamma(R) \qquad (3.34)$$

$$\gamma(R) = \exp(-R/\ell_c) \qquad (3.35)$$

with the correlation length ℓ_c given as:

$$\ell_c = \pi a_1(1-a_1)A/C \qquad (3.36)$$

By substituting 3.35 and 3.36 in 3.11 and a Fourier Bessel transform [83], the form of the scattering pattern from a random two-phase structure in two dimensions is obtained:

$$\tilde{I}(S) = 2\pi a_1(1-a_1)(\sigma_1-\sigma_2)^2 \ell_c^2/(1+4\pi^2\ell_c^2 S^2)^{3/2} \qquad (3.37)$$

where equation 3.19 for a structure with sharp interfaces has been used. The functional form of equation (3.37) is the same as that derived by Porod [81] for the scattering pattern obtained from a random three dimensional structure using a slit-collimated incident beam, as naturally its cross-section is also a random two-dimensional structure.

3.4 Scattering From a Collection of Particles

The intensity of x-rays scattered at small angles by a particulate system results from the interference of waves scattered by individual spatial elements within the system. Using pairwise additivity, the scattered intensity (in units of electrons^2) is [78,84]:

$$i(\underset{\sim}{S}) = \int_{-\infty}^{\infty}\int f_1 f_2 \exp\{2\pi i[\underset{\sim}{S}\cdot(\underset{\sim}{R}_1-\underset{\sim}{R}_2)]\} d\underset{\sim}{R}_1^d d\underset{\sim}{R}_2^d \qquad (3.38)$$

where $d\underset{\sim}{R}_i^d$ is the spatial element in d-dimensional space, located at position $\underset{\sim}{R}_i$ and having an electron density of f_i [electrons^2/cm^d].

If the system is composed of widely separated particles, the scattered intensity is the sum of the scattering from the individual particles. If all the particles are identical, and it is further assumed that:

(a) the particles are centrosymmetric;

(b) each particle can assume all possible orientations with equal probability;

then the intensity scattered from the system of widely separated particles, per unit volume of sample [electrons^2/cm^d] can be written as:

$$I(S) = n\overline{F^2(\underset{\sim}{S})} \tag{3.39}$$

where n is the number of particles per unit volume [1/cm^d], $S=|\underset{\sim}{S}|$, and $F(\underset{\sim}{S})$, termed the structure factor [84], is defined as [78]:

$$F(\underset{\sim}{S}) = \int_{\substack{\text{single}\\ \text{particle}}} f_1 \exp[2\pi i \underset{\sim}{S}\cdot\underset{\sim}{R}_1] d\underset{\sim}{R}_1^d \tag{3.40}$$

$\overline{F^2(\underset{\sim}{S})}$ in (3.39) is averaged over all orientations of $\underset{\sim}{R}$ relative to $\underset{\sim}{S}$. It is termed the form factor.

Whenever the density of the particles is sufficiently large, interference from waves scattered by volume elements in different particles must be taken into account. If the particles in the dense system are packed in a crystal having long range order a scattering pattern composed of discrete maxima is obtained. This case is not treated here. For the case where no long range order exists, such as in the liquid state, the intraparticle interference effects can be separated from the interparticle ones if its assumed that there are no correlations between the positions and orientations of the particles. Zernicke and Prins [85] introduced a pair correlation function $g(R_{12})$ which is related to the probability that the center of a particle is located at a distance

R_{12} from the center of another particle, taken as the origin. Thus [84]:

$$I(S) = n\{\overline{F^2(S)} + n\overline{F(S)}^2 \int_0^\infty [g(R_{12})-1]\overline{\exp(2\pi i \underset{\sim}{S}\cdot\underset{\sim}{R}_{12})}\, d\underset{\sim}{R}_{12}^{d}\} \qquad (3.41)$$

The orientational average of the phase factor in equation (3.40) and (3.41) is:

$$\overline{\exp(2\pi i \underset{\sim}{S}\cdot\underset{\sim}{R})} = \begin{cases} \dfrac{\sin(2\pi SR)}{2\pi SR} & d=3 \quad [86] \\ J_0(2\pi SR) & d=2 \quad [79] \end{cases} \qquad (3.42)$$

In further discussion it is assumed that the particles are spherically symmetric (in 3D) or circularly symmetric (in 2D), so that:

$$\overline{F}(S)^2 = \overline{F^2}(S) \equiv F^2(S) \qquad (3.43)$$

For the two-dimensional case, equation (3.41) is thus:

$$I(S) = nF^2(S)G(S) \qquad (3.44)$$

where G(S), termed the interference factor, is given by [79]:

$$G(S) = 1 + \int_0^\infty [g(R)-1]J_0(2\pi SR)\,2\pi R\,dR \qquad (3.45)$$

In a real system there will inevitably be polydispersity in particle size. The equation for the scattered intensity is derived analogously to equation (3.41) [84]. For the two dimensional case it is:

$$I(S) = n\{\sum_k p_k F_k^2(S) + n\sum_k \sum_j p_k p_j F_k(S) F_j(S) \int_0^\infty [g_{kj}(R)-1] J_0(2\pi SR)\, 2\pi R dR\} \tag{3.46}$$

where P_k is the probability that one of the particles is of type k having a structure factor $F_k(S)$, and $g_{kj}(R)$ is related to the probability that a center of a particle of type j is located at a distance R from the center of a particle of type k. Now it is not possible to rigorously describe the scattered intensity in terms of a single pair correlation function, as for the monodisperse case. In order to do so it is assumed that the interparticle interference effects can be approximated by those in an equivalent system, composed of monodisperse "average" particles, and having a prescribed pair correlation function.

If the "average" particle is taken as one having the average structure factor $\langle F(S)\rangle$ of the polydisperse system, then equation (3.46) yields:

$$I(S) = n\{\langle F^2(S)\rangle - \langle F(S)\rangle^2\} + n\langle F(S)\rangle^2 G_p(S) \tag{3.47}$$

Equation (3.47) has been used by Dettenmaier [75] in analysis of SAXS measurements from craze fibrils.

If, on the other hand, the "average" particle is taken as one having the average form factor $\langle F^2(S)\rangle$, then equation (3.46) yields:

$$I(S) = n\langle F^2(S)\rangle G_p(S) \tag{3.48}$$

In both (3.47) and (3.48) $G_p(S)$ is the interference factor obtained from the prescribed pair correlation function of the equivalent monodisperse system, using equation (3.45). It is not clear which form, (3.47) or

(3.48) is more appropriate. In this study equation (3.48) is used, for its similarity with equation (3.44), and for its simplicity.

3.5 A Hard Disc Fluid Model for the Scattering from Oriented Fibrils

The microstructure formed by a uniaxial process is commonly observed to be composed of oriented fibrils. Some examples are synthetic fibers formed by solution spinning or melt-extrusion, and craze fibrils formed in glassy polymers under uniaxial tension [75-77]. Following the discussion in section 3.1, the SAXS pattern obtained from a system of oriented fibrils using a slit-collimated incident beam can be analyzed in terms of the structure in a cross section plane perpendicular to the axis of orientation. If the fibrils are well aligned the scattering elements can be identified as the cross sections of the fibrils.

In many cases the packing of the fibrils is very disordered. In such case a possible model for the packing of the fibrillar cross-section is that of a fluid composed of hard, impenetrable discs. This model implies the use of the ergodic assumption that the spatial average of the positions of the elements in the scattering volume is equal to the temporal average of the equivalent elements of the fluid.

The pair correlation function of a hard disc fluid has been evaluated by Chae Ree and Ree [87] using Monte Carlo simulations and numerical solutions to several integral equations. They have shown that the pair correlation function obtained by Monte Carlo simulations are closely fit by those obtained by numerical solution of the Ornstein-Zernicke (OZ) equation [88] using the Percus-Yevick (PY) approximation [89].

Ornstein and Zernicke [88] proposed that the total correlation between two particles in a fluid be separated into a direct part in which all other particles are disregarded, and an indirect part in which the correlation is transferred indirectly via all possible third particles. The OZ equation (3.49) expresses these relations as follows:

$$h(R_{12}) = c(R_{12}) + n\int_{-\infty}^{\infty} c(R_{13})h(R_{32})dR_3^d \tag{3.49}$$

where h(R) is the total correlation function defined as:

$$h(R) = g(R)-1 \tag{3.50}$$

and c(R), termed the direct correlation function, is defined by equation (3.49).

The PY approximation states that [89]:

$$c(R) = y(R)\{\exp[-\beta U(R)]-1\} \tag{3.51}$$

where $\beta=1/kT$ is the Boltzmann factor and y(R) is defined as:

$$y(R) = g(R)\exp[\beta U(R)] \tag{3.52}$$

U(R) is the potential function for head discs of diameter D:

$$U(R) = \begin{cases} \infty & R<D \\ 0 & R>D \end{cases} \tag{3.53}$$

By numerical solution of the integral equation obtained when equations (3.50) to (3.53) are substituted in the OZ equation (3.49), for a two-dimensional space, Chae et al. [86] obtained the first three coefficients of the density expansion of y(R) for a hard disc fluid:

$$y(R^*,n^*) = 1 + g_1(R^*)n^* + g_2(R^*)n^{*2} + g_3(R^*)n^{*3} \tag{3.54}$$

where $R^*=R/D$ and $n^*=nD^2=4a_1/\pi$, a_1 being the area fraction covered by the discs. $g_1(R^*)$ is given by:

$$g_1(R^*) = \begin{cases} 2\arccos(R^*/2)-R^*/2(4-R^{*2})^{1/2} & 0\leq R^*\leq 2 \\ 0 & R^*\geq 2 \end{cases} \tag{3.55}$$

The coefficients $g_2(R^*)$ and $g_3(R^*)$ are tabulated [87]. They are monotonically decreasing functions of R^* in the region $0<R^*<1$. Their value in this region can be readily obtained by a polynomial fit, the coefficients of which are given in Table 3.1.

From the definition of h(R) (3.50) and equation (3.45) it is evident that

$$G(S) = 1 + nH(S) \tag{3.56}$$

A Fourier transform of the OZ equation (3.49), using the convolution theorem yields

$$H(S) = C(S) + nC(S)H(S) \tag{3.57}$$

where H(S) and C(S) are the Fourier transforms of h(R) and c(R). Substituting (3.57) in (3.56) yields:

$$G(S) = [1-nC(S)]^{-1} \tag{3.58}$$

Substituting (3.53) in (3.51) yields, after a Fourier-Bessel transform:

$$nC(S) = -n^*\int_0^1 y(R^*,n^*)J_o(2\pi SR^*)2\pi R^*dR^* \tag{3.59}$$

Table 3.1. A Polynomial Expression for the Coefficients in Equation (3.54) (from a fit of the data in [87]) for $0<R<1$

	$g_i(R) = \gamma_0 + \gamma_1 R + \gamma_2 R^2 + \gamma_3 R^3$	
	$g_2(R)$	$g_3(R)$
γ_0	5.788	8.332
γ_1	-4.901	-7.948
γ_2	-0.0640	-0.1243
γ_3	0.4132	0.8808

Numerical integration of equation 3.59 using equation 3.54 and substitution in equation 3.58, allows the interference factor to be calculated for any desired area fraction of discs (for which the Percus-Yevick approximation and the third order density expansion are still valid). In addition, the finite range of integration in equation 3.59 eliminates truncation errors which affect the simulated pattern at small angles. But as the value of y(R) in the range $0<R<1$ cannot be obtained by Monte-Carlo simulation, the accuracy of the values obtained using the Percus-Yevick approximation can only be inferred by the quality of the fit in the range $R>1$. Interference factors calculated in this way for several area fractions of hard discs are plotted in Figure 3.3.

The scattering pattern from a system of hard discs can now be simulated using equation 3.44 or 3.48, with the interference factor calculated as outlined above. The structure factor of a disc of diameter D is given by [79]:

$$F(S) = \sigma\pi D^2 J_1(\pi SD)/2\pi SD \qquad (3.60)$$

where J_1 is the first order Bessel function. Considering polydispersity in the distribution of disc diameters, the form factor can be calculated as:

$$\langle F^2(S)\rangle = \int_0^\infty P(D)F^2(D,S)dD \qquad (3.61)$$

where P(D) is the distribution of disc diameters.

In order to check the applicability of the method outlined above to the simulation of a scattering pattern from a system of oriented

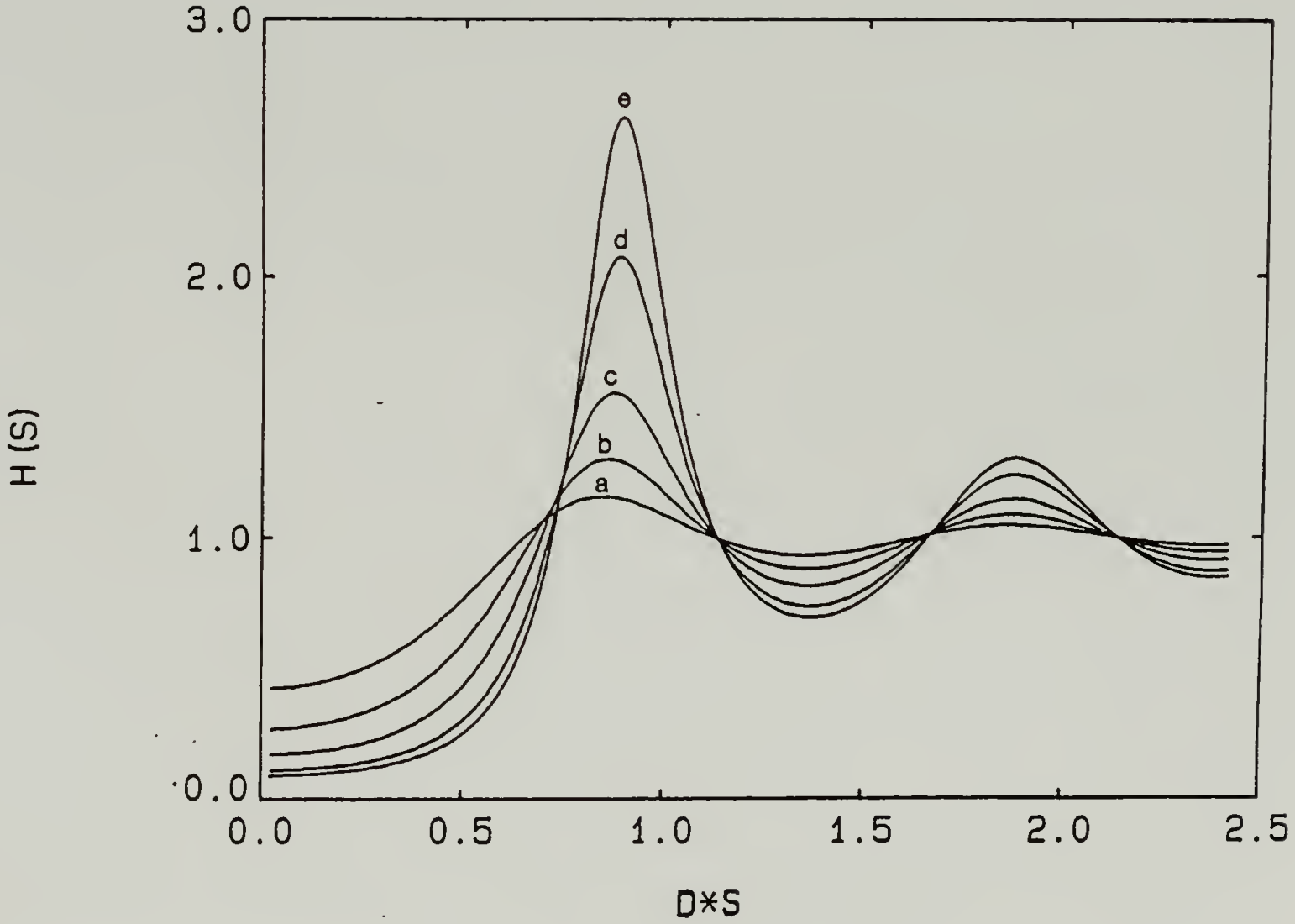

Figure 3.3. The interference factor for a hard disc fluid, calculated for volume fraction of: (a) 0.2, (b) 0.3, (c) 0.4, (d) 0.5 and (e) 0.55.

fibrils, it is used to simulate the SAXS pattern obtained by Paredes and Fischer [76] from polycarbonate crazed by stretching at a strain rate of 0.33%/min at 114°C. They calculated an average diameter $\bar{D}=\langle D^2\rangle/\langle D\rangle$ of 200Å from the asymptotic value of the SAXS pattern at large angles (Porod region) using a volume fraction of 0.45 estimated on the basis of optical measurements. Polysdispersity in the diameter of craze-fibrils is taken into account using a diameter distribution function used by Brown and Kramer [77]:

$$P(D) = (A/D^4)\exp\{-[(D-D_0)/\sigma D_0]^2\} \qquad (3.62)$$

where A is a normalization constant. Brown and Kramer estimated a value of $\sigma=0.28$ for polycarbonate crazes [77].

In Figure 3.4 the experimental data of Paredes and Fischer [76] are plotted together with the simulation obtained using equation (3.48) with equations 3.58-3.62 and a prescribed interference factor of a hard disc fluid with disc diameter D_0. The parameters of the simulation are $D_0=232$Å, $\sigma=0.28$ (for which $\bar{D}=200$Å) and an area fraction of 0.45.

The correspondence between the experimental data and the simulation obtained with parameters which are very close to those estimated by the authors [76,77], verifies the validity of this method and suggests that both the average diameter and the volume fraction of fibrils (as well as possibly some information about the distribution of fibril diameters), can be obtained directly from the scattering pattern by its simulation in the manner described in this thesis.

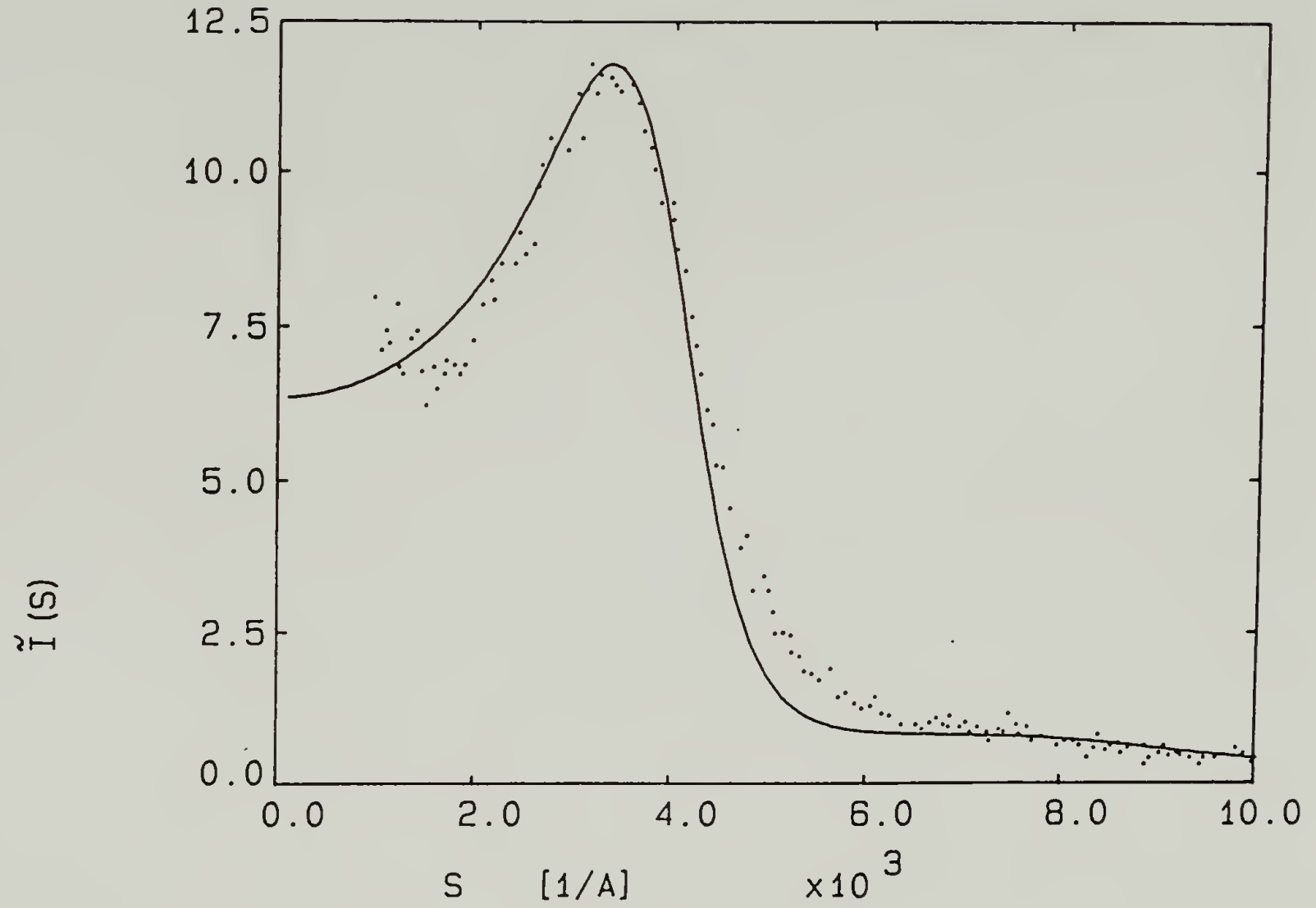

Figure 3.4 The scattering pattern from polycarbonate crazes:
..... experimental data of Paredes and Fischer (reference [76])
——— simulation (see text for details).

CHAPTER IV

THE STRUCTURE FORMED DURING COAGULATION OF PBT FIBERS AND FILMS

4.1 Introduction

This chapter focuses on the coagulation stage in the spinning process of PBT fibers and films. The objective is to characterize the morphology which develops when the oriented nematic solution undergoes a phase transition induced by the action of a coagulant (water). For the morphological characterization, a combination of complementary techniques is utilized: direct visualization by electron microscopy provides a structural model which is tested by SAXS measurements.

A central issue is the ability to control the structure formed during coagulation. The formation of a crystal-solvate phase in isotropic solutions of PBT in MSA, described in section 1.3.2, has motivated the study of alternative coagulation pathways which involve formation of an intermediate crystal-solvate phase. This is achieved by a slower coagulation process, using 85% phosphoric acid as a coagulant. The formation of a novel PBT/PPA crystal-solvate phase is described, and its effect on the ensuing PBT morphology is discussed.

4.2 Direct Visualization of the Basic Morphology: An Interconnected Microfibrillar Network

The microstructure formed by the coagulation process in PBT fibers and films is revealed by electron microscopy. Images of longitudinal

sections of the wet-coagulated PBT fiber (FB) impregnated with an epoxy resin are shown in Figures 4.1 and 4.2, and those of the epoxy impregnated film (FM1) are shown in figures 4.3 and 4.5. The cutting direction was parallel to the fiber axis in the longitudinal sections shown in figures 4.1, 4.3 and 4.5, whereas it was perpendicular to the fiber axis in the one shown in figure 4.2.

At low magnification (figure 4.1a), the fibrillous appearing PBT is seen to be embedded in the epoxy resin. During longitudinal sectioning parallel to the fiber direction, the knife detached some fragments of the fiber from the section (arrows in figure 4.1a). This allows imaging of the underlying fine structure with minimum interference from projection-overlap of the three dimensional structure onto the two dimensional image. A higher magnification image of the thin part in the outlined area, with correct relative orientation, is given in figure 4.1b. At higher magnification (figures 4.1b, 4.2, 4.3), dark longitudinal striations appear parallel to the extrusion direction, with a typical width on the order of 100Å.

The dark striations are identified as PBT microfibrils embedded in an epoxy matrix [38,90]. The PBT microfibrils appear dark due to several contrast mechanisms reinforcing each other. The density difference between PBT ($\sim$1.5 g/cm^3) and the epoxy resin (about 1.0 g/cm^3), as well as the crystalline nature of PBT, result in stronger scattering of electrons by the microfibrils at angles which are blocked by the objective aperture used in obtaining the images. Furthermore, by underfocusing the objective lense, phase contrast is enhanced [91] reinforcing mass

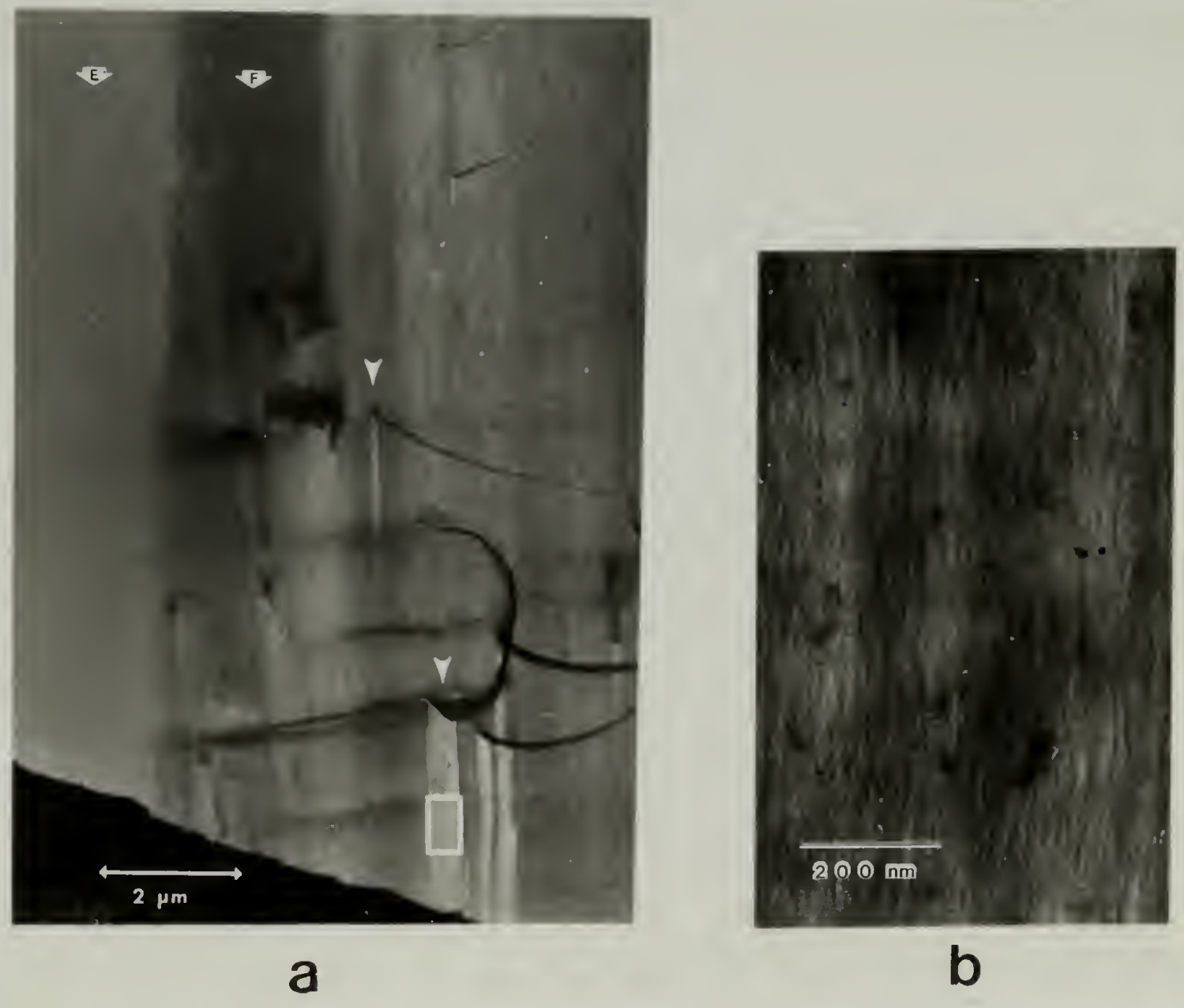

Figure 4.1. An electron micrograph of a longitudinal section of an epoxy-impregnated PBT fiber. Fiber axis and cutting direction are vertical.
(a) Lower magnification image, E - epoxy matrix, F - PBT fiber.
Arrows indicate parts peeled by the cutting knife.
(b) Higher magnification of the outlined area in (a).

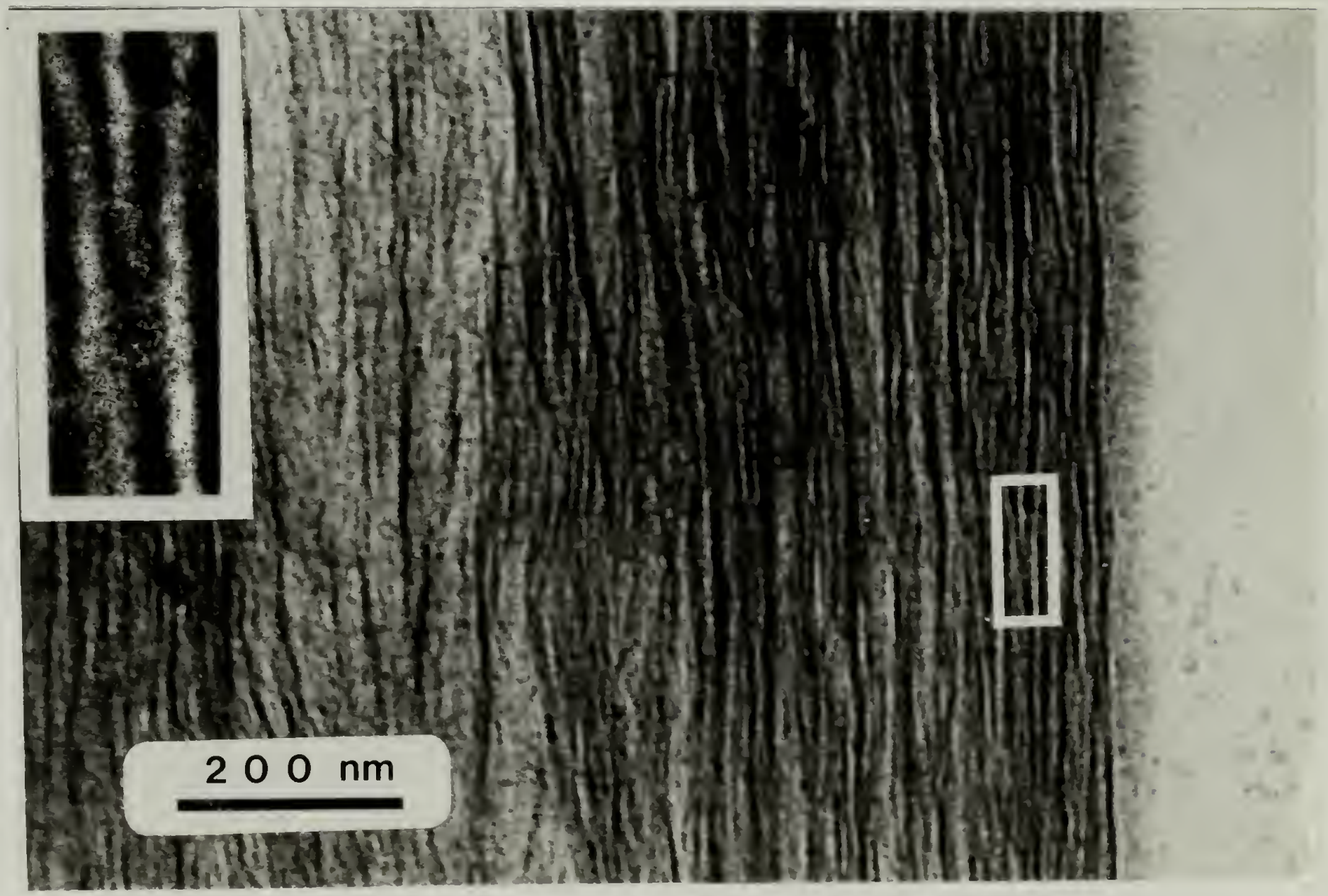

Figure 4.2. An electron micrograph of a longitudinal section of an epoxy-impregnated PBT fiber. Fiber axis vertical, cutting direction horizontal. Inset: Enlargement of a junction between microfibrils.

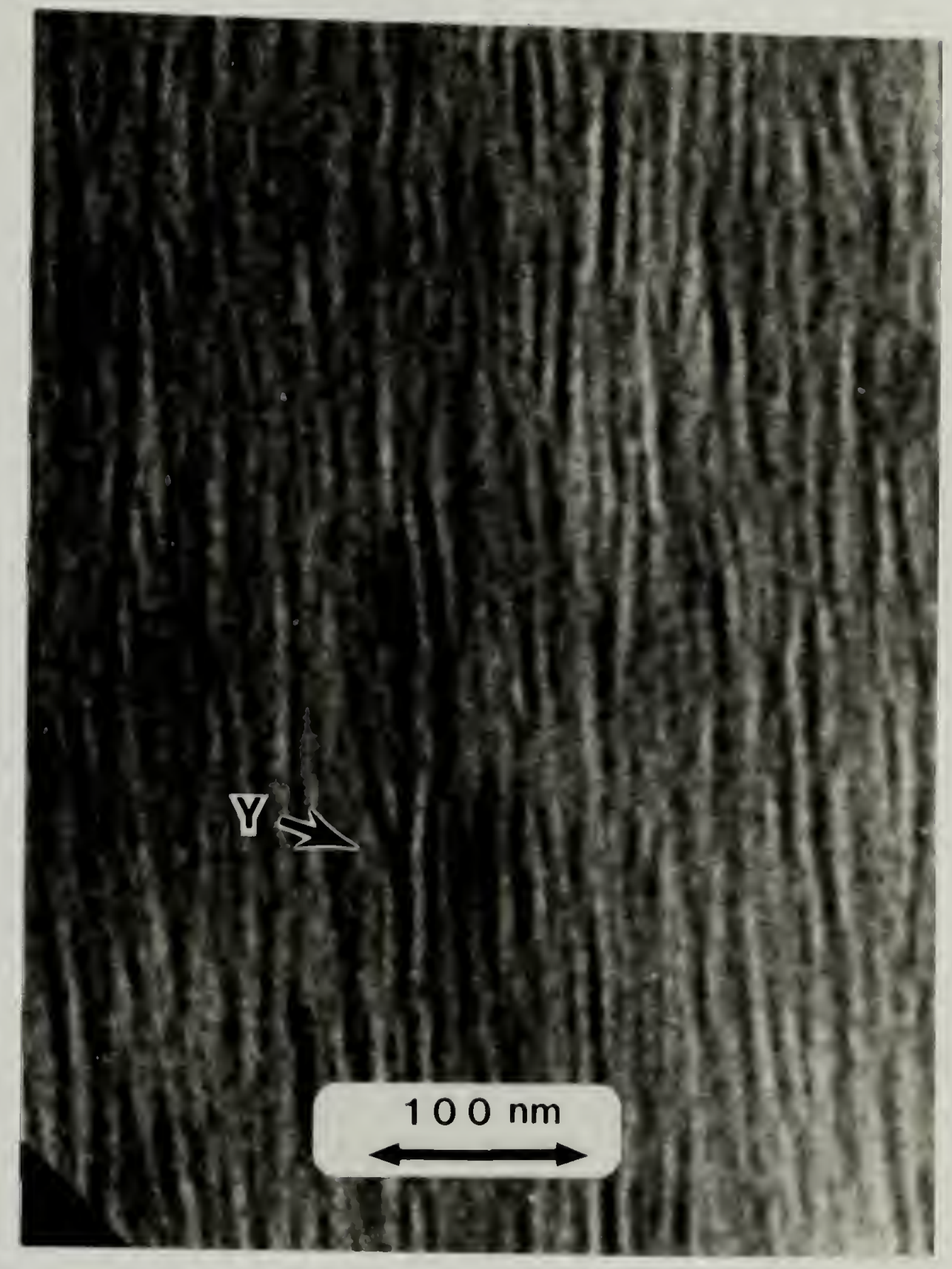

Figure 4.3. An electron micrograph of an epoxy-impregnated PBT film (FM1). Y - "Y"-shaped junction between microfibrils. Both Extrusion and cutting directions are vertical.

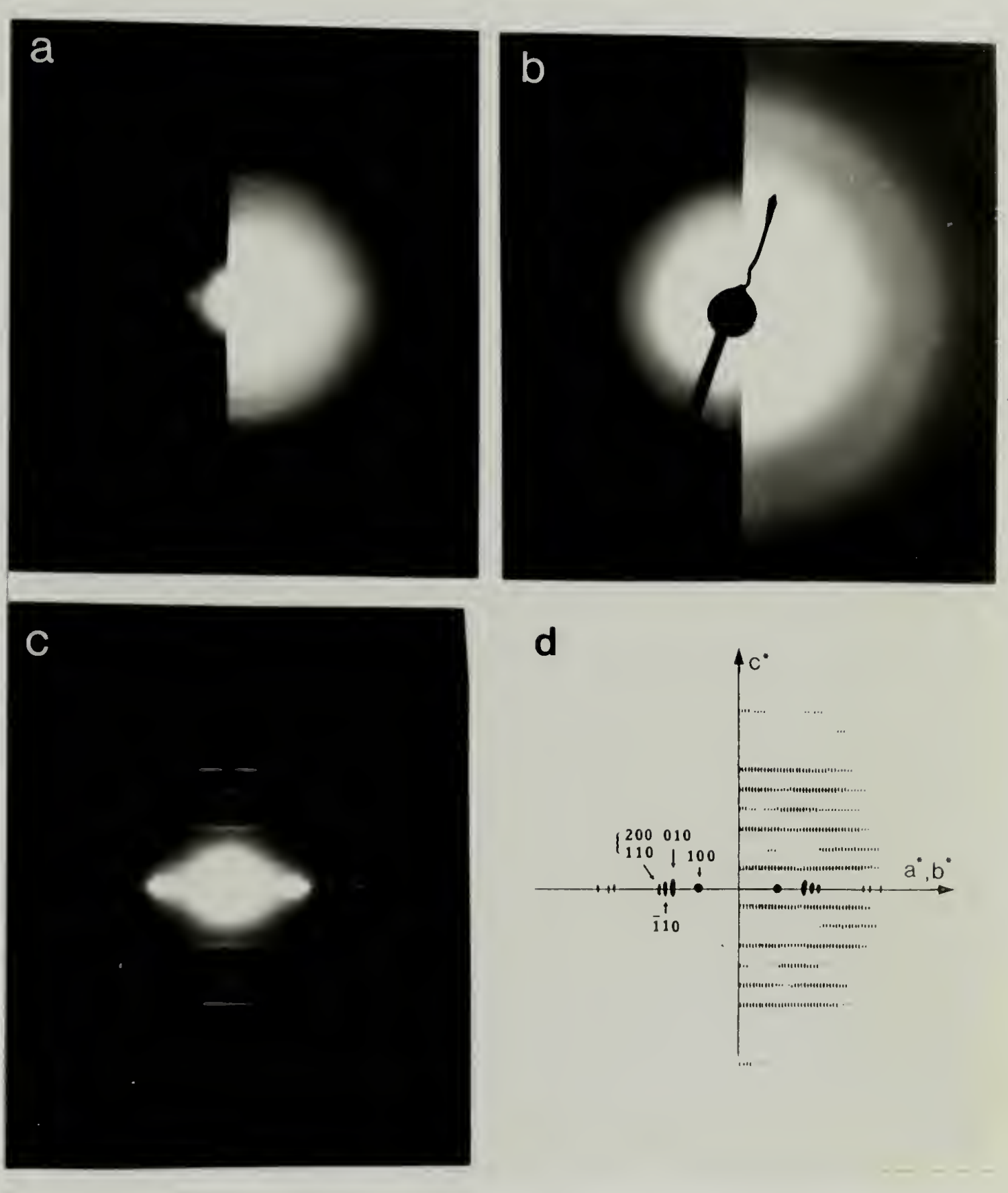

Figure 4.4. Electron diffraction patterns from: (a) epoxy-impregnated PBT fiber, (b) the epoxy matrix, (c) Heat-treated PBT fiber. (d) A schematic represantation of the PBT fiber diffraction pattern.

Figure 4.5. An electron micrograph of a longitudinal section of an epoxy-impregnated film (FM1) exhibiting a buckled region ("kink band"). E - epoxy matrix. Arrows indicate the kink bands.

and diffraction contrast. Appearance of the striations parallel to the extrusion direction irrespective of whether the cutting direction was parallel or perpendicular to it, indicates that they are not artifacts induced by the cutting procedure.

An electron diffraction pattern from an area less than 3um in diameter within a section of the epoxy impregnated fiber is shown in figure 4.4a. It exhibits a superposition of the characteristic PBT fiber diffraction pattern and the amorphous halos of the epoxy matrix. The PBT reflections, although weak and dominated by the amorphous halos of the matrix which is the major component, indicate that the PBT crystallites are less oriented and are less ordered compared to a dried, heat treated PBT fiber. For comparison the electron diffraction from the epoxy matrix alone and from heat-treated PBT are given in figure 4.4b and 4.4c respectively. A schematic representation of the PBT fiber diffraction pattern is shown in figure 4.4d.

Closer inspection of the micrographs reveals "Y"-shaped junctions between microfibrils as indicated by an arrow in figure 4.3 and in the inset in figure 4.2. It is difficult to estimate the length of the microfibrils, i.e., the distance between the junction points. The micrographs shown are two dimensional projections of the three dimensional structure. Partial overlap of the microfibrils may appear in a projection as junctions. Nevertheless, the micrographs shown in figures 4.1-4.3 indicate a wide distribution of microfibrillar lengths, from several hundred to several thousand Angstroms.

These structural elements, the microfibrils and their junctions, which are formed in the coagulation process, constitute the fundamental structure of oriented PBT fibers and films, namely an interconnected network of oriented microfibrils. The network formation is reversible in the sense that replacement of the coagulant with a solvent (i.e., a strong acid) results in dissolution of the microfibrillar network, so that the system reverts to its original state (i.e., a PBT solution). That this network is formed during coagulation explains the ability of the wet-coagulated fibers to sustain a large tensile force [32,36], and indicates that the microfibrillar network is the basis for the structure and properties of the final material.

Further evidence for the relevance of the microfibrillar elements to the compressive properties of PBT is indicated by the electron micrograph shown in figure 4.5. It is an image of a kinked region in a FM1 film which has buckled under compression during its handling. Compressive failure of PBT fibers has been shown to be due to a buckling instability which is manifested in the formation of kink bands [33]. The technique developed in this study allows the visualization of the microstructure within a kink band. As shown in figure 4.5, it appears to result from sharp (close to 90°) bends of the individual microfibrils. This indicates that the microfibrils are the structural elements responsible for the compressive properties, as it is the buckling of the individual microfibrils which results in the compressive failure.

It can now be postulated why heat treatment has not been observed to enhance the compressive strength of PBT, and why a dimension on the

order of 100Å appears to be the upper limit to the width of regions of coherently packed PBT chains, as described in section 1.3.1. It is postulated that the dimensions of the microfibrils, in particular the length:width ratio, control the compressive strength of PBT. These dimensions are set in the coagulation process. All subsequent post-treatments may perfect the packing of chains within the microfibrils but do not alter the microfibrillar morphology. Any possible enhancement of the compressive properties must therefore involve the coagulation process in which the microfibrils are formed.

The propensity of the microfibrils for bending at sharp angles, as seen, for example, at the buckled region in figure 4.5, is also manifested in the image of a transversal section of the epoxy impregnated fiber. Figure 4.6 shows a transversal section, "looking down" the fiber axis, in a region close to the circumference of the fiber. The thick diagonal lines appearing within the fiber are knife marks. Their orientation indicates the cutting direction. Closer inspection reveals smaller dark striations oriented along the cutting direction. These are fragments of the microfibrils which have been bent at 90° to the fiber axis by the shear action of the advancing knife edge. The electron diffraction pattern verifies that the predominant chain orientation is along the cutting direction, perpendicular to the fiber axis! The "bent" microfibrils therefore obscure the underlying morphology in the transversal section.

In summary, the basic structural element of PBT fibers and films, which is formed in the coagulation process, has been identified as an

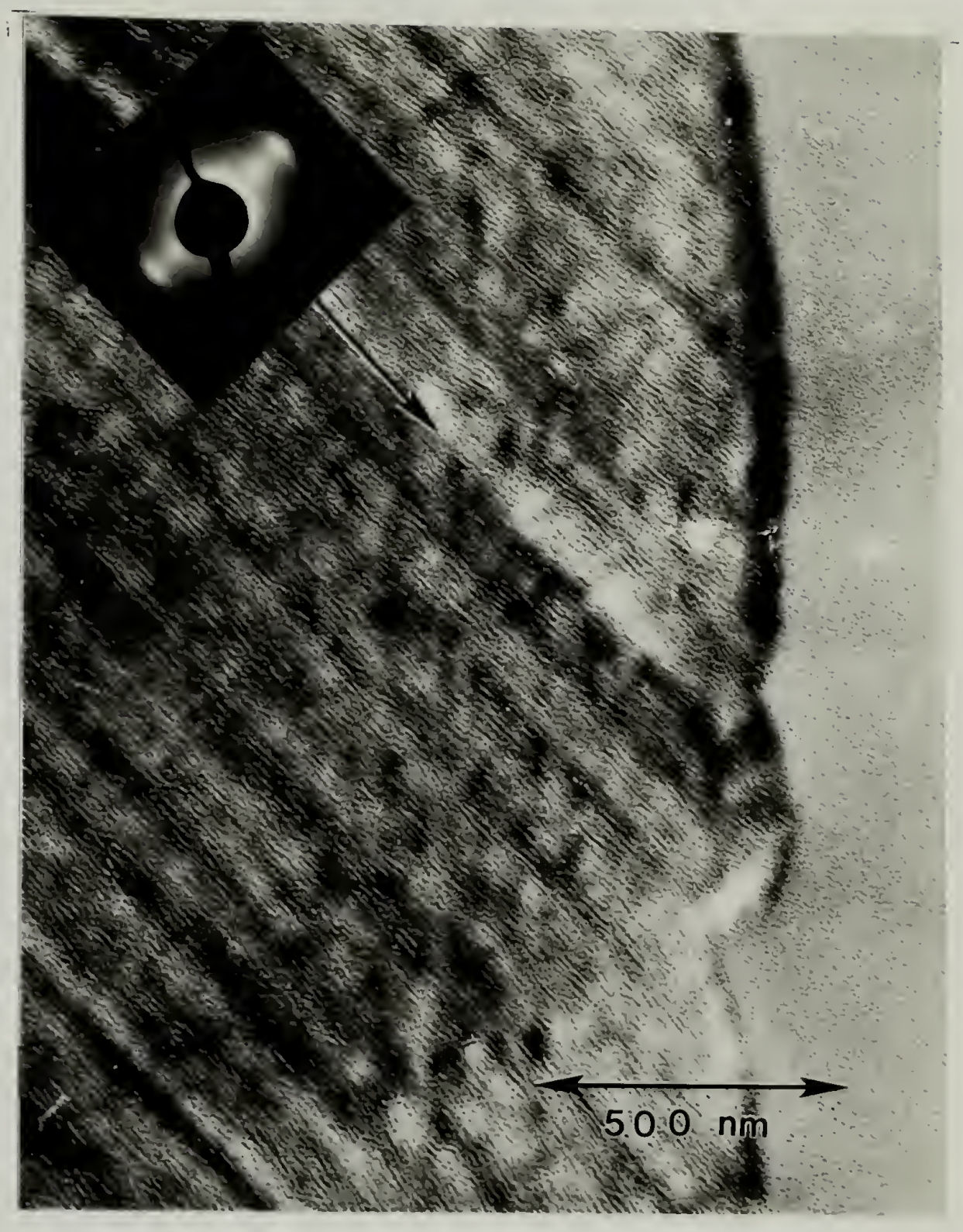

Figure 4.6. An electron micrograph of a transversal section of an epoxy-impregnated PBT fiber, near its periphery. Arrow indicates the cutting direction. Inset: a correctly aligned diffraction pattern.

interconnected network of oriented microfibrils, about 100Å in width. The relevance of the microfibrils to the compressive properties and thus the significance of the phase transition occurring during coagulation has been pointed out.

4.3 Quantification of the Morphology by SAXS

4.3.1 General Considerations

Having established that the morphology of PBT fibers and films in the wet-coagulated state is composed of long, thin microfibrils oriented along the extrusion direction, a more quantitative measure of the microfibrillar morphology can be obtained by SAXS measurements. The SAXS pattern obtained with a pinhole collimated incident beam, shown in figure 4.7, exhibits a narrow and intense equatorial streak, as expected of oriented microfibrils, the length of which is much larger than their width. Based on the electron-microscopical observation it is assumed that the microfibrils are well oriented so that a cross section of a microfibril perpendicular to the extrusion direction is a good representation of a cross section perpendicular to its axis.

The objective is now to study the structure in a cross section plane of an epoxy impregnated PBT film, perpendicular to the extrusion direction, i.e., assess the shape and arrangement of the microfibrillar cross sections. This information can be obtained by analysis of the scattering pattern from a slit-collimated incident beam, in the experimental geometry as shown in figure 3.1, since the assumptions of the derivations outlined in section 3.1 are satisfied in this experiment:

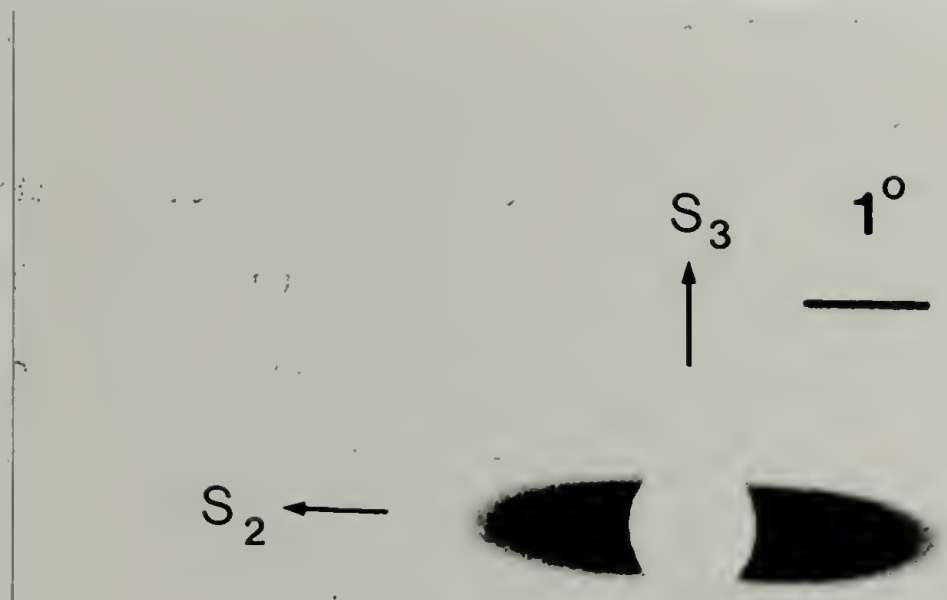

Figure 4.7. SAXS pattern from an epoxy-impregnated PBT film (FM1), using a pinhole-collimated incident beam.

(a) The scattered radiation in the S_3 direction is of negligible intensity for values of S larger than about $0.005\mathring{A}^{-1}$, as seen in figure 4.7. The beam incident on the sample is of constant intensity up to a distance of 38mm from its center point, which is equivalent to about $S=0.046\mathring{A}^{-1}$.

(b) By virtue of the continuous extrusion process by which the films were processed, the microstructure is expected to be homogeneous in the extrusion direction.

(c) The observation of a PBT fiber diffraction pattern by electron diffraction and WAXD, as well as the equivalence of the WAXD patterns obtained with the incident beam perpendicular to the front and edge faces of the film, verifies the overall cylindrical symmetry of the microstructure.

4.3.2 The Width and Density of the Microfibrils

The SAXS pattern obtained using a slit-collimated incident beam is shown in figure 4.8a after correction for detector sensitivity and subtraction of parasitic scattering. The scattered intensity $\tilde{I}(S)$, is a monotonically decreasing function of the scattering vector S. A plot of $S^3\tilde{I}(S)$ as a function of S^3, given in figure 4.8b is linear at large S. Thus:

$$\tilde{I}(S) = K_p/S^3 + F_\ell \qquad (4.1)$$

where K_p is the Porod constant for a two phase system of constant

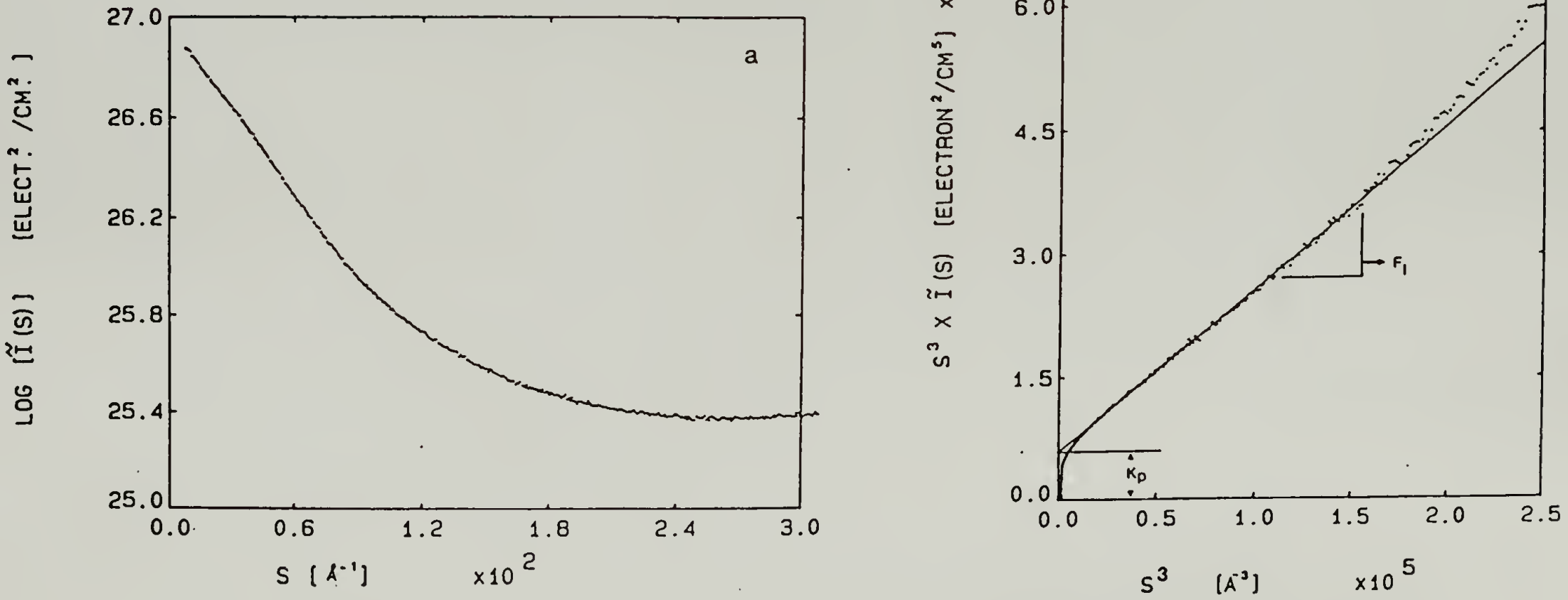

Figure 4.8. (a) SAXS pattern from the FM1 film obtained using a slit-collimated incident beam. (b) The data plotted to fit Porod's law (equation 4.1).

densities and sharp interfaces in two dimensions, as given in equation (3.28), and F_ℓ is the intensity scattered by small scale density fluctuations in one or both phases [92], which is assumed to be constant over the measured range of scattering angles. In this case F_ℓ can be seen to result mostly from the low angle tail of the amorphous halo of the epoxy matrix. The data points below $S=0.026\mathring{A}^{-1}$, at which deviations from Porod's law appear in figure 4.8a, are excluded in further analysis, and the value of F_ℓ determined from the slope in figure 4.8b is subtracted from the measured intensity.

The scattering invariant is calculated according to equation 3.30 using the experimental data and asymptotic extrapolations at the extremities of the pattern. At low angles the Guinier approximation [84] is used. Beyond $S=0.026\mathring{A}^{-1}$ the scattering pattern is extrapolated using Porod's law. The contribution to the total invariant from the low angle extrapolation is less than 2%, and from the large angle extrapolation less than 10%.

The calculation of the scattering invariant, together with independent measurement of the densities of the epoxy impregnated PBT film and the epoxy matrix, allow the determination of the volume fraction and density of the microfibrillar phase in the film. Under the assumption that the area fraction of the microfibrillar phase in the cross section is equal to its volume fraction in the film, v_f, equation (3.30) written in terms of mass densities instead of electron densities, yields:

$$\frac{Q}{L\lambda}\left(\frac{M_f}{Z_f N_{AV}}\right)^2 = \left(d_f - d_m \frac{Z_m M_f}{Z_f M_m}\right)^2 V_f(1-V_f) \qquad (4.2)$$

where M_f and M_m are the molecular weights, and Z_f and Z_m are the number of electrons per repeat unit of PBT and the epoxy resin respectively; d_f and d_m are the densities of the respective phases and N_{AV} is Avogadro's number. In addition, assuming all voids are filled with the epoxy resin, the film density, d, can be given as:

$$d = d_f v_f + d_m(1-V_f) \tag{4.3}$$

From the chemical structure of both PBT and the epoxy resin M_f=266, Z_f=136, M_m=200, and Z_m=109. By measuring Q, d and d_m, equations (4.2) and (4.3) can be solved for the density and volume fraction of the microfibrillar phase. From the Porod constant determined in figure 4.8b the interfacial contour length and the average diameter of the microfibrils are obtained using equations 3.28 and 3.31. These measurements and results are summarized in Table 4.1.

The average microfibrillar diameter determined from the scattering pattern, 71Å, is in agreement with the observations by electron microscopy. The calculated volume fraction, 0.18, indicates that volume shrinkage has occurred during the coagulation and/or the impregnation processes, as the weight fraction of PBT in the initial solution was about 0.06. The density of the microfibrils, calculated as 1.46 g/cm^3, is smaller than the density of the PBT crystal, estimated as 1.69 g/cm^3 [26]. This indicates the existence of a significant number of defects within the individual microfibril.

The presence of defects in the lateral packing of PBT chains is also suggested by the small width of PBT crystallites in the "as-spun" state. Minter et al. [36] observed regions of coherently packed PBT

Table 4.1. Analysis of the SAXS Pattern From Epoxy-impregnated PBT Film (FM1)

Measurements:	
scattering invariant	$Q = 1.1 \times 10^{39}$ elect.^{2}/cm^4
Porod constant	$K_p = 5.9 \times 10^{43}$ elect.^{2}/cm^5
film density	$d = 1.15$ g/cm^3
density of epoxy matrix	$d_m = 1.08$ g/cm^3
Results:	
volume fraction of microfibrils	$v_f = 0.18$
density of microfibrils	$d_f = 1.46$ g/cm^3
interfacial length/unit volume	$C/A = 0.010 A^{-1}$
average diameter of microfibrils	$\bar{D} = 71 \mathring{A}$

chains about 20Å in width, which increased to about 100Å upon heat treatment. The microfibrils in PBT may thus be composed of smaller elements in which the chains are coherently packed, with the imperfections between these elements resulting in a lower overall density. These imperfections may be removed by heat treatment leading to a coherent packing of chains with a lateral dimension on the order of the microfibrillar width.

4.3.3 Models for the Shape and Packing of the Microfibrillar Cross-sections

The width of the microfibrils has been calculated using the large angle part of the scattering pattern (the "Porod region"). More information about the shape and packing of the cross sections of the microfibrils may be obtained by simulation of the complete scattering pattern using more detailed models of the microfibrillar cross-sections.

Three models are considered in the simulation of the scattering pattern: hard discs, semipenetrable discs, and a random two-phase structure, as shown schematically in figure 4.9. The simulated pattern of the first two models is calculated using equation 3.48. The form factor is calculated using equations 3.60 and 3.61, with a Gaussian distribution of disc diameters having $\bar{D}$=71Å and a standard deviation of 20Å. (A distribution of such breadth is required to suppress the form factor peaks as these are not observed experimentally.). The impenetrable and semipenetrable disc models differ in the prescribed interference factor used in equation 3.48. The interference factor of a hard disc fluid, in which the discs have a diameter of 71Å and cover an area

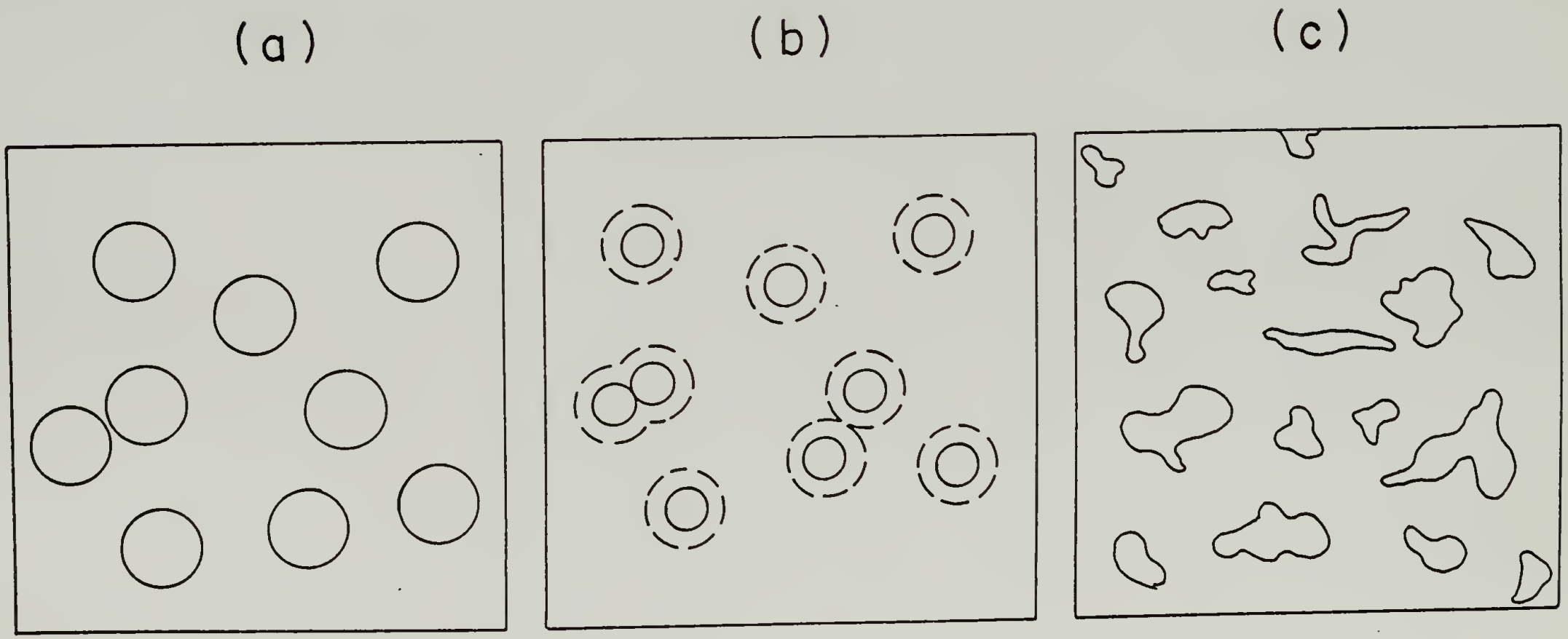

Figure 4.9. A schematic representation of the models used in simulation of the scattering pattern: (a) hard discs, (b) semipenetrable discs, (c) a random two-phase structure.

fraction of 0.18, is used in the first model. For the semipenetrable disc model, the interference factor is calculated for a hard disc fluid having the same number of discs per unit area as the previous model, but with a smaller apparent diameter, hence a smaller apparent area fraction. This allows the minimal distance between the centers of the discs to be less than the average disc diameter, as shown in figure 4.9b, and may simulate the cross-section of a junction between microfibrils. In the third model the structure in the cross section of the film is simulated as a random two-phase structure.

The three simulated patterns are compared with the experimental measurement in figure 4.10. The intensity at zero angle is set to be equal for the measurement and simulations. The hard disc model fits the experimental data poorly. A better fit at the large angle part of the scattering pattern is obtained with the semipenetrable disc model, using an apparent hard disc diameter $D_a = 0.8\bar{D}$ in the calculation of the interference factor. Both models fail in the smaller angle part of the scattering pattern, where the higher intensities predicted by these models are a direct consequence of the spatial correlations between the hard or semipenetrable discs.

A good fit of the experimental data is obtained with the random two phase structure model in the entire experimentally accessible range. It is obtained using a correlation length of 36Å, which is estimated from a plot of $\tilde{I}(S)^{-2/3}$ as a function of S^2 shown in figure 4.11. A linear fit is predicted by equation 3.37. This suggests that the cross sections of the microfibrils have irregular shapes. The average cord length of the

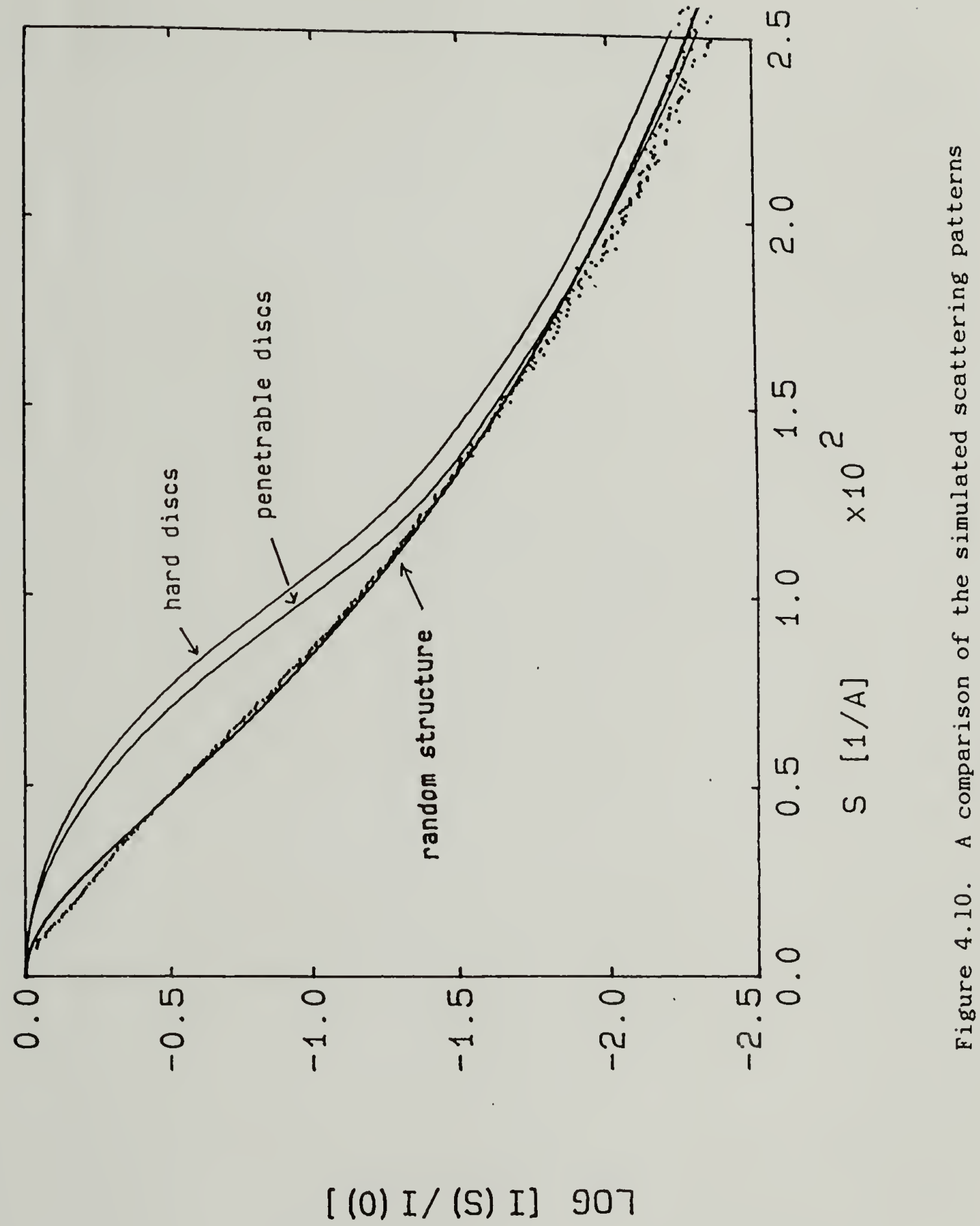

Figure 4.10. A comparison of the simulated scattering patterns with the experimental data.

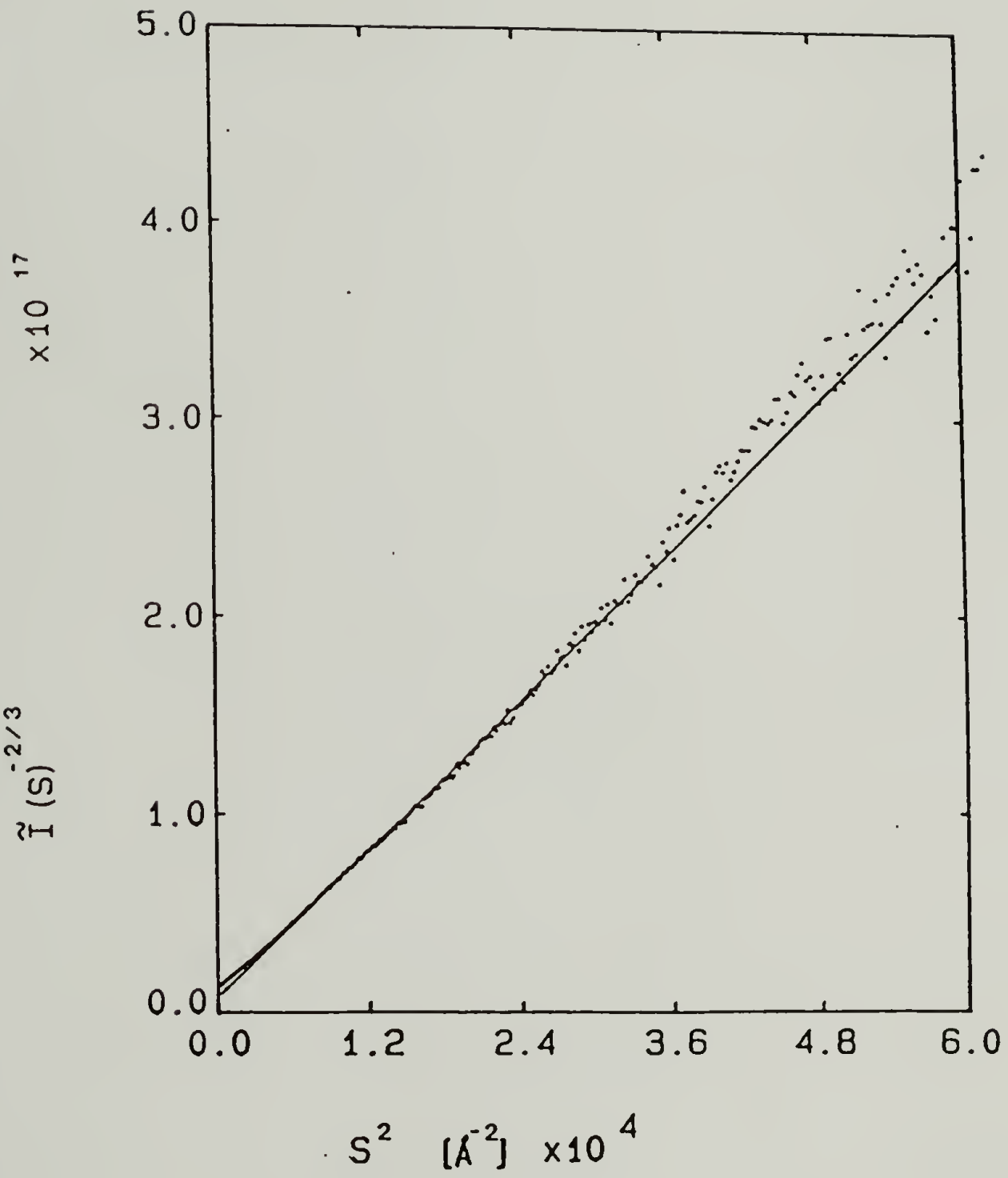

Figure 4.11. A plot of $\tilde{I}(S)^{-2/3}$ as a function of S^2, to fit equation (3.37).

microfibrillar cross sections, ℓ_f, as defined by Porod [80], is given by:

$$\ell_f = \ell_c/(1-v_f) \tag{4.4}$$

the value of ℓ_f thus calculated, 44Å, is smaller than the observed dimension of the microfibrils. In addition the interfacial contour length per unit area calculated from the correlation length by equation 3.36, $0.013 Å^{-1}$, is larger than calculated from Porod's law. This may reflect the fact that in using Porod's law the information is obtained from the large angle part of the scattering pattern, whereas equation 3.37 is fit to the entire pattern, giving more weight to the smaller angle region.

In conclusion, SAXS measurements yield quantitative information about the microfibrillar morphology: average width of 71Å, density 1.46 g/cm^3 and a volume fraction of 0.18 in the epoxy impregnated film. The microfibrils are shown to have irregularly shaped cross-sections.

4.4 The PBT/Poly (Phosphoric Acid) Crystal-Solvate Phase

The formation of a crystal-solvate phase in isotropic solutions of PBT in MSA under the influence of moisture [37,38] has motivated an investigation of the formation of crystal solvates in a monodomain nematic solution of PBT in PPA. Polyphosphoric acid is a mixture of oligomers of the phosphate monomer $+PO_3H)_n^-$, in which the equilibrium distribution of oligomer lengths is a function of the P_2O_5/H_2O ratio of the compound [93]. The coagulant chosen for this experiment was commercial phosphoric acid (85% H_3PO_4, 15% water) as the phosphate anion,

being a weaker base than water, is expected to be a slower coagulant. In this way the coagulation medium is well defined (compared with atmospheric moisture), and the coagulating solution is maintained within the P_2O_5/H_2O system, for which the chemical transitions and their kinetics are well known [93]. At room temperature PPA is stable towards hydrolysis for several weeks even at low pH. Therefore the only reaction expected to occur in the coagulation medium used is proton transfer. At 90°C and pH of 4, hydrolysis is expected to occur with a rate constant of a few seconds [93].

Within one hour after immersion in the coagulation medium, at room temperature, the oriented PBT/PPA solution exhibits a striking color change from green to bright red, and appears to have the mechanical integrity of a solid. A change of color to dark yellow is induced when the red phase is washed with water, and is similar to the color of films coagulated directly in water. Formation of a solid red phase in the PBT/MSA/water system has been attributed to aggregation of deprotonated PBT molecules [98] or to formation of a crystal-solvate phase [37,38]. Characterization of the structure and formation of the red phase in the PBT/PPA system is the subject of this investigation.

The evolution of structure in the formation of FM2P and FM2W films under the processing conditions described in section 2.1.1 (Table 2.1) can be followed with the aid of the WAXD patterns shown in figure 4.12. Figure 4.12a is the diffraction pattern from the PBT/PPA solution prior to coagulation. In addition to the diffuse rings due to the isotropically oriented solvent, it exhibits a broad equatorial reflection at a

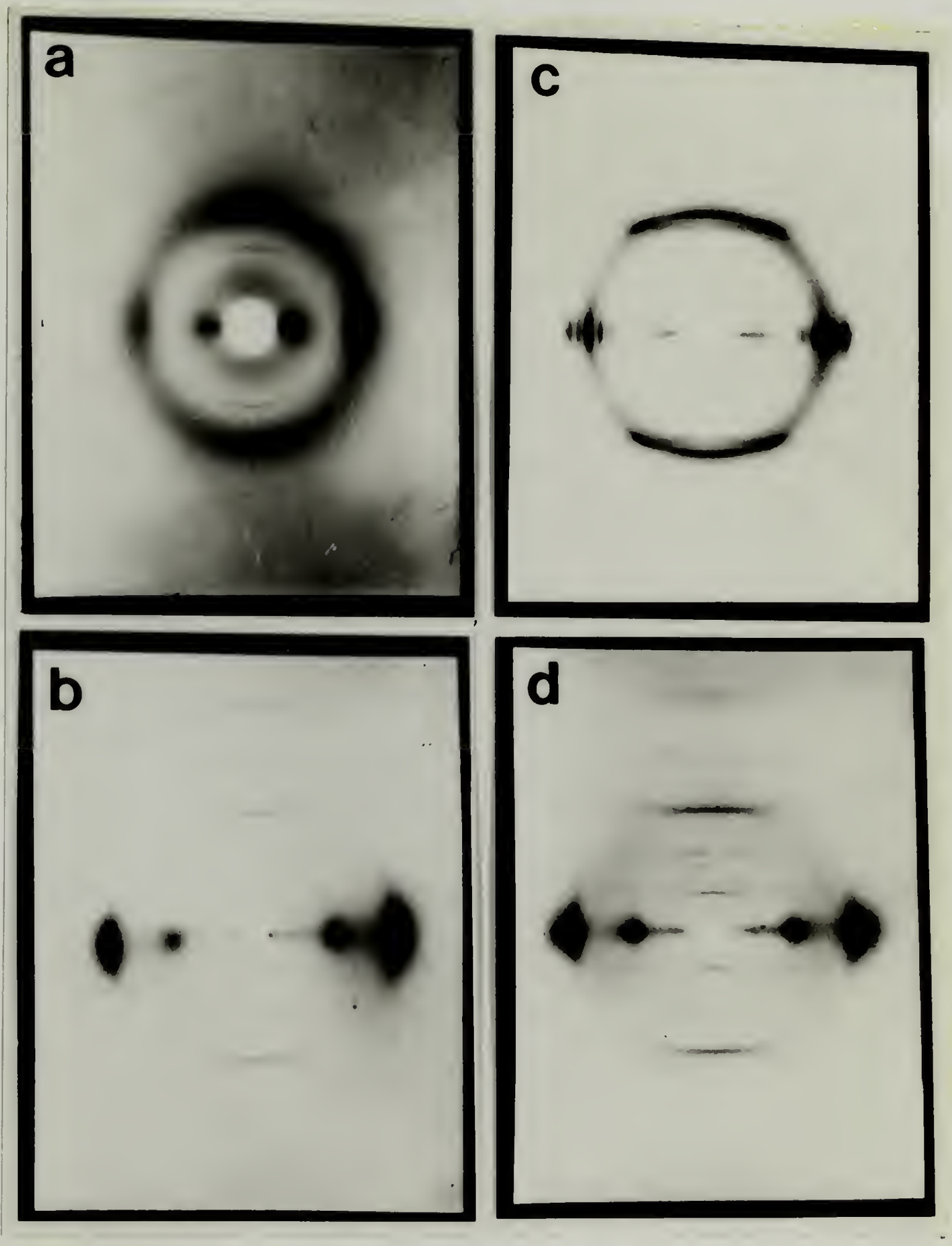

Figure 4.12. Wide angle X-ray diffraction patterns from: (a) the oriented PBT solution in PPA, (b) the dried, water-coagulated film (FM2W), (c) the solution coagulated in phosphoric acid, (d) the dried, acid coagulated film (FM2P).

spacing of about 15.5Å, and diffuse layer lines at the characteristic spacings due to the PBT repeat unit. This pattern is typical of the oriented nematic state, and thus characterizes the initial state of the solution as such. The relatively high intensity on the second PBT layer line, which is nearly extinct in the molecular transform of the isolated PBT molecule [27] as well as in diffraction patterns of solid PBT [25-28], indicates that the PBT molecule in the PPA solution is not isolated or aggregated with other PBT molecules, but is associated, possibly with the PPA anion. When the solution is coagulated in water and subsequently dried, as in the usual spinning process, the diffraction pattern typical of PBT in the as-spun state is observed, as shown in figure 4.12b.

The diffraction pattern from the film coagulated in phosphoric acid (the "red" phase) shown in figures 4.12c and 4.13 represents a new structure which has not been previously observed. Its significant features are several sharp equatorial reflections at spacings which are not common to solid PBT, off-meridional reflections indicating a degree of three-dimensional order which is absent in PBT, and a layer line at a meridional spacing of 4.6Å which is incommensurate with the layer line spacings of the normal PBT fiber diffraction pattern.

The tentative indexing of the diffraction pattern is shown in figure 4.13 and table 4.2. The reflections index on an orthorhombic unit cell of dimensions:

$$a = 15.88\text{Å};\ b = 20.64\text{Å};\ c\ (\text{chain axis}) = 36.90\text{Å}$$

The radial streaks near the center of the diffraction pattern in figures

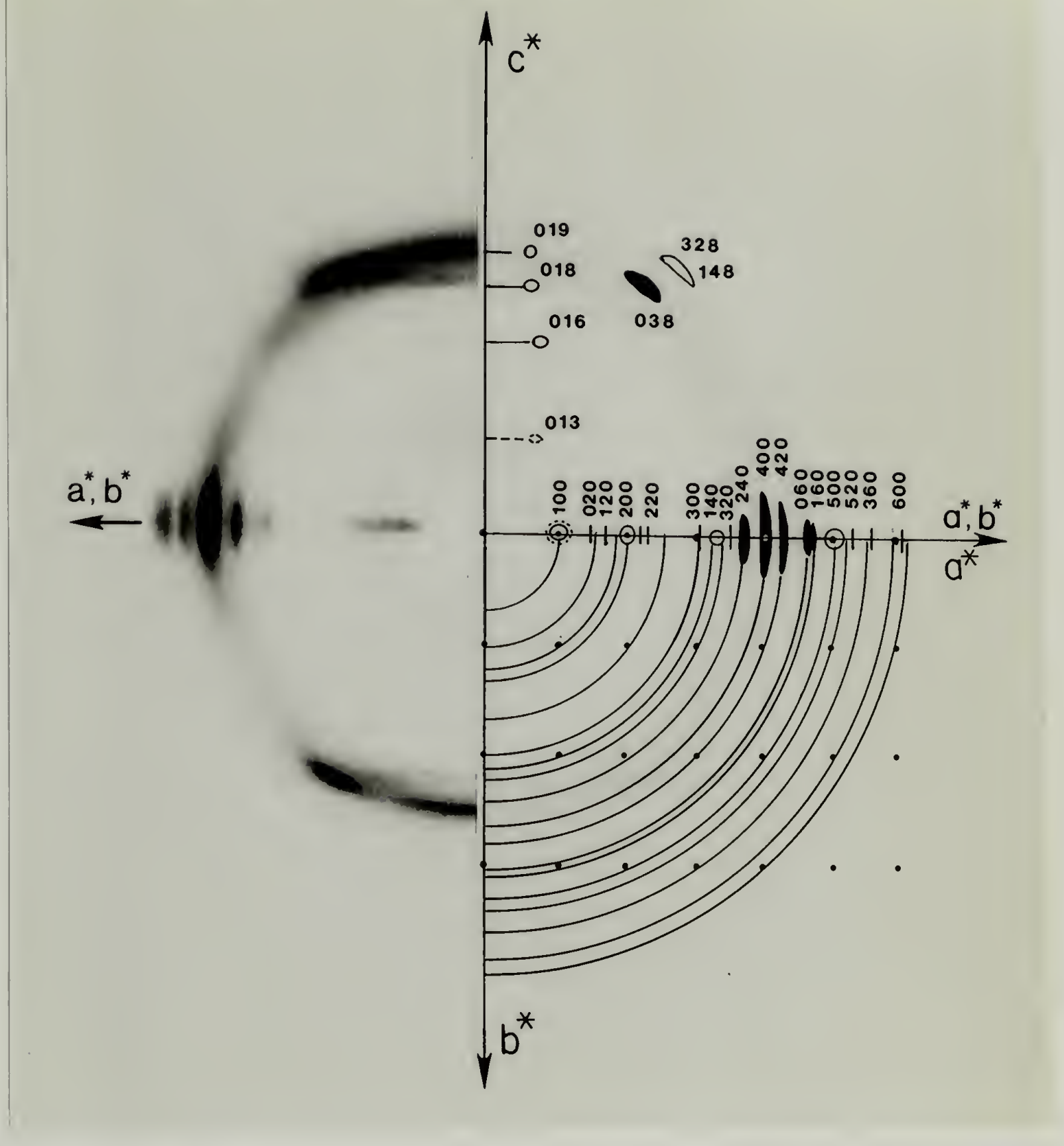

Figure 4.13. X-ray diffraction pattern from the PBT/PPA crystal-solvate.
At left: one half of the symmetric diffraction pattern.
Top right: a schematic representation of the diffraction pattern.
Bottom right: the equatorial plane of the reciprocal lattice: a rectangular net having spacings of a^* and $2b^*$.

Table 4.2. Comparison of Measured and Calculated d-Spacings for the PBT/PPA Crystal-Solvate (orthorhombic unit cell a=15.88, b=20.64, c=36.9Å)

Miller Indices (hkℓ)	d (measured) Å	d (calc.) Å	Comments
(A) Equatorial Reflections			
100	15.6*	15.88	weak
020	10.8	10.32	very weak
120	9.3	8.65	very weak
200	8.0	7.94	weak
	7.41	-	very weak
220	6.8	6.29	very weak
040, 300	5.2	5.16, 5.29	very weak
140	4.87	4.91	weak
320	4.59	4.71	very weak
240	4.35	4.33	medium
400	3.97	3.97	very strong
340, 420	3.70	3.69, 3.71	medium
060	3.51	3.44	strong
160	3.37	3.36	medium
260, 440, 500	3.28	3.16, 3.15, 3.18	very weak
520	3.03	3.04	weak
360	2.87	2.88	very weak
540, 600	2.68	2.70, 2.65	very weak
(B) Off Meridional Reflections			
016	5.88	5.89	diffuse
018	4.48	4.50	diffuse
019	3.99	4.02	diffuse
038	3.84	3.83	strong
328, 148	3.33	3.30, 3.36	medium
(C) Layer Line Spacings			
ℓ = 3	12.11	12.3	
6	6.13	6.15	
8	4.59	4.61	
9	4.06	4.10	
12	3.06	3.08	
15	2.54	2.46	

*from D-500 diffractometer

4.12c and 4.13 are due to radiation of continuous wavelength which has not been adequately filtered. In particular the streaks along the equator obscure the low angle reflections. This problem is somewhat alleviated in the diffractometer trace shown in figure 4.14, where a peak corresponding to a 15.9Å spacings and a shoulder at about 7.9Å can be observed. The indexing of the equatorial reflections (hk0) on a rectangular net of dimensions (a*, 2b*) is shown in figure 4.13. By this assignment, the unit cell of the c-axis projection is a rectangle of dimensions 15.88Å and 10.32Å. The larger equatorial net needed to index the three dimensional pattern is thus due only to a shift of the chains in the c-axis direction.

The diffraction pattern in figures 4.12c and 4.13 is interpreted as arising from the crystal-solvate phase formed by cocrystallization of PBT and PPA. It is analogous to the crystal solvate phase in the PBT/MSA system [37,38], but differs from it by the oligomeric nature of the solvent. The PBT chains and the PPA oligomers co-crystallize parallel to each other, in an overall uniaxial orientation dictated by the extensional flow during the spinning process. Crystallizable polyelectrolyte complexes of the polyphosphate anion with flexible polybases, such as polyvinylpyridine, have been reported [95,96]. This is believed to be the first report of such a complex with a rodlike polymer, obtained from a monodomain nematic state.

The origin of the layer line at 4.6Å meridional spacing, on which the intense off meridional reflections are found, can be postulated with reference to the crystal structures of polyphosphate salts [94].

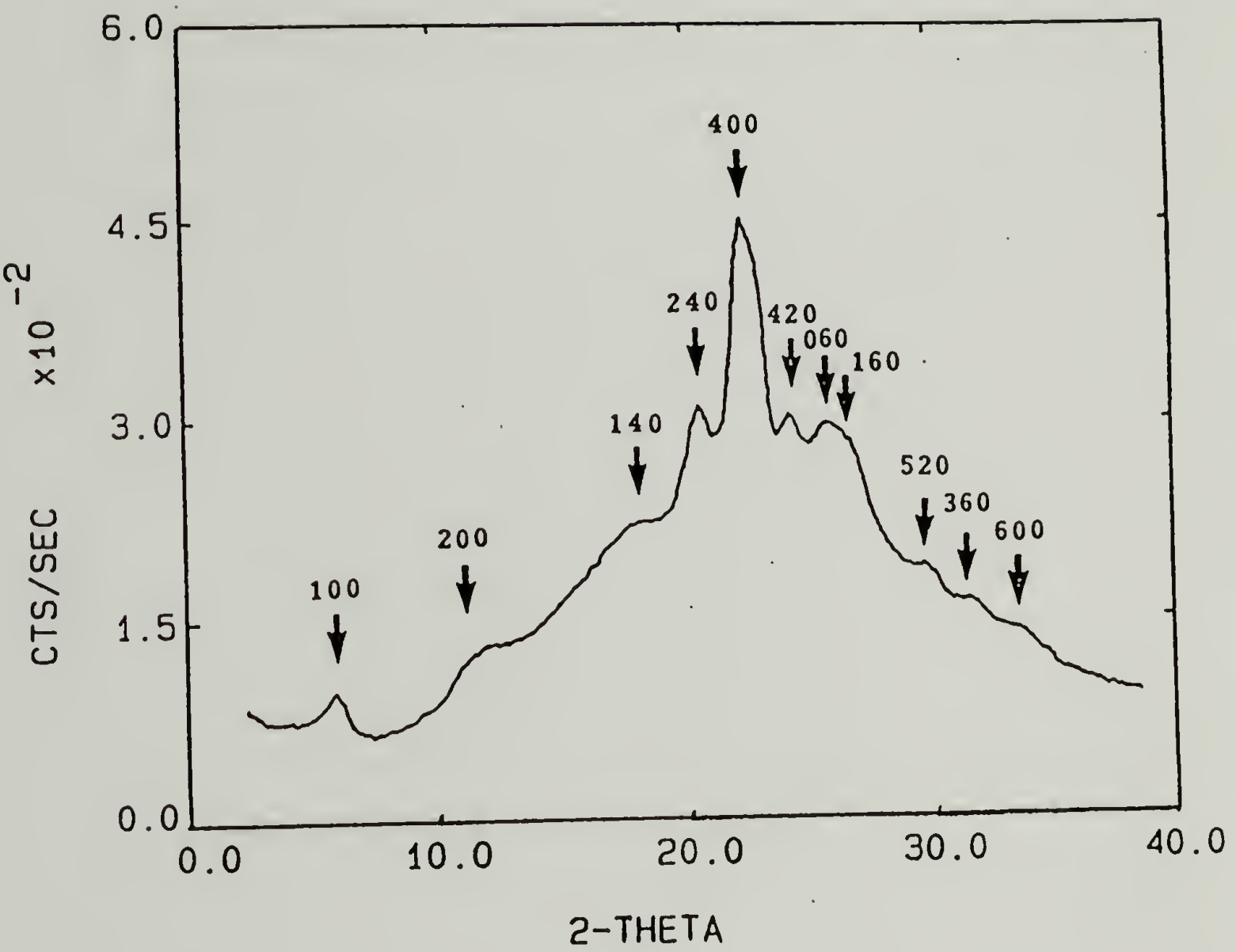

Figure 4.14. A diffractometer scan of the equatorial reflections of the PBT/PPA crystal-solvate.

Several conformations of the polyphosphate anion having a chain axis repeat length between 4.2Å and 7.0Å have been described, depending on the nature of the counterion and temperature, as shown in figure 4.15. The tetrahedral elements in figure 4.15 represent the phosphate group having oxygens at the apices and phosphorus at the center. In particular, the 2/1 helical conformations of PPA in its salts with Lithium and Rubidium, having two phosphate groups in a repeat length of 4.2Å and 5.2Å respectively, suggest the possibility of a similar conformation with a repeat length of 4.6Å in the co-crystal with PBT. In such case the reflections on layer lines which are orders of the polyphosphate repeat length are expected to be of high intensity, due to the large electron density of phosphorus, as is indeed observed. The assignment of the 4.6Å meridional spacing to a unit composed of two phosphate groups implies that along the c-axis dimension of the unit cell there are three PBT monomer units and sixteen phosphate groups (in eight repeat units).

The length of the PPA oligomers in this system is not known, as PPA is condensed during the polymerization of PBT by addition of P_2O_5 to the reaction mixture. The most probable species in a P_2O_5/H_2O system having an equivalent P_2O_5 content (87.6%) is a trimer [93]. As the acidity of a PPA oligomer increases with chain length [93], it is conceivable that the PPA oligomers which are associated with PBT by proton transfer are the longer chains in the distribution. Irrespective of their length, it is postulated that the PPA oligomers are aligned along the c-axis of the crystal solvate in such a way that a repeat distance

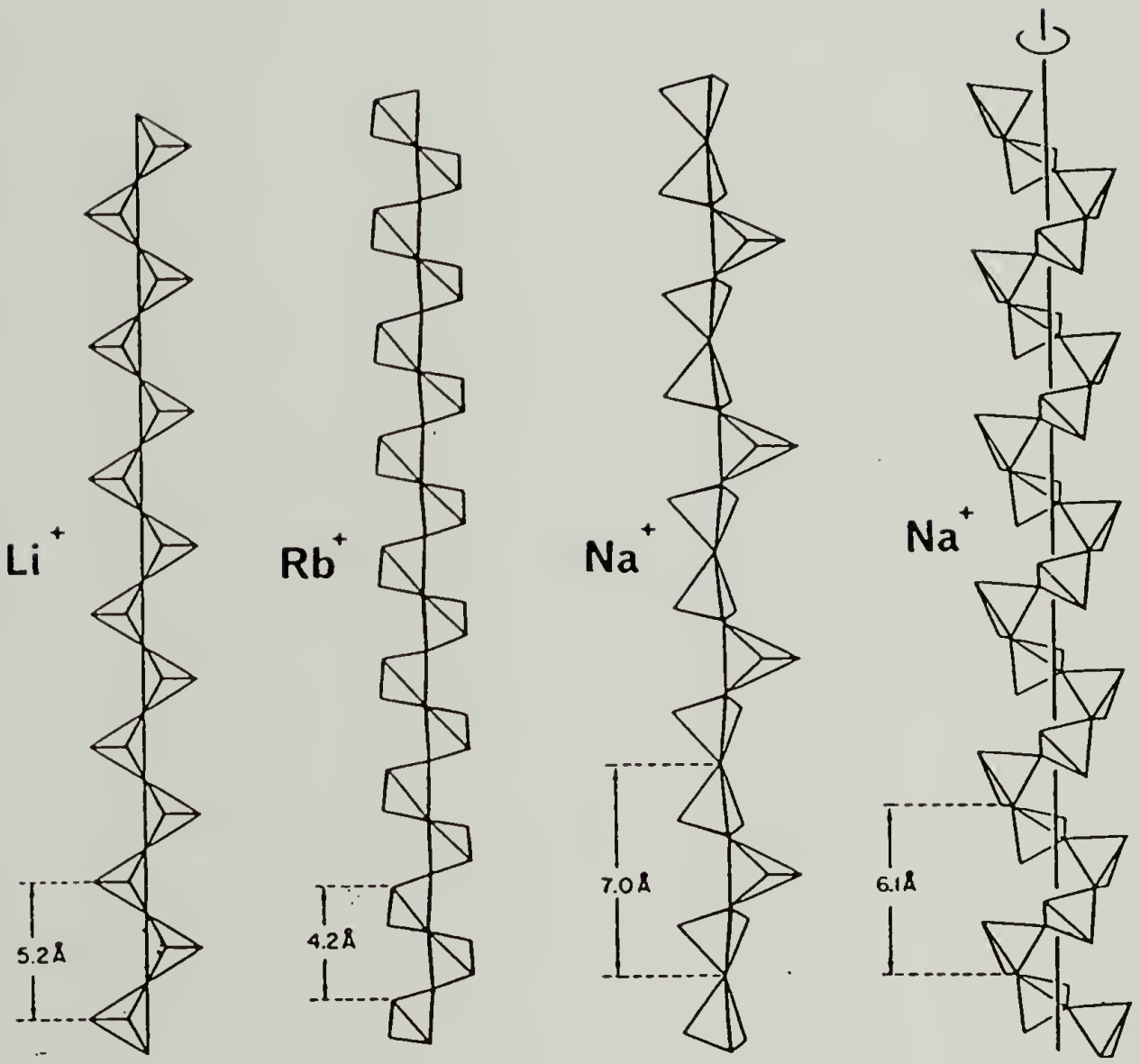

Figure 4.15. A schematic representation of the conformation of the PPA anion in salts with various cations (from ref. [94]).

of 4.6Å in which there are two phosphate groups, is obtained parallel to the PBT chain axis.

The formation of a crystal-solvate phase is supported by thermal analysis. The DSC trace of the phosphoric acid coagulated PBT/PPA solution, shown in figure 4.16, exhibits a very sharp transition at about 250°C. This transition, although reproducible in several samples, is not reversible as it appears only in the first heating. For comparison, trace (b) in figure 4.16 is due to a mixture of 50% PPA, 42.5% H_3PO_4 7.5% water, which is taken to represent the components of the system in the absence of PBT. (The trace is plotted on the same ordinate scale by assuming the mixture to represent 75% of the weight of the coagulated PBT solution.) Clearly the relative amounts given above are arbitrary, as the composition of the coagulated film is not known. Nevertheless it demonstrates that the sharp transition at 250°C is due to the presence of PBT in system. It also demonstrates the gradual hydrolysis of PPA which occurs even at low temperatures but is accelerated above 200°C [93].

The sharp peak at 250°C is attributed to the melting of the crystal solvate:

PBT/PPA co-crystal → PPA + PBT crystal

The PPA oligomers which have been "locked" in the co-crystal with PBT are then released into the acidic environment at the elevated temperature. This results in rapid hydrolysis, that would have otherwise occurred more gradually at lower temperatures. Once PPA is hydrolyzed,

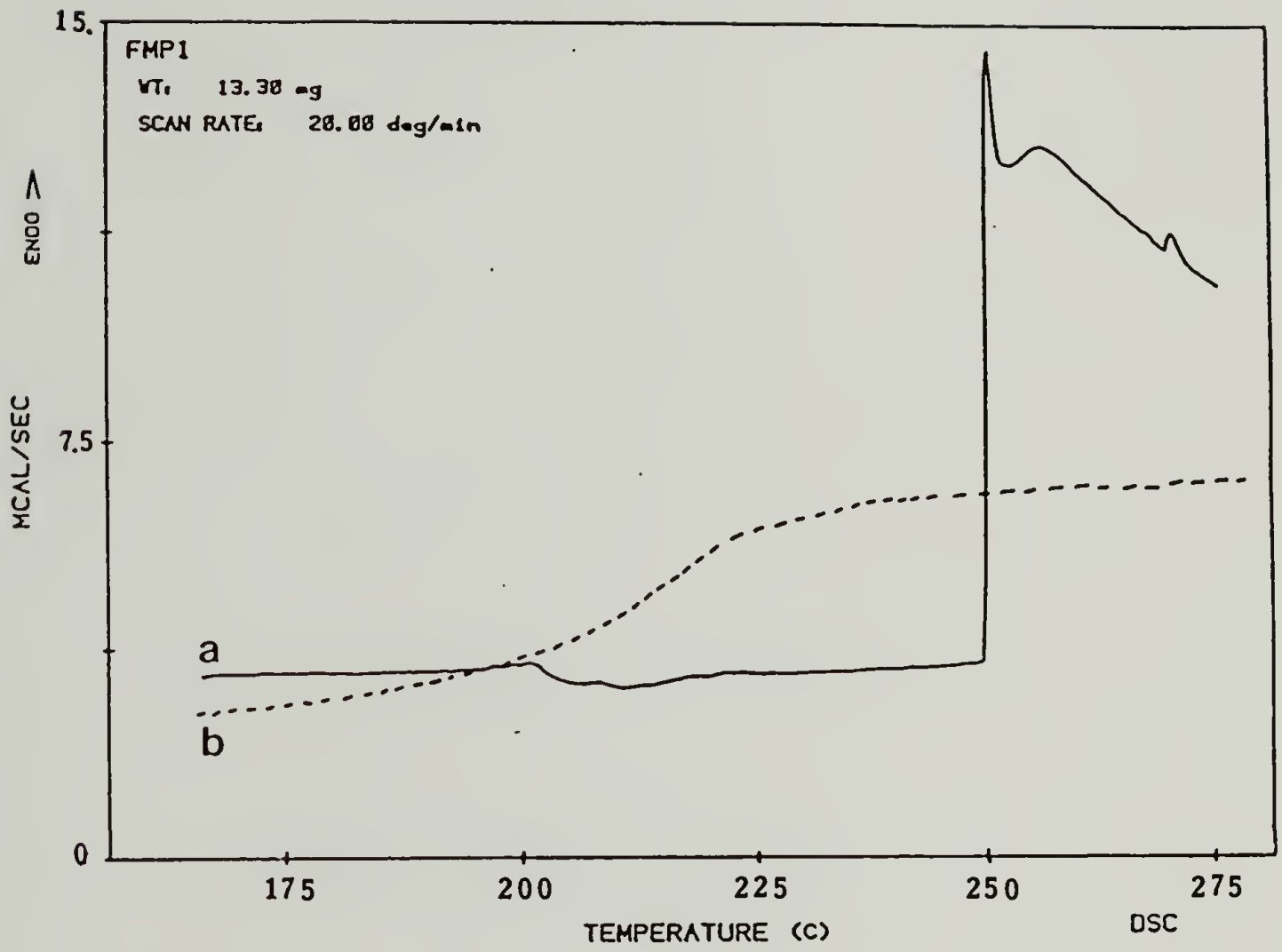

Figure 4.16. Differential scanning calorimetry of: (a) the PBT/PPA solution coagulated in 85% phosphoric acid, (b) a mixture of PPA and 85% phosphoric acid.

the phosphoric acid which is formed is not acidic enough to dissolve PBT, and hence the transition is not reversible.

The sequence of events leading to formation of the crystal-solvate is envisaged as follows: since the 15% water in the coagulant is protonated, coagulation is induced by the phosphate anion. As it diffuses into the PBT/PPA solution it deprotonates the PPA oligomers, the strongest acids in the system, which then complex and co-crystallize with the protonated PBT cations. It is possible that the deprotonation and complexation/crystallization are cooperative, in the sense that the PPA oligomers, which are already associated with PBT due to previous proton-exchange, will be deprotonated in preference of other molecules. Such cooperativity has been reported in the complexation of the PPA anion with basic oligomers [97].

The stoichometry of the crystal solvate cannot be resolved by the present experiments. Some predictions may be made by considerations of charge neutrality and unit cell density, under the following assumptions:

(a) The PPA anions are arranged parallel to the PBT chains such that there are 16 phosphate groups (8 repeat units of 4.6Å each) along the C-axis of the unit cell, either as a single chain or as shorter "runs" of oligomers.

(b) All the PAA repeat units have the same degree of deprotonation.

(c) Water (or H_3O^+) is excluded from the crystal.

Under these assumptions the ratio of PBT to PPA "chains" should be 8m:3n; where m and n are integers. The unit cell densities calculated for some possible stoichiometries are given in table 4.3. The model having a stoichiometry of $(H_2\text{-PBT})^{+2}(P_2O_6H)^{-}_2$, whereby each PBT monomer is doubly protonated, and only every other phosphate (i.e., every PPA repeat unit) is deprotonated, for which the density is 1.93 g/cm^3, seems reasonable considering the densities of PBT (1.69 g/cm^3) and PPA ($\sim$2.0 g/cm^3).

4.5 The Effect of Coagulation via the Crystal Solvate Phase on the Microfibrillar Morphology

The formation of a crystal solvate phase demonstrated in the preceding section offers an alternative route for the transition from the oriented nematic solution to the solid fiber or film. After immersion in phosphoric acid (for about 24 hours) the coagulated film has been transferred to a water bath and subsequently dried. Its morphology is compared in this section to that of a film formed from the same initial solution by coagulation in water. The WAXD patterns of the water coagulated (FM2W) and acid coagulated (FM2P) films are shown in figures 4.12(b) and 4.12(d) respectively, and the diffractometer trace of their equatorial reflections in figure 4.17. By comparison of the curvature of the layer lines and the azimuthal spread of the equatorial reflections, it is apparent that better orientation of PBT chains along the extrusion direction is achieved in the acid-coagulated film. Moreover the sharpness of the equatorial reflections of the acid-coagulated film

Table 4.3. Unit Cell Densities for Possible Stoichiometries of the Crystal Solvate

Stoichiometry	Chains/Unit Cell PBT	PPA	Density g/cm^3
$(H_2PBT)^{+2}(PO_3^-)_2$	8	3	1.40
$(H_2PBT)^{+2}(P_2O_6H)_2^-$	8	6	1.93
$(HPBT)^+(PO_3^-)$	16	3	2.27

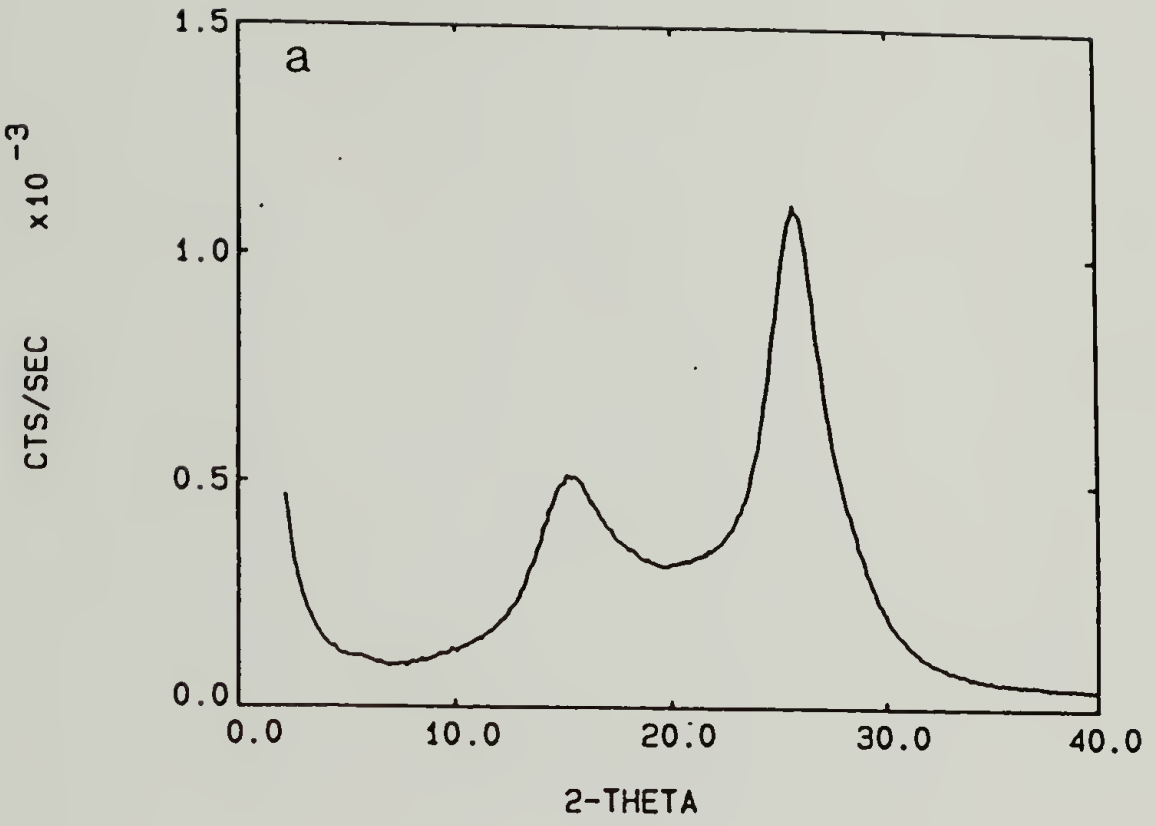

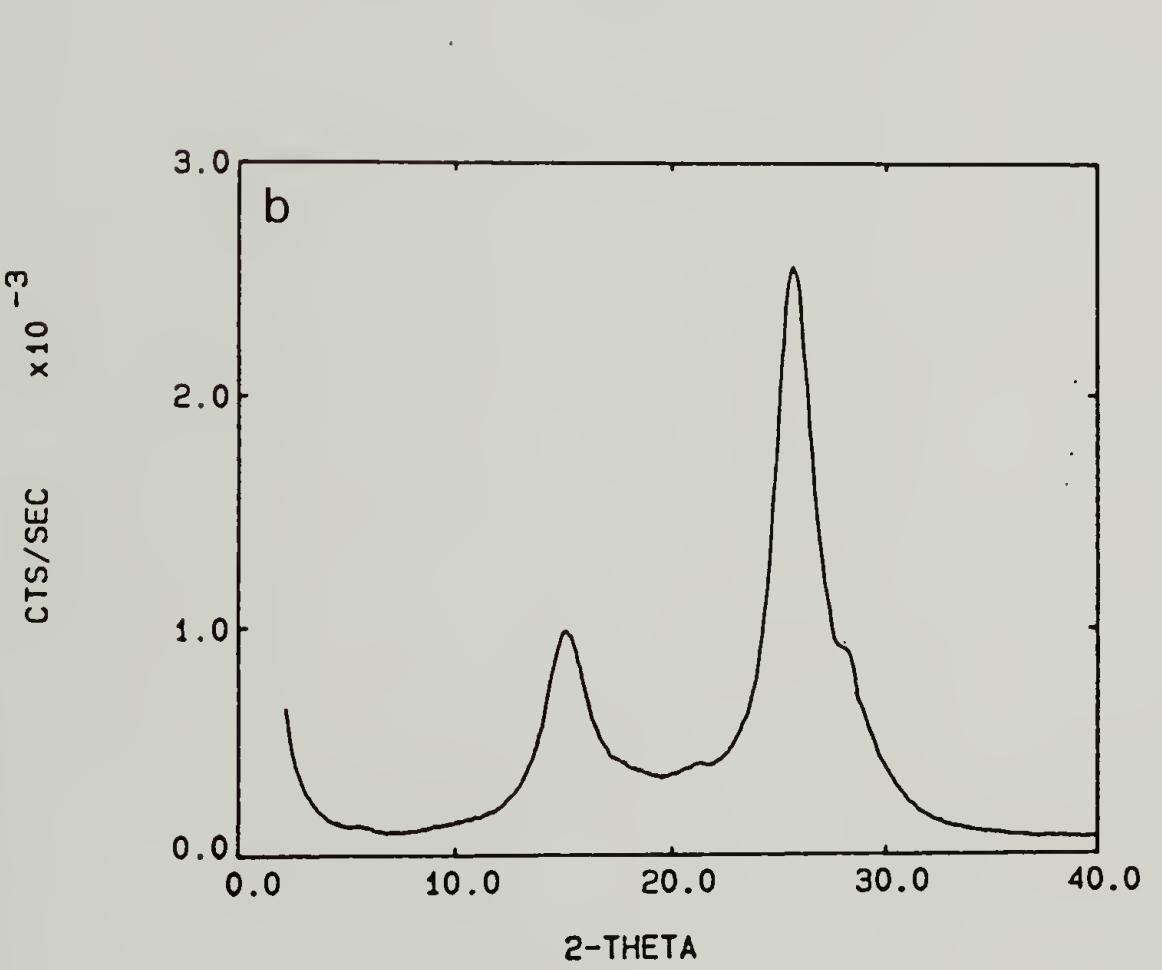

Figure 4.17. Diffractometer scan of the equatorial reflections of the dried PBT films: (a) water coagulated (FM2W), (b) acid coagulated (FM2P).

indicates a higher degree of lateral packing of the PBT chains. An estimation of the lower limit of the extent of lateral packing from the width of the reflections at 15° (d=5.9Å) in figure 4.17 (not corrected for instrumental broadening or paracrystallinity) yields about 10Å for the water coagulated film and 40Å for the acid coagulated one. In figures 4.12(d) and 4.17(b) it can be seen that the equatorial reflection at 25° (d=3.54Å) can be resolved into two reflections. This is usually seen only after heat-treatment and indicates that the degree of order achieved by acid-coagulation may be approaching that which results from heat treatment.

The effect of acid-coagulation on the microfibrillar morphology has been studied by SAXS and TEM of epoxy impregnated FM2W and FM2P films. The acid-coagulated film was washed in a water bath, to remove the acid, before infiltration with the epoxy resin. It should be emphasized that these structures relate only to the water washed film. It is not clear to what extent the morphology of the crystal solvate phase is preserved in the washing process. It is evident from figure 4.12 that the three-dimensional order achieved in the crystal solvate phase is lost by the subsequent immersion in the water bath. The results of the SAXS measurements, which have been analyzed using the methods described in sec-section 4.2, are given in table 4.4. They indicate that within the margin of error of these measurements there is no significant difference in the width, density and volume fraction of the microfibrils formed by the two processes.

Table 4.4. Results of SAXS Measurements from Epoxy-Impregnated FM2W and FM2P Films

Coagulant	Film Density gr/cm^3	Microfibrillar Characteristics: Volume fraction	Density gr/cm^3	Diameter A
Water	1.15	0.25	1.46	67
Phosphoric acid	1.19	0.28	1.48	85

The morphology of the water-coagulated film observed by TEM is shown in figure 4.18a. The micrograph shown is typical of the regions which could be visualized. The morphology of the acid coagulated film was not homogeneous. The majority of the regions observed exhibited the morphology shown in figure 4.18b. Comparison of figures 4.18(a) and 4.18(b) demonstrates that the microfibrils in the two preparations are of comparable width, with the ones in the acid coagulated film being better oriented. The appearance of slightly wider microfibrils in figure 4.18(a) is due to a larger underfocus of the objective lense used in its imaging.

Some regions in the acid coagulated film exhibited a different morphology than that shown in figure 4.18b. The micrograph in figure 4.19 is an example of such regions. A thick microfibril, the width of which is traversed by horizontal bands, can be observed. Its boundaries are indicated by vertical bars. The origin of the transverse banding is not clear, but it is taken to indicate the width of the microfibril. This suggests the possibility that microfibrils having a width on the order of 500Å have been formed by coagulation in phosphoric acid.

4.6 Conclusions

Direct observation by electron microscopy demonstrates that the basic structural element formed in the coagulation of a monodomain nematic PBT solution is an interconnected network of highly oriented microfibrils. The width of the microfibrils is observed to be about 100Å. SAXS measurements yield quantitative information about the microfibrillar

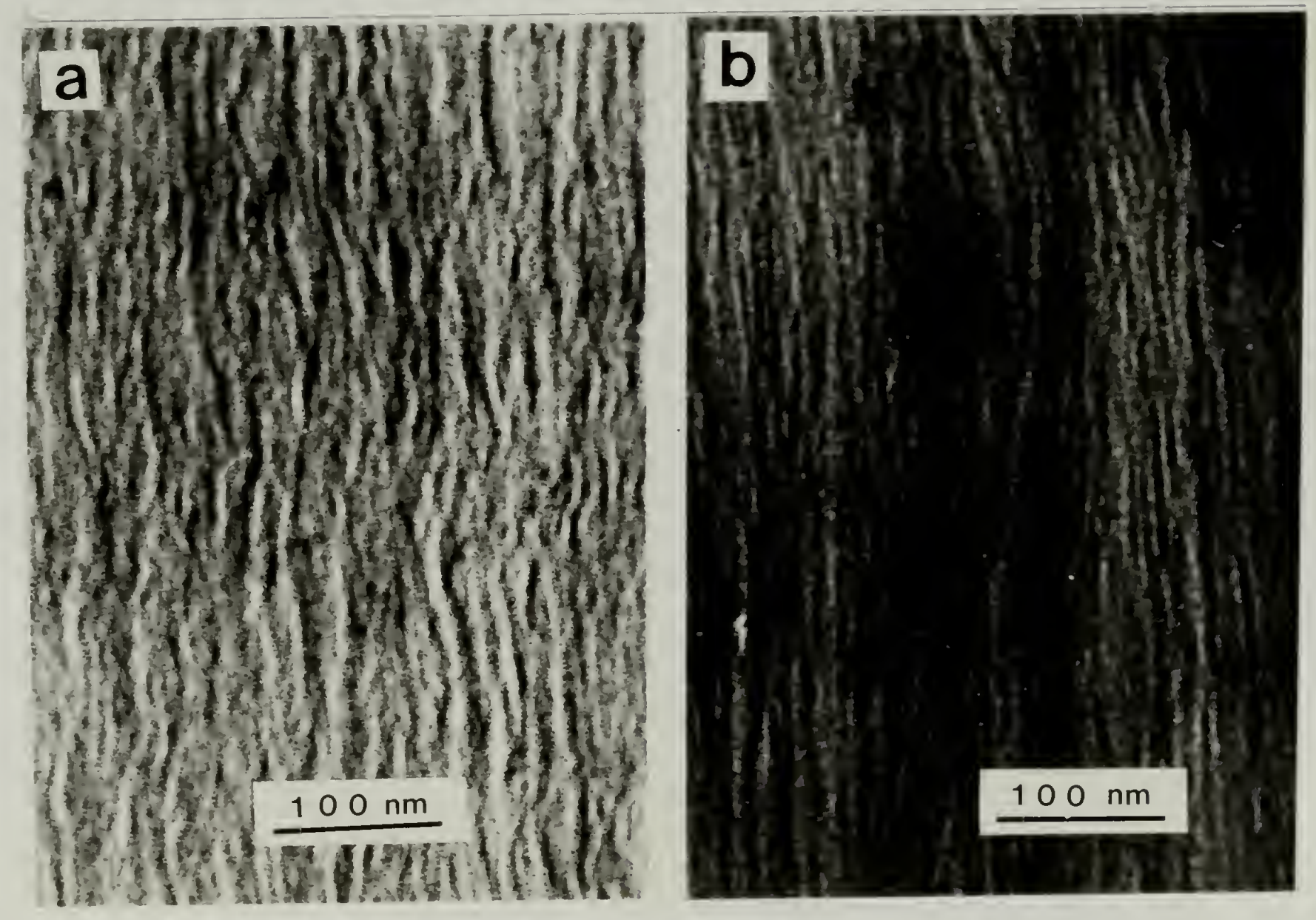

Figure 4.18. Electron micrographs of epoxy-impregnated PBT films: (a) water coagulated (FM2W), (b) acid coagulated (FM2P).

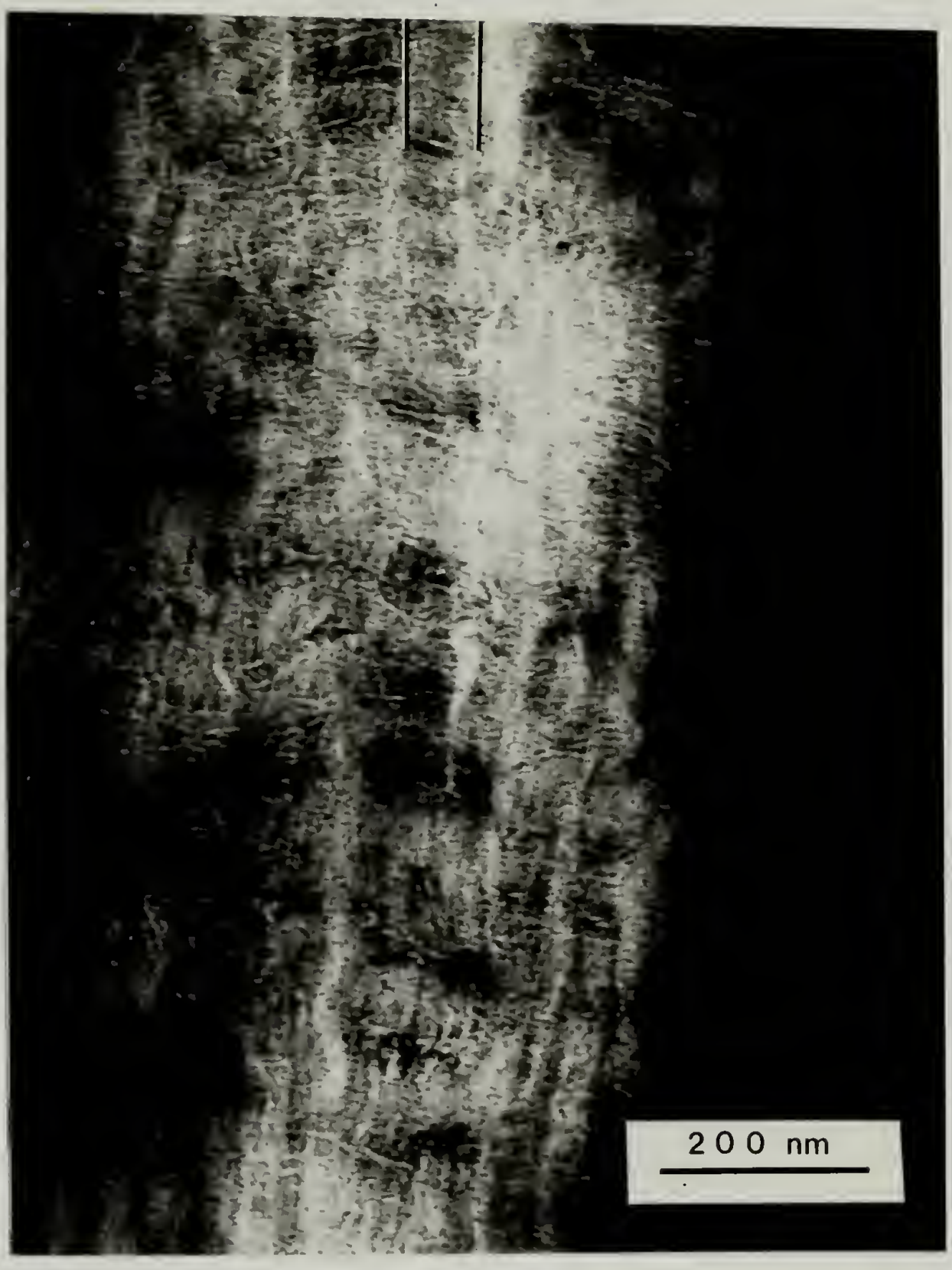

Figure 4.19. Electron micrograph of a banded region which is occasionally observed in the acid-coagulated films (FM2P).

morphology: average width of 71Å, density 1.46 g/cm^3, and volume fraction of 0.18 in an epoxy impregnated film. The microfibrils are shown to have irregularly shaped cross-sections. Visualization of a buckled region indicates that the buckling of the individual microfibrils is the cause of compressive failure. The coagulation process, in which the dimensions of the microfibrillar morphology are set, is crucial to the development of the compressive properties of PBT fibers and films.

A novel crystal-solvate phase is shown to be formed by a slow coagulation process using 85% phosphoric acid as a coagulant. A unique structure is proposed, in which the protonated PBT chains and the oligomeric PPA anion, having an extended conformation, co-crystallize parallel to each other. The crystal solvate phase exhibits a degree of three dimensional order which is absent in PBT fibers and films. Preliminary results indicate that formation of an intermediate crystal-solvate phase during the spinning process has a potential for influencing the microfibrillar morphology.

CHAPTER V

THE STRUCTURE FORMED DURING GELATION OF AN ISOTROPIC PBLG SOLUTION

5.1 Introduction

The ability of dilute isotropic solutions of PBLG to form self-supporting clear gels upon a decrease in temperature has been recognized for the past two decades, as was described in section 1.4. This chapter concerns the morphology of PBLG gels formed from isotropic solutions. Direct imaging by electron microscopy, using techniques suitable for observation of a system which consists mostly of a volatile solvent, is combined with SAXS measurements for evaluation of structural models. The mechanistic aspects of the gelation process will be discussed in Chapter VI.

5.2 A Network Morphology Observed by Electron Microscopy

The TEM image of a carbon/platinum replica of the etched fracture surface of a frozen gel is shown in figure 5.1. A disordered, isotropic network of interconnected microfibrils is observed. The morphology is very irregular. The width of the microfibrils ranges from about 50 to 500Å, and the distance between junction points from several hundred to several thousand Angstroms. The microfibrillar morphology is reminiscent of the structure reported by Tohyama and Miller [60] for a PBLG-DMF gel, although the structure shown in figure 5.1 is less regular with respect to the size and directionality of the microfibrils.

Figure 5.1. The image of a PBLG/benzyl alcohol gel revealed by a freeze-fracture replication technique.

A network structure can also be seen in the images of the rapidly frozen, gelled thin films, observed directly using a cold stage. This network, shown in figure 5.2, is on a larger length scale (order 1μm) and has a very different appearance than the microfibrillar network shown in figure 5.1. These images require a careful interpretation due to the unique method by which the gel was formed. As described in section 2.2.3, gelation was induced by an increase in PBLG concentration due to solvent evaporation from a thin film of a dilute solution supported on a copper grid. Figure 5.2a represents the typical morphology observed in a sample prepared in this manner. Figure 5.2b is the morphology observed when a gel formed in a much thicker film is rapidly frozen, with the solvent subsequently sublimed in the electron microscope. The structure observed when the solvent is allowed to completely evaporate from the solution deposited on the grid, is shown in figure 5.2c.

The image in figure 5.2a exhibits a "foam-like" morphology with open cells which are spanned by solid regions. Since the only components in the observed system are the polymer and solvent (there is no support film, etc.) the solid region is the frozen gel and the open cells are voids from which the solvent has evaporated. This image is therefore a manifestation of the solvent evaporation process, which has been interrupted by the rapid freezing. It is interpreted as reflecting inhomogeneities in the polymer concentration within the gel, as the solvent is expected to evaporate more readily from regions of the gel having negligible polymer concentration. The observation of a similar

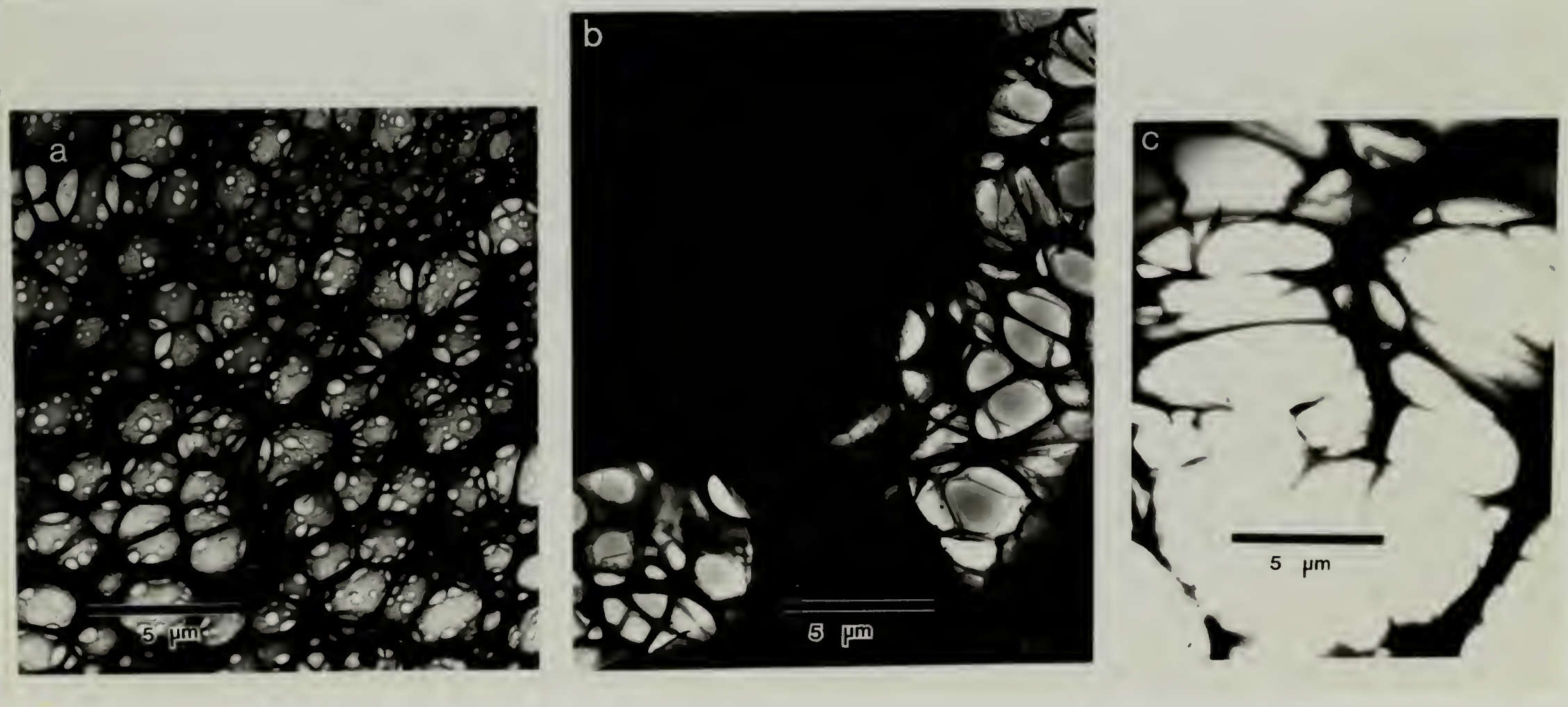

Figure 5.2. A direct image of a PBLG gel obtained by cold-stage electron microscopy: (a) a rapidly frozen thin film, (b) a rapidly frozen thicker film, after partial sublimation of the solvent in the microscope. (c) a thin film completely dried at room temperature.

structure in the regions of a thicker specimen which were exposed by sublimation of the solvent, as shown in figure 5.2b, indicate that the inhomogeneities are not merely an artifact of the thin film preparation. In some regions where the solvent has been completely sublimed, shown in figure 5.2b, thin microfibrils, the width of which is on the order of 100Å, may be observed. The salient feature of figure 5.1a is the apparent self similarity of the structure: the observation of "cells within cells" ranging in size from about 500Å to over 1μm.

On the basis of the preliminary electron-microscopical observations a tentative model may be formulated for the structure of the isotropic PBLG/benzyl alcohol gel. This model suggests that the gel is composed of clusters of microfibrils which are distributed inhomogeneously throughout space. It thus answers some of the questions posed at the end of section 1.4. The local ordering of the PBLG chains is postulated to be highly correlated in the form of microfibrils composed of parallel-packed chains. This is in agreement with the microfibrillar network propoed by Tohyama and Miller [60]. In addition, the proposed model suggests the presence of larger scale inhomogeneities: regions of increasing length scale up to several microns in which the polymer concentration is negligible, which are interspersed within the regions in which the microfibrillar clusters exist. The presence of large scale homogeneities is consistent with the observations of Russo et al. [61] on PBLG-toluene gels discussed in section 1.4.2. It should be emphasized that the difference in polymer concentration between these regions need not be significantly large. For the 1% PBLG gel studied here, the

polymer concentration within the regions of microfibrillar clusters will be only a few percent, whereas it would be essentially zero in the other regions. This difference is enough to have an effect on the evaporation or sublimation of the solvent.

5.3 SAXS Evidence for a Fractal Structure

In accordance with the principle guiding this thesis, SAXS measurements are used to substantiate structural models based on electron microscopical observations. The dotted line in figure 5.3 is the experimentally measured SAXS pattern from a 1% PBLG/benzyl alcohol gel, after subtraction of the scattering from the pure solvent. The simulated scattering pattern calculated for three structural models is compared with the experimental results. These models are: (a) a dilute suspension of long thin fibrils; (b) a random two phase structure; (c) a self similar, fractal structure. Since the overall structure of the gel is isotropic, and a slit-collimated incident beam is used, the scattering patterns calculated theoretically for the case of point collimation, can be corrected for the slit geometry, assuming a slit of infinite length [72,84]:

$$\tilde{I}(S) = \int_{-\infty}^{\infty} I(\sqrt{s^2+m^2})\,dm \qquad (5.1)$$

where $I(S)$ and $\tilde{I}(S)$ are the scattered intensities from a point and slit-collimated incident beam, respectively.

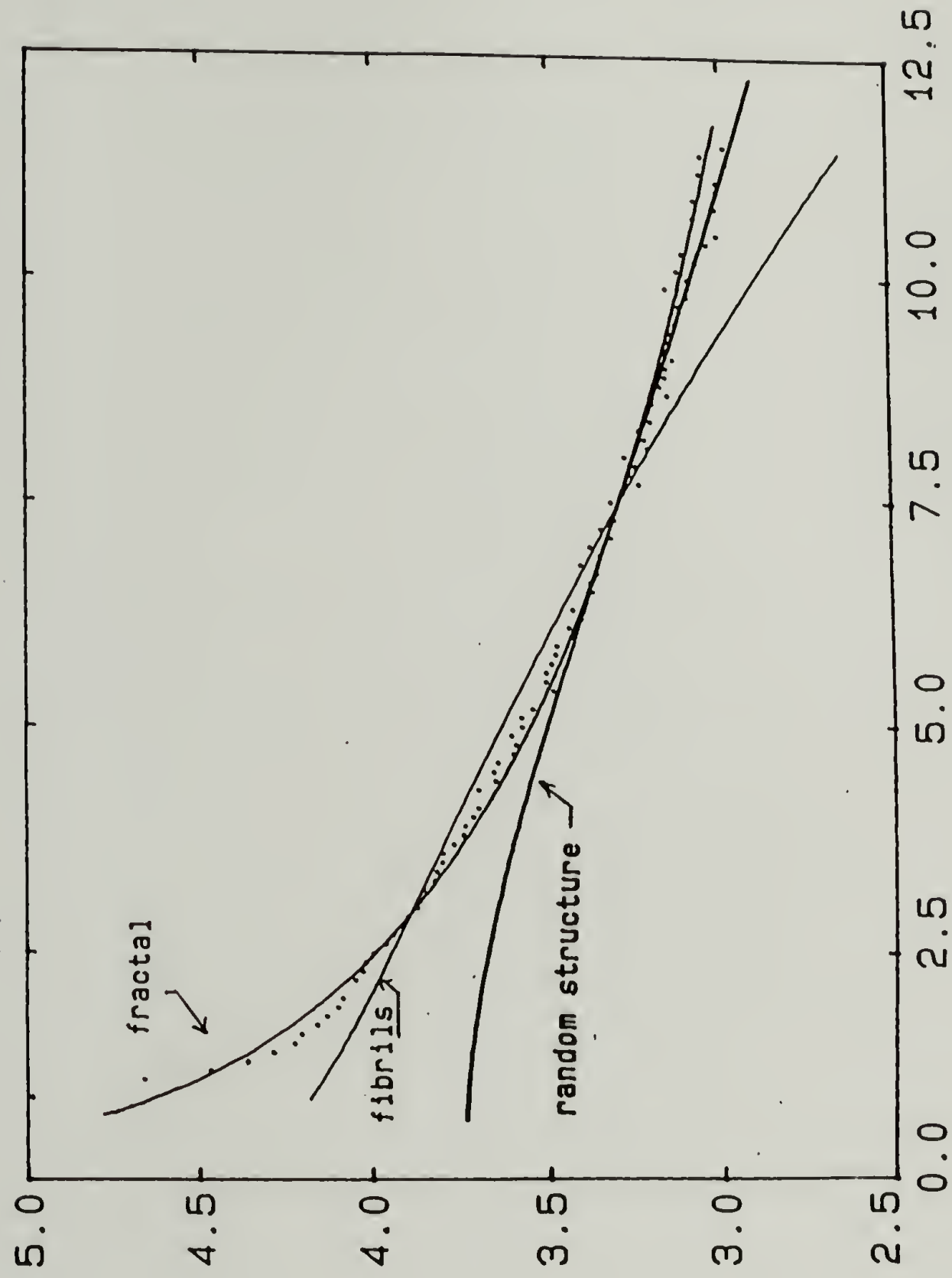

Figure 5.3. The SAXS pattern from a PBLG/benzyl alcohol gel. A comparison of the experimental data with simulated patterns using three structural models.

The intensity of radiation scattered from a dilute assembly of long, thin rods is as follows [72]:

$$I(S) \sim \frac{L}{S} I_c(S) \tag{5.2}$$

where L is the length of the rod and $I_c(S)$ is a function of the cross-section of the rod. If the width of the rod (D) is small, such that $DS<<1$, the usual Guinier approximation can be used [83], so that:

$$I(S) \sim \frac{L}{S} \exp(-2\pi^2 S^2 R_c^2) \tag{5.3}$$

Where R_c is the radius of gyration of the cross-section, which for a disc of radius R_o is

$$R_c = R_o/\sqrt{2} \tag{5.4}$$

The slit smeared scattering pattern for the isotropic assembly of isolated long, thin microfibrils is obtained by substituting equation (5.3) in (5.1), which yields [99]:

$$\tilde{I}(S) \sim K_o(\pi^2 R_c^2 S^2)\exp(-\pi^2 R_c^2 S^2) \tag{5.5}$$

where K_o is the modified Bessel function of zero order.

The scattering pattern from a random two phase structure, i.e., a structure which is described by an exponentially decreasing correlation function (see section 3.3) is given by Debye et al. [80]:

$$I(S) \sim (1+4\pi^2 \ell_c^2 S^2)^{-2} \tag{5.6}$$

where ℓ_c is the correlation length. The slit-smeared scattering pattern obtained using equation 5.1 is [81]:

$$\tilde{I}(S) \sim (1+4\pi^2 \ell_c^2 S^2)^{-3/2} \tag{5.7}$$

which is the same functional form as equation 3.37 for fully oriented systems. The structures are, of course, different.

A fractal structure is self similar in the sense that when observed at different length scales it has the same appearance [100]. Stated mathematically, upon a change of length scale by a factor λ, the correlation function changes only by a multiplication factor:

$$\gamma(\lambda r) = \lambda^{-A}\gamma(r) \tag{5.8}$$

where A is an arbitrary constant. A correlation function which satisfies (5.8), i.e., has no implicit length scale, is a power law function:

$$\gamma(r) \sim r^{-A} \tag{5.9}$$

As the scattering pattern is the Fourier transform of the correlation function (equation 3.1), the scattering pattern from a fractal structure is given by:

$$I(S) \sim r^{-A+d} \tag{5.10}$$

where d is the spatial dimensionality.

The number of particles in a sphere of radius R is proportional to the volume integral of the correlation function [84]:

$$N(R) \sim \int_0^R \gamma(r)\, d\underset{\sim}{r}^d \sim R^{d-A} \tag{5.11}$$

A fractal structure is characterized by its "fractal dimension" D_f, defined as [100]:

$$N(R) \sim R^{D_f} \tag{5.12}$$

The scattering pattern is therefore given by:

$$I(S) \sim S^{-D_f} \tag{5.13}$$

and the slit-smeared scattering pattern by:

$$\tilde{I}(S) \sim S^{-D_f+1} \tag{5.14}$$

The best fit of the experimental data using the three models is shown in figure 5.3. The simulated patterns were obtained using the following parameters:

(a) Fibrils: $R_c = 28\text{Å}$, for which the fibril diameter is 80Å

(b) Random structure: correlation length $\ell_c = 21\text{Å}$

(c) Fractal: $D_f = 2.5$

The fibril model fits the data poorly. It does not predict even the correct curvature of the scattering pattern. The random structure model can always be made to fit the large angle part of the pattern, but fails at smaller angles, where the large scale correlations are important. The fractal model appears to fit the experimental data in the measured range of scattering angles, which correspond to dimensions between 100Å to 1000Å. In this range of length scales, the SAXS experiment probes the correlations within the region of the microfibrillar clusters. The results suggest that the microfibrillar clusters are self-similar, with a fractal dimension of 2.5.

The structural model proposed for the PBLG/benzyl alcohol gel formed from an isotropic solution, can be described as clusters of microfibrils having a fractal structure, characterized by a fractal

dimension of 2.5, and which are aggregated and interconnected to form an overall structure in which there are inhomogeneities of several length scales ranging to over 1 μm.

The implications of the structural model to the gelation mechanism will be discussed in Chapter VI. It will be noted here that this model has several features in common with the structure obtained by simulations of a "cluster-cluster aggregation" process [101,102]. An example of the result of one such simulation [102] is shown in figure 5.4.

5.4 Conclusions

The morphology of a PBLG gel formed from a dilute isotropic solution in benzyl alcohol is shown to consist of disordered clusters of microfibrils, the width of which is on the order of 100Å. SAXS measurements indicate that on the length scale of 10^2 to 10^3Å the structure can be described as a self similar fractal of dimension 2.5. Direct visualization by cold-stage electron microscopy of the gel structure has been achieved for PBLG gels in benzene, formed in a thin film by solvent evaporation from a dilute solution. The occurrence of large scale inhomogeneities, which appear to have a self-similar structure on the length scale of 0.1-5 μm, is indicated.

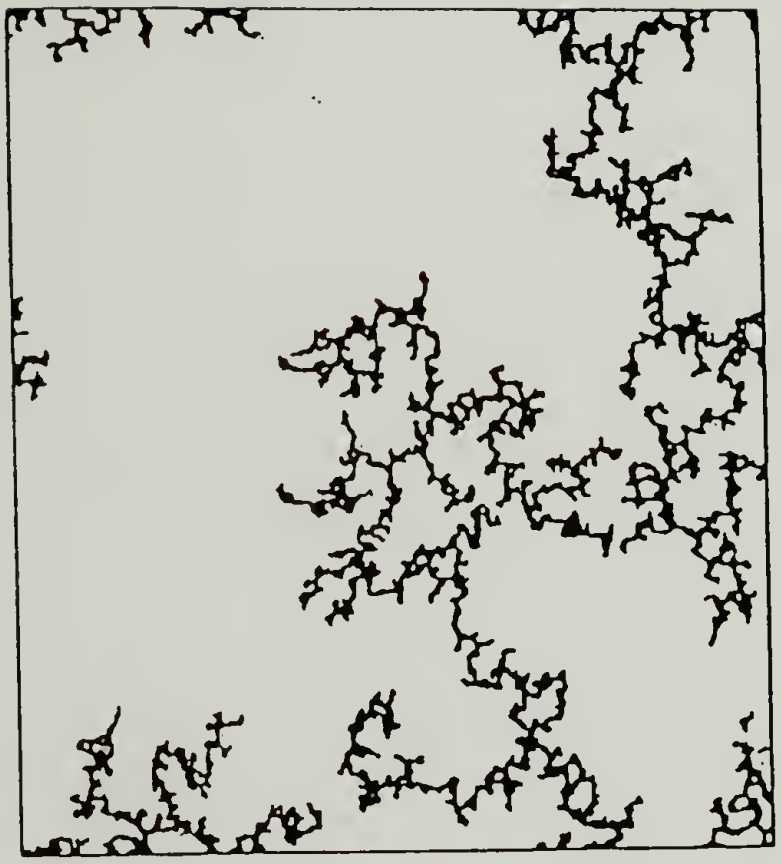

Figure 5.4. The simulated morphology obtained by a "cluster-cluster aggregation" process in two dimensions for a particle volume fraction of 6.25% (from ref. [109]).

CHAPTER VI

THE RELATION BETWEEN PHASE EQUILIBRIA, KINETICS, AND MORPHOLOGY

6.1 Kinetic Mechanisms

Phase separation in a binary mixture is predicted to occur whenever there are more than one minima in the free energy of the mixture as a function of concentration [103]. This is shown schematically in figure 6.1a. The concentrations of the phases coexisting at equilibrium are given by the common tangent (the "Maxwell construction"). These points mark the binodal curve in the temperature-composition phase diagram (figure 6.1b). The inflection points in the free energy curve define the points of the spinodal in the phase diagram. This is the boundary between the areas of metastable and unstable mixtures. In the metastable region, between the binodal and the spinodal, the free energy curve is concave. The mixture is stable towards small concentration fluctuations, as they will render the free energy higher than that of the homogeneous mixture. It is metastable towards large fluctuations, such as nuclei, and will separate to two phases whose compositions are given by the binodal. Within the spinodal, the free energy curve is convex, the mixture is unstable even to small composition fluctuations, as the free energy of an infinitisimally separated mixture is lower than that of the homogeneous mixture. Different mechanisms are considered for the phase separation process, depending on whether it takes place in the metastable or unstable region of the phase diagram.

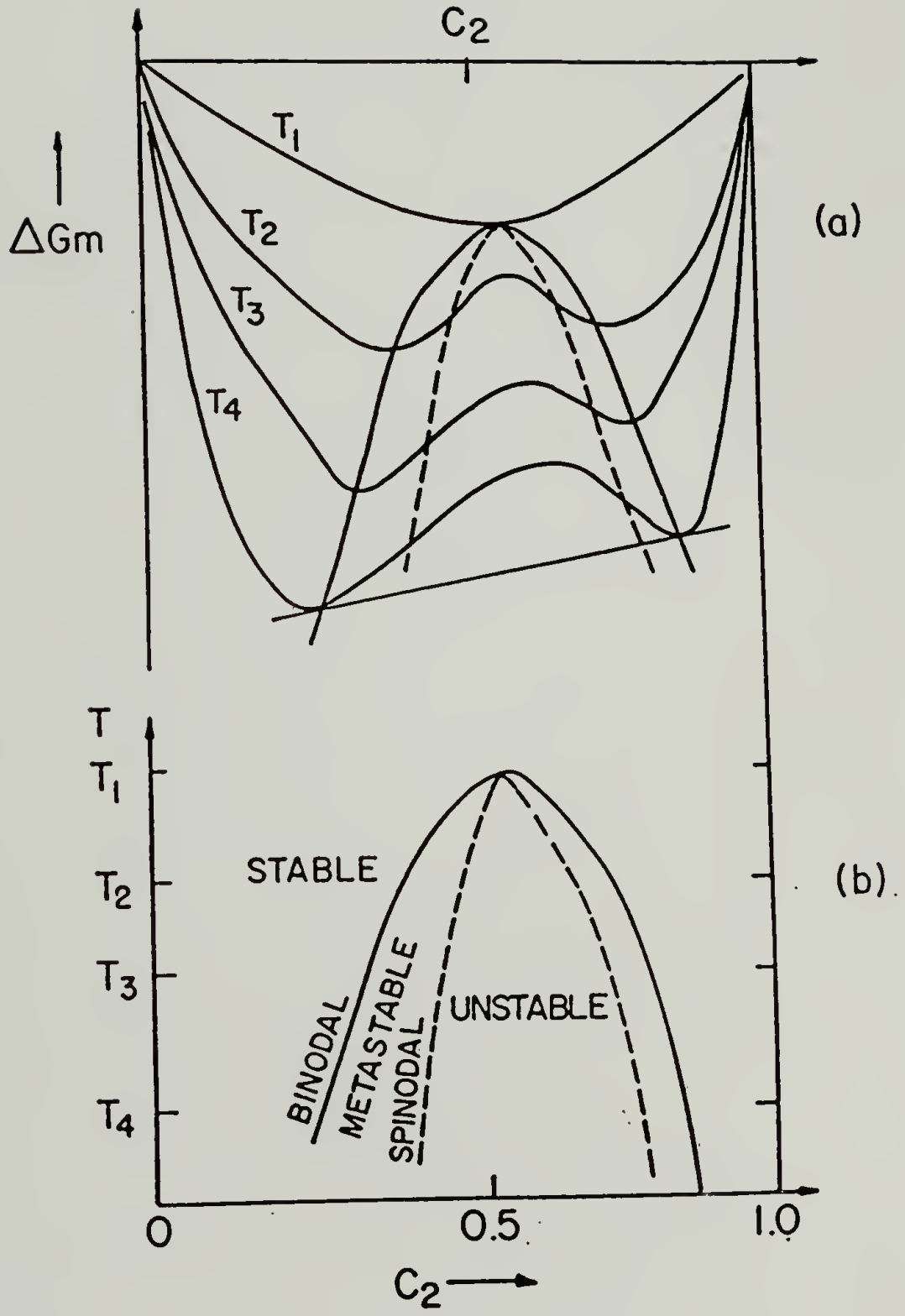

Figure 6.1. Thermodynamics of a binary mixture: (a) a schematic representation of the free energy of mixing, (b) the temperature–composition phase diagram.

Within the spinodal, where the mixture is unstable towards small concentration fluctuations, phase separation proceeds by continuous growth of the amplitude of these fluctuations, brought about by an "uphill" diffusion process. The kinetics of this mechanism, called "spinodal decomposition," where first treated by Cahn and Hilliard [104], by introducing the dependence of the free energy of the mixture on the concentration gradient:

$$G = \int_V [G_o + K(\nabla c)^2] \, dv \tag{6.1}$$

where G_o is the free energy density of the homogeneous mixture, c is a concentration variable, and K is a constant. The Cahn-Hilliard model [104] predicts that a fluctuation of a specific wavelength λ_n given by:

$$\lambda_m = 4\pi \left[-\left(\frac{\partial^2 G}{\partial c^2} \right)_{c_o} / K \right]^{-1/2} \tag{6.2}$$

will have a maximum growth rate. Spinodal decomposition is therefore characterized by a continuous change in the concentration of the separating phases, the length scale of which remains constant, at least initially.

In the metastable region, formation of a large concentration fluctuation (nucleation) results in a depletion zone surrounding the separated phase. Growth ensues by "downhill" diffusion of the separating component towards the nucleated phase. The "nucleation and growth" process is thus characterized by a continuous increase in the size of the separating phase, while its concentration remains constant. The rate of phase separation is governed by the rates of both nucleation and

diffusion. In the case where nucleation is the rate-limiting step, the kinetics as well as the morphology are controlled by the nucleation rate. It can be approximated as [105]:

$$\frac{dN^*}{dt} \sim \exp[-\alpha T_m^2/kT(T_m-T)^2(\Delta H_f)^2] \qquad (6.3)$$

where N* is the number of nucleation sites, T_m is the melting (or dissolution) temperature and ΔH_f the enthalpy of the transition. α is a constant depending on the surface energy of the nucleus, and is different for homogeneous or heterogeneous nucleation.

Diffusion-limited aggregation (DLA) is at the other extreme of the spectrum of nucleation and growth processes. Many variants of DLA have been proposed (see, for example [106]), mostly by means of their computer simulation. Only two will be discussed: particle-cluster aggregation (PA) and cluster-cluster aggregation (CA).

In the PA model, first suggested by Witten and Sander [107], particles are allowed to diffuse, successively towards a nucleation center by a random walk from a distant point. Whenever a diffusing particle comes into contact with another particle which is part of the cluster emerging from the nucleation center, it sticks to it. The cluster grown by such successive cycles has unique features: it is extremely tenuous and does not completely fill a finite fraction of space. Furthermore, it is devoid of a characteristic length scale, yet exhibits self similarity in its structure over a range of length scales. It can therefore be described as a fractal object, the nature of which has been discussed in section 5.2. The relation between the fractal dimension of the cluster, D_f, and the dimension of space in which the process occurs, d, is given

by Muthukumar [108] as:

$$D_f = (d^2+1)/(d+1) \tag{6.4}$$

This expression is in good agreement with computer simulations for d=2,3,4 [109]. A process as described above (PA) can be considered as a DLA process under conditions of a low nucleation density.

A DLA process occurring in a situation having a high nucleation density, whereby the restrictions on the critical size of a nucleus are negligible, is simulated by the cluster-cluster aggregation (CA) model. In this model the particles in an initially homogeneous, dilute system, are allowed to move independently of each other in a random walk. Clusters are formed when the particles come into contact with each other, forming dimers, trimers, etc. The clusters continue to diffuse, and again stick to other clusters (or particles) upon contact. This process continues until finally all the particles belong to a single, space-spanning, cluster. The cluster described by this process is also a self-similar fractal object. Its fractal dimensionality is lower than in the PA case ($D_f \simeq 1.8$ for d=3) [110]. This is due to the fact that the clusters cannot easily interpenetrate, which results in much more open space between regions of clustered particles. Although the CA process is a result of microscopic nucleation and growth events, it has several features in common with spinodal decomposition when viewed on a larger scale: the apparently uniform transformation throughout space, with a continuously varying average local concentration on a coarse-grained scale.

The foregoing discussion described the influence exerted by the kinetics of the transition on the morphology of the separated phases. It can be summarized as follows: near equilibrium, the morphology is governed by the nucleation events. Characteristic length scales are determined by the density of primary nucleation sites, and by details of the secondary nucleation (including possible instabilities which result in unique patterns). Farther from equilibrium, a regime of disorderly growth, devoid of a characteristic length scale, may occur. Diffusion controlled processes may result in scale-invariant fractal structures. Even farther from equilibrium, phase separation under conditions of instability towards small-scale fluctuations (e.g., spinoal decomposition) may result in a structure having characteristic dimensions dictated by the kinetics of the separation process. The emergence of ordered structures under conditions far from equilibrium has been extensively investigated by Prigogine and co-workers [111].

In the proceeding sections, the relevance of the different mechanisms discussed above to phase separation in solutions of rigid polymers, will be evaluated.

6.2 Coagulation of PBT Solutions as a Nucleation and Growth Process

The phase transition during slow coagulation of an isotropic PBT solution by atmospheric moisture, as described in section 1.3.2, occurs under conditions close to equilibrium. Nucleation and growth of spherulites can be observed directly by optical microscopy [37]. The

coagulation process during the spinning of PBT fibers and films, which is induced by immersion in a non-solvent, occurs under conditions which are farther from equilibrium. In section 4.2, the structure formed by this process was shown to be a network of oriented microfibrils, the width of which is on the order of 100Å. The question posed is: by what mechanism the oriented nematic solution is transformed into the microfibrillar network?

The difference in the morphology which is expected to emerge in a monodomain nematic solution, as a result of the mechanisms of spinodal decomposition and nucleation and growth, can be addressed with reference to figure 6.2. Due to the inherent rigidity and relatively high molecular weight of the PBT molecules, polymer and solvent mobility is expected to be anisotropic, being much larger in the orientation direction than perpendicular to it. For simplification, the mobility is assumed to be one dimensional in the orientation direction.

A schematic representation of the Cahn-Hilliard model of spinodal decomposition [104], as applied to oriented rods with one dimensional mobility, is compared to one dimensional nucleation and growth in figure 6.2. In the case of spinodal decomposition, a concentration fluctuation of a specific wavelength will have a maximum rate of growth, as discussed in section 6.1. Since the mobility is assumed to be one dimensional, only concentration fluctuations in the direction of molecular orientation are considered. Growth of such a fluctuation leads to regions of high concentration of rods, perpendicular to the orientation direction, with depletion zones between them, as shown in figure 6.2a.

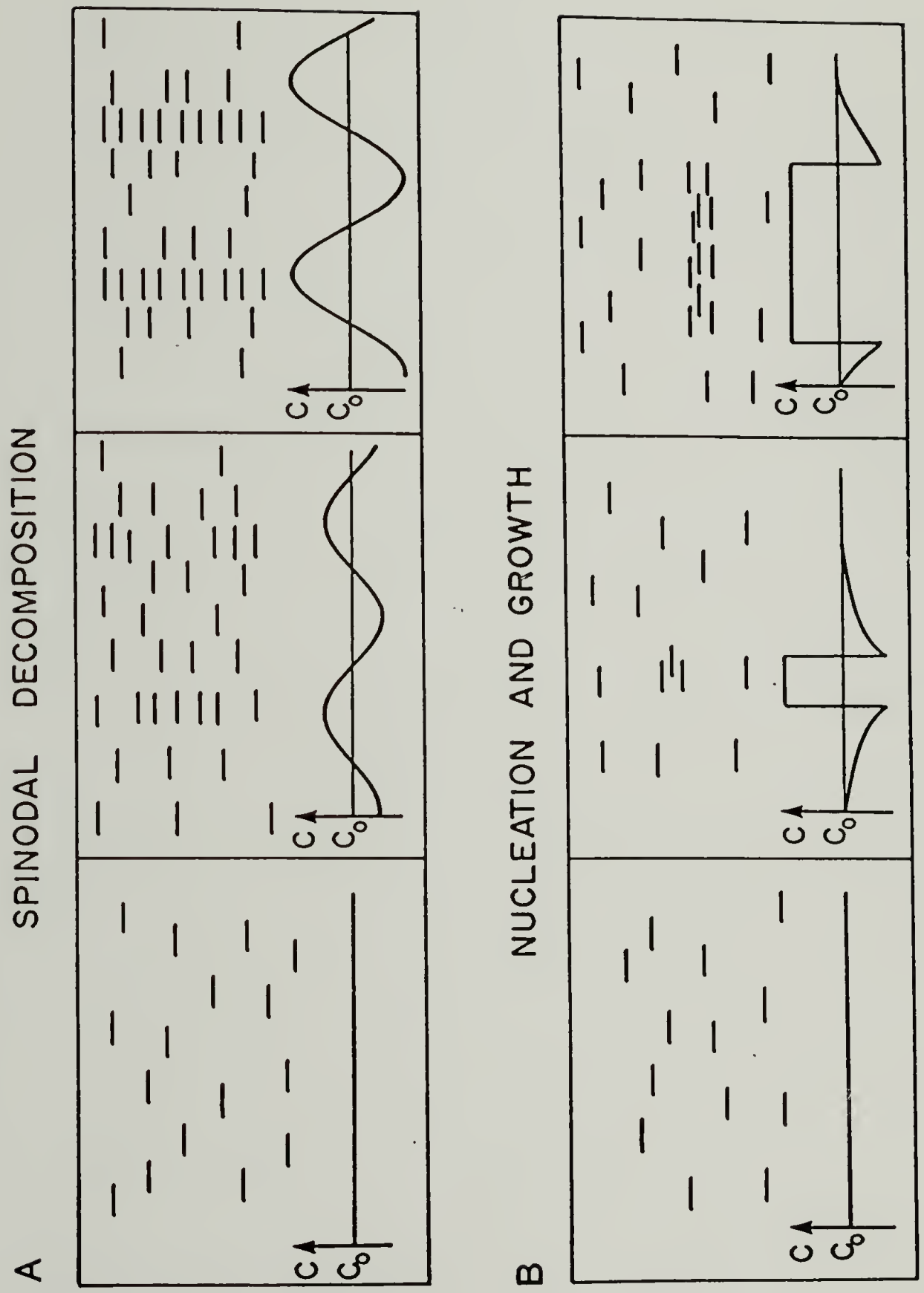

Figure 6.2. A schematic representation of phase separation in a monodomain nematic solution, assuming essentially one-dimensional mobility: (a) spinodal decomposition, (b) nucleation and growth.

The extent of the polymer-rich regions perpendicular to the orientation direction, may be dictated by the correlation length of the fluctuations in that direction. Crystallization of the polymer in the regions of high concentration may result in a lamellar morphology. In general, an "uphill diffusion" of oriented rods in the direction of their alignment will result in discontinuities of the polymer-rich phase along the chain axis direction. This is incompatible with formation of long, continuous microfibrils.

On the other hand, a predominantly one dimensional nucleation and growth process can readily result in formation of a fibrillar morphology, as shown in figure 6.2b. In this case, it is conceivable that the width of the microfibrils is controlled by the density of nuclei. Deviations in the molecular orientation may account for the interconnectivity of the microfibrils. It is therefore proposed the phase transition during coagulation of the oriented PBT solution in the spinning process occurs by a nucleation and growth mechanism.

The coagulation process can now be considered in perspective of a ternary polymer-solvent-nonsolvent phase diagram. A schematic ternary phase diagram, at constant temperature, is shown in figure 6.3. The boundaries of the isotropic and the narrow biphasic (isotropic-nematic) regions are based on an extension of Flory's theory [3] to a polymer-solvent-nonsolvent system, due to Russo and Miller [48]. These boundaries were calculated for a polymer of axial ratio x=100, and the following interaction parameters: $\chi_{P-S}=\chi_{S-NS}=0$; $\chi_{P-NS}=1.0$. They are in qualitative agreement with the phase diagram of the PBLG-DMF-water

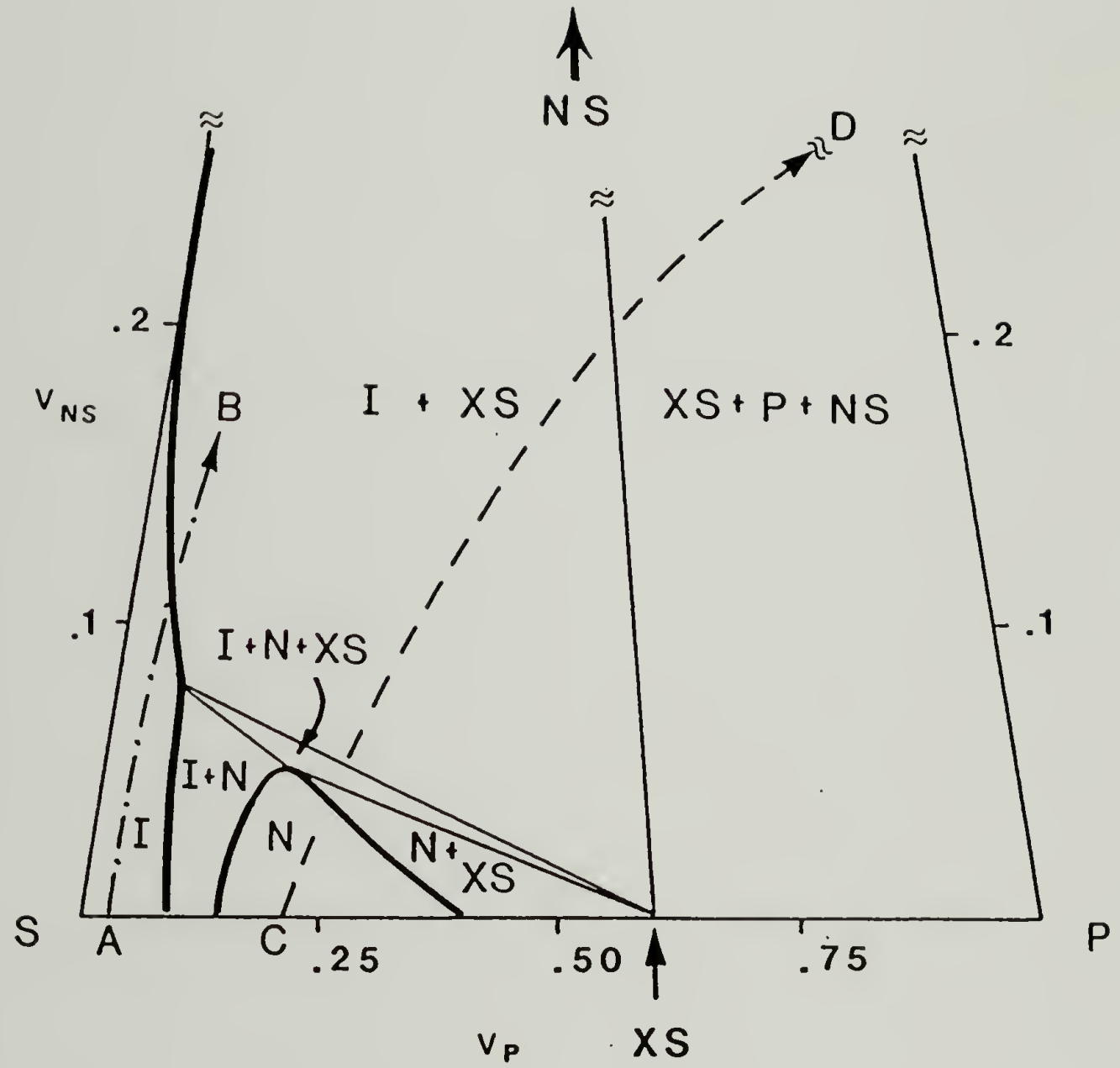

Figure 6.3. A schematic representation of a ternary system composed of a rigid polymer, a solvent and a nonsolvent, at constant temperature.
I - isotropic solution, N - nematic solution, P - crystalline polymer, S - Solvent, NS - nonsolvent, XS - crystal-solvate, v - volume fraction.

system determined by Nakajima et al. [112]. Other boundaries of the biphasic regions are set schematically, in accordance with the Gibbs phase rule. For purpose of clarity only one crystal solvate phase is considered. It is assumed to have a distinct polymer-solvent composition with total exclusion of nonsolvent, and therefore appears as a single point on the polymer-solvent axis. In reality, these constraints may be somewhat relaxed.

Transition to a solid phase can occur either in a region of the phase diagram which is at equilibrium with a crystal-solvate phase, or within the region that is at equilibrium with the formation of the crystalline polymer. The main difference between these two regimes is in the extent of the undercooling relative to the dissolution temperature of the solid phase. As mentioned in sections 1.3.2 and 4.4, the melting point of the crystal-solvates are much lower than the (hypothetical) melting point of the crystalline polymer. Therefore the degree of undercooling in the region of the phase diagram which is at equilibrium with formation of the crystal solvate is much smaller than in the region which is at equilibrium with formation of the solid polymer. Since the nucleation rate is extremely sensitive to the degree of undercooling, as evident from equation 6.3, the density of nucleation centers in a transition to the crystal-solvate phase is expected to be much smaller than the nucleation density in a transition to the solid polymer.

It is instructive to view the coagulation process as a trajectory in the ternary phase diagram, bearing in mind the approximations

involved with any treatment of a non-equilibrium process by means of an equilibrium phase diagram. The shape of the trajectory depends on the rates of diffusion of coagulant into the solution and solvent away from it. This method has been applied to the coagulation of a cellulose-acelate solution during formation of porous membranes [113].

Slow coagulation of an isotropic solution, induced by absorption of moisture, is represented by the trajectory A-B in figure 6.3. The transformation to the crystal-solvate phase occurs just beyond the phase boundary (point B). The very small undercooling relative to formation of the crystal-solvate phase results in a very low density of nuclei. The growth of lamellae to form a spherulite, described in section 1.3.2, is the outcome of a single initial nucleation event.

In the coagulation stage of the spinning process, immersion of the nematic solution in a non-solvent bath can be represented by trajectory C-D in figure 6.3. The region of the phase diagram which is at equilibrium with formation of crystal solvates (at low undercoolings) is bypassed, and the system is transposed to the region at equilibrium with the crystalline polymer (point D). This can be rationalized as follows: A high flux of coagulant into the solution results from its high concentration in the coagulation bath. Before appreciable nucleation of crystal-solvates can occur, enough coagulant has diffused into the solution to deprotonate the PBT molecules, which are now at a very large undercooling relative to formation of PBT crystals. The formation of a microfibrillar morphology is thus postulated to be an outcome of a nucleation and growth process in a monodomain nematic solution under

conditions of an extremely high nucleation density. Under such conditions a nucleus will generate very few microfibrils, most likely one or two.

The morphologies obtained at the two coagulation conditions discussed above represent two extremes in the width of regions formed of aggregated parallel PBT chains: about 10^{4}Å in the lamellar morphology compared to about 10^{2}Å in the microfibrillar morphology. The controlling factor is postulated to be the nucleation density determined by the degree of undercooling, which is much lower when the crystal-solvate phase is formed. This suggests that the path towards achievement of wider microfibrils in PBT fibers and films lies in the formation of the crystal-solvate phase. The experiments reported in sections 4.4 and 4.5 represent preliminary efforts in this direction. The possibility of forming a crystal-solvate phase by coagulation in phosphoric acid has been demonstrated. Its effect on the microfibrillar morphology is as yet inconclusive, mostly due to uncertainties with regards to the subsequent process by which the crystal solvate phase is converted to PBT crystals.

6.3 Evaluation of Different Mechanisms for Gelation of Isotropic PBLG Solutions

Several mechanisms have been invoked for the gelation of an isotropic PBLG solution upon cooling, as was mentioned in section 1.4. The possible models will be now evaluated in view of the morphological features described in Chapter V. A successful model should predict the

following characteristics: (a) a microfibrillar morphology on the 10^2Å length scale; (b) a self-similar fractal structure in the 10^2-10^3Å range; (c) inhomogeneities on a length scale of 10^4Å.

In the simplest model, gelation is considered a glass transition-cessation of large-scale motion of the dissolved PBLG rods. A glass transition in a solution of rod-like polymers has been predicted by Doi and Kuuzu [57] when the volume fraction of the rods, v_p, satisfies:

$$\frac{1}{x} \lesssim v_p << 1 \qquad (6.5)$$

where x is the axial ratio of the rod. The gel is described as a "log-jam" in which there are no orientational correlations between neighboring chains and no large scale inhomogeneities. Such a glass is a non-equilibrium state, as an equilibrium transition to an ordered (liquid-crystalline) state is predicted for $v_p^* \simeq 1/x$ [1]. This model implies that gelation upon a decrease in temperature is an outcome of an increase in the axial ratio of the dissolved polymer, and formation of a "log-jam." The increased rigidity of the PBLG helix, and hence an increase in its axial ratio, is reflected in the shift of the critical concentration for formation of an ordered solution to lower concentrations, upon a decrease in temperature [5,46,49].

There are several discrepancies between predictions of this model and experimental observations on PBLG gels. The Doi-Kuzuu model predicts that the gel modulus should be very sensitive to the polymer concentration, scaling with the fifth power of the concentration [57]. In practice it was found to be much less sensitive, with a scaling power of

1.3-2.6 for gels in benzyl alcohol [52] and 0.25 for gels in DMF and toluene [50]. The "log jam-glass" model is also inconsistent with the observation of microfibrils on the 100Å scale, or larger inhomogeneities on the 1 μm scale.

If gelation is not a glass transition, then a phase separation process must be involved. Miller et al. [49] proposed a mechanism by which phase separation by a spinodal decomposition process results in a bicontinuous system of interpenetrating dilute isotropic and concentrated ordered phases. Crystallization of the polymer in the concentrated ordered phase results in an interconnected microfibrillar morphology. The dimension of the microfibrils is thus predicted to be determined by the characteristic length scale of the spinodal decomposition process. Inhomogeneities on a larger scale are not predicted. This model will be denoted "spinodal/fibril."

Phase separation by spinodal decomposition into interpenetrating isotropic phases may be considered following the results reported by Russo et al. [61]. As the volume fraction of rods in the concentrated phase increases, a glass transition of the "log-jam" type occurs within that phase, thus frustrating further phase separation. Large scale inhomogeneities, resulting from the spinodal decomposition process, are predicted by this model. In this case, the characteristic length scale of spinodal decomposition is assumed to be about 1 μm, two orders of magnitude larger than in the "spinodal/fibril" model. It is in accord with observation by optical microscopy [61] and light scattering [51,

61]. This model does not predict structural features on the microfibrillar level. It will be denoted the "spinodal/glass" model.

In view of the proposed mechanisms which involve spinodal decomposition, it is of interest to focus attention on the location of the spinodal in the limit of a dilute isotropic solution of rod-like polymers. As mentioned in section 6.1, the location of the spinodal is the limit of metastability towards small concentration fluctuations. It is given by the condition [103]:

$$\frac{d^2\Delta G_m}{dv_p^2} = 0 \qquad (6.6)$$

where for the isotropic solution under consideration ΔG_m is given by equation 1.6 with $\bar{y}=x$. The result obtained in this case is identical to the limit of metastability in a solution of a flexible polymer of the same length [6]:

$$\chi_S = \frac{1}{2}\left[\frac{1}{1-V_p} + \frac{1}{xV_p}\right] \qquad (6.7)$$

where χ_S is the value of the Flory χ-parameter at the spinodal. Wee and Miller [114] established a relationship between temperature and the χ parameter for PBLG solutions in DMF. The value of χ at the gelation temperature of a 1% solution (for x=100) can be estimated as 0.15. Equation 6.7 yields for the same conditions $\chi \simeq 1.0$. This is a significant difference. It suggests that the unstable region may be inaccessible by a reasonable temperature quench from the very dilute solutions which exhibit gelation. However, the equivalence of the criterion for

the limit of metastability in both solutions of rigid, as well as flexible polymers, may indicate the inadequacy of the theory for dilute solutions of rods. The possibility of coupling between fluctuations in concentration and orientation, and its effect on phase separation in isotropic solutions, is beyond the scope of current theories. For an assessment of spinodal decomposition as a possible mechanism for gelation of dilute isotropic solutions, a more specific thermodynamic theory for isotropic solutions of rigid polymers is necessary.

The final mechanism to be considered for gelation of isotropic PBLG solutions is diffusion-limited aggregation (DLA), in particular the cluster-cluster aggregation model (CA) described in section 6.1. The driving force for the transition is not liquid-liquid phase separation, as in the models involving spinodal decomposition, but crystallization of the polymer. Theoretical considerations [7-9] have shown that it is reasonable that a dilute isotropic solution of rigid polymers becomes metastable towards crystallization. The nature of the crystalline phase, whether it is a crystal-solvate or a pure PBLG crystal is not clear. Since the reported diffraction patterns of PBLG-benzyl alcohol gels at higher polymer concentrations [52,53] have been interpreted as indicating a crystal-solvate, it is reasonable to assume that the microfibrils of the dilute PBLG gels are crystal-solvates as well.

The proposed gelation mechanism is envisaged as follows: A dilute isotropic solution is supercooled with respect to formation of the crystal-solvate phase. Isolated molecules aggregate to form clusters which continue to aggregate, as described in section 6.1. On a

molecular scale, polymer and solvent co-crystallize to form microfibrils, which form clusters that can be described as fractal objects. The clustering of clusters results in a space-spanning network having large scale inhomogeneities. The simulated structure formed by a CA process (but not of rods), for a 6% solution in two dimensions, was previously displayed in figure 5.4.

The structural predictions of the gelation models discussed above are summarized in table 6.1. The cluster-aggregation model is attractive as it predicts the formation of microfibrils, as well as larger scale inhomogeneities. It is also consistent with an apparent nucleation-free, continuous process, when observed on the length scale of 1-10 μm as probed by optical microscopy and light scattering.

The value of the fractal dimensionality measured by SAXS was 2.5. It is similar to the dimension predicted by theory [108] and simulations [109] for a particle-cluster model of a DLA process. Simulations of CA processes yield a lower dimensionality [101,102,110] (1.8 in three dimensions [110]). Both theory and simulations do not account for the anisotropy of the diffusing particles. In the case where the diffusing rods "stick" upon contact, without orientational reagrangement, a lower dimensionally (more open structure) is predicted [115]. The discrepancy with regards to the fractal dimensionality is yet to be settled. The role of the crystal solvate phase in allowing a more compact structure due to a weaker interaction between chains (lower enthalpy of crystallization), and hence a lower "sticking probability," is not clear.

Table 6.1. Structural Predictions of Gelation Models

Model	Short Range Orientation Correlations (Fibrils)	Large Scale Inhomogeneities
Log-jam/Glass	No	No
Spinodal/Fibril	Yes	No
Spinodal/Glass	No	Yes
Cluster-Aggregation	Yes	Yes

More experiments, as well as theory and simulations, are needed for a better understanding of the gelation process. It is believed that diffusion limited aggregation, and the cluster-aggregation model, are a good starting point.

CHAPTER VII

CONCLUSIONS AND SUGGESTIONS FOR FUTURE STUDIES

7.1 Summary of the Conclusions

The focus of this thesis is the morphology developed when a phase transition is induced in a solution of a rigid polymer. Two cases have been considered: coagulation of a monodomain nematic solution induced by addition of a non solvent and gelation of an isotropic solution induced by a decrease in temperature. The former case is realized in the spinning process of high performance PBT fibers and films. In the latter case, a solution of a synthetic polypeptide PBLG was used as a model system.

The conclusions with regards to the coagulation of PBT solutions are summarized below:

(1) An interconnected network of oriented microfibrils, having a typical width on the order of 100Å, is observed by electron microscopy. It is identified as the basic structural element of PBT fibers and films. A direct visualization of a buckled region indicates that the width of the microfibrils, which is set in the coagulation process, is the controlling factor for the compressive strength of PBT fibers and films.

(2) The theoretical framework for analysis of SAXS measurements from systems of oriented fibrils using a slit-collimated incident beam is outlined. The scattering pattern reflects the structure in a cross-section plane perpendicular to the orientation direction.

The relations between the measured pattern and the characteristics of the morphology in the cross-section plane are derived.

(3) Using SAXS measurements, the characteristics of the microfibrillar cross-sections are quantitatively determined. The parameters that can be evaluated are: average diameter, density, and volume fraction of the microfibrils.

(4) Formation of a novel crystal-solvate phase in the PBT/PPA system, induced by coagulation in phosphoric acid, is demonstrated. It is formed by co-crystallization of the protonated PBT and the PPA anion. This structure is unique in that it is a complex between a rod-like polymer and an oligomeric solvent. Analysis of the x-ray diffraction pattern indicates an orthorhombic unit cell [a=15.9Å; b=20.6Å; c=36.9Å], in which the PPA anion has an extended conformation, parallel to the PBT chain, with a repeat length of 4.6Å.

(5) The proposed mechanism for structure formation, in the monodomain nematic solution, is nucleation and growth, whereby a high nucleation density and essentially one-dimensional growth result in a microfibrillar morphology. This model suggests that the width of the microfibrils is controlled by the nucleation rate which is largely dependent on the degree of undercooling. Preliminary results indicate that formation of an intermediate crystal-solvate phase during the spinning process has a potential for influencing the microfibrillar morphology.

The conclusions concerning gelation of the isotropic PBLG solutions are summarized below. The structure of a PBLG gel, which is formed from an isotropic solution in benzyl alcohol, was studied by SAXS and electron microscopy. Much effort was directed towards direct visualization of the gel structure by electron microscopy using cryogenic techniques. The following characteristics of the PBLG gel are obtained by these studies:

(a) A disordered cluster of microfibrils is observed, the width of which is on the order of 100Å.

(b) SAXS measurements indicate that on the length scale of 10^2-10^3Å the structure can be described as a self-similar fractal structure with a dimensionality of 2.5.

(c) Observations by cold-stage electron microscopy indicate the occurrence of large scale inhomogeneities, on the length scale of over 1 μm. These inhomogeneous also have an apparent self-similar structure in the range of 0.1-5 μm.

It is proposed that gelation occurs by a diffusion limited aggregation process, which is driven by crystallization of the polymer (possibly to a crystal-solvate phase), and is controlled by diffusion.

It has been an objective of this thesis to describe a relation between the initial state of a solution of a rigid polymer, the kinetic pathway of the phase transition and the ensuing morphology. The conclusions drawn from this study, concerning isotropic and monodomain nematic solutions, as well as some inferences from previous studies, are

summarized in Table 7.1. It is evident that the understanding of these issues is far from complete. Much is left for future studies.

7.2 Suggestions for Future Studies

7.2.1 The Effect of Coagulation Conditions on the Structure and Properties of PBT Fibers and Films

A major thrust of this thesis has been the characterization and control of the microfibrillar morphology formed during coagulation, in the spinning process of PBT fibers and films. Although the potential for control of the microfibrillar width by formation of an intermediate crystal-solvate phase has been demonstrated, the ultimate goal has not yet been achieved. Further studies are suggested on the following lines:

(1) The use of different coagulants. Phosphoric acid was used in this thesis so as to remain within the P_2O_5/water system. Other coagulation conditions should be investigated, in particular mixtures of water with acids whose pK_a is intermediate between that of phosphoric acid and PPA. Preliminary observations indicate that sulfuric acid is a good candidate.

(2) Investigation of the transition from the crystal-solvate phase to the solid PBT phase. So far, this transition was induced by immersion in water. A more controlled transition should be investigated. One possibility is a gradual increase in the water content of the coagulation bath from 15% to 100%. Alternatively, heat treatment of the crystal-solvate phase above its melting point will result in an irreversible transition to solid PBT due to hydrolysis

Table 7.1. Conjectured Relationship Between the Mechanism of Phase Transition in a Rigid-Polymer Solution and the Morphology of the Solid State

MECHANISM	Initial State of Solution: ISOTROPIC	NEMATIC polydomain	NEMATIC monodomain
A. NUCLEATION AND GROWTH			
1. Nucleation controlled			
a) slow, few nuclei	spherulites/ lamellae	spherulites/ lamellae	stacked lamellae/ shish-kebobs
b) rapid, many nuclei	fibrillar mat	fibrillar	oriented fibrils
2. Diffusion Limited	fractal ?	?	?
B. SPINODAL DECOMPOSITION	?	?	lamellar
C. GLASS TRANSITION	"log-jam"	?	?

of the PPA. The morphology formed by these processes can be studied using the methods employed in this thesis.

(3) Finally, the effect of the coagulation conditions on the mechanical properties should be investigated, in order to test the conjectured correlation between the width of the microfibrils and the compressive properties. Methods for the measurement of the compressive strength have been discussed by DeTeresa [33].

7.2.2 Characterization of the Crystal-Solvate Phase

The structural characterization of the crystal-solvate phase reported in this thesis are only the first step. There are several unresolved issues: the exact composition (stoichiometry, presence of water or H_3O^+), the state of protonation and details of the conformation of PPA. The possibility of forming different phases of varying compositions should not be overlooked. These questions may be answered by means of a more complete crystal-structure analysis, for which larger and more perfect crystals are necessary. The use of PBT having lower molecular weight may be helpful. Structural analysis by x-ray crystallography of co-crystals of PPA with low molecular weight model compounds (analogs of PBT) may be instructive.

In addition to analysis of its crystal structure, it is of interest to study the microstructure of the oriented PBT/PPA crystal solvate phase on a larger scale. SAXS measurements on the phosphoric-acid coagulated system, as well as optical microscopy, can be pursued.

The nature of the high temperature transitions is another point of interest. X-ray diffraction measurements at elevated temperatures, as

well as optical microscopy using a hot stage, may reveal more information regarding the sharp transition at 250°C.

7.2.3 Phase Transitions in PBLG Solutions

The observations reported in this thesis represent only preliminary studies on the nature of PBLG gels. Further refinement of the cold stage technique which would allow observation of the structure on a finer scale are necessary. The apparently fractal structure of the gel should be further investigated. The self-similarity of the structure should be tested using other scattering techniques such as small-angle neutron scattering (SANS) and small-angle light scattering. This is necessary to characterize the structure in the intermediate length scales, between that of the microfibrils and of the large scale inhomogeneities. In particular SANS measurements of gels formed in deuterated solvents (e.g., d_6-benzene) should be useful due to enhanced contrast, as compared with SAXS. The fractal dimensionality should thus be tested as a function of concentration, molecular weight and temperature of gelation.

The morphology of gels formed from ordered solutions has not been treated in this thesis. PBLG forms a cholesteric phase, the pitch of which depends both on concentration and temperature. A mixture of the D- and L- enantiomers yields a nematic phase. The ordered phases exhibit complex textures due to defects (disclinations) which depend on surface effects and the thermal history of the sample. Little is known about the structure of gels formed from ordered phases. The freeze-

fracture-replication technique seems to be a possible starting point for further studies.

The nature of the correlation between neighboring chains needs more clarification. Are the microfibrils composed of parallel helices with a crystal-like packing? If so, is it the same crystal packing as in a solid PBLG fiber, or a co-crystal with solvent molecules? Wide-angle neutron scattering using a deuterated solvent is likely to be sensitive to formation of PBLG-solvent co-crystals.

A monodomain nematic solution of PBLG can be obtained by orientation with electric or magnetic fields [116]. This allows the investigation of the phase transition in a monodomain nematic state induced by a decrease in temperature. It is of interest to test the predictions of the "one dimensional" model for spinodal decomposition and nucleation and growth, discussed in Chapter VI.

7.2.4 Theory and Simulation

It has been pointed out in Chapter VI that a suitable thermodynamic theory for an isotropic solution of a rigid polymer is lacking. This is necessary, for example, in order to evaluate the limit of metastability (the location of the spinodal). The lattice theory of Flory for a solution of a rigid-polymer yields results which are identical to those of the lattice theory for flexible polymers. As the mean-field approach which is the basis of the lattice theories may be inadequate for dilute solutions, other approaches to obtain the free energy of a dilute isotropic solution of a rigid polymer should be explored. As an extension,

such theory may allow the prediction of spinodal decomposition in isotropic solutions of rigid polymers, by taking into account the stability towards both concentration and orientation fluctuations.

A gelation mechanism was proposed in this thesis, which is analogous to the "cluster-cluster" variant of a diffusion-limited aggregation process. Current simulations of such a process are limited to isotropic particles. Simulations of aggregation in an initially isotropic solution of rods, by the rules of the "cluster-aggregation" model, are suggested. Variations of the "sticking probability" to account for orientation correlations would be of interest.

APPENDIX

MOMENTS OF THE ZERO-ORDER BESSEL FUNCTION

In order to calculate $\int_0^\infty x^p J_o(x)\,dx$, define:

$$I_o(\lambda) = \int_0^\infty e^{-\lambda x} J_o(x)\,dx \tag{A.1}$$

then*:

$$I_o(\lambda) = (1+\lambda^2)^{-1/2} \tag{A.2}$$

and:

$$\int_0^\infty x^p J_o(x)\,dx = (-1)^p \left[\frac{d^p I_o(x)}{d\lambda^p}\right]_{\lambda=0} \tag{A.3}$$

Taking derivatives of (A.2) yields:

$$\begin{aligned} &\text{(a)}\quad I_o'(\lambda) = -\lambda(1+\lambda^2)^{-3/2} \\ &\text{(b)}\quad I_o''(\lambda) = -(1-2\lambda^2)(1+\lambda^2)^{-5/2} \\ &\text{(c)}\quad I_0'''(\lambda) = 3\lambda(3-2\lambda^2)(1+\lambda^2)^{-7/2} \end{aligned} \tag{A.4}$$

---

*I.S. Gradshteyn, I.M. Ryzhik, "Tables of Integrals," Academic Press, New York (1983), p. 707.

Substitution of (A.4) in (A.3) yields:

$$\text{(a)} \quad \int_0^\infty x J_o(x)\,dx = 0$$

$$\text{(b)} \quad \int_0^\infty x^2 J_o(x)\,dx = -1 \qquad \text{(A.5)}$$

$$\text{(c)} \quad \int_0^\infty x^3 J_o(x)\,dx = 0$$

REFERENCES

1. L. Onsager, "The Effects of Shapes on the Interaction of Colloidal Particles", Ann. N.Y. Acad. Sci., 57, 627-659 (1949).

2. A. Isihara, "Theory of Anisotropic Colloidal Solutions", J. Chem. Phys., 19, 1142-1147 (1951).

3. P. J. Flory, "Statistical Thermodynamics of Semi-flexible Chain Molecules", Proc. Roy. Soc. (London), A234, 60-73 (1956).

4. P. J. Flory, "Phase Equilibria in Solutions of Rigid Particles", Proc. Roy. Soc. (London), A234, 73-89 (1956).

5. P.J. Flory, "Molecular Theory of Liquid Crystals", Adv. Polym. Sci., 59, 2-36 (1984).

6. P. J. Flory, Principles of Polymer Chemistry, Cornell University Press, Ithaca (1953).

7. W. R. Krigbaum, A. Ciferri, "Depression of the Melting Temperature for Lyotropic Liquid Crystals", J. Polym. Sci., Polym. Lett. Ed., 18, 253-258 (1980).

8. A. Ciferri, W. R. Krigbaum, "Self Assembly of Natural Polymers via Liquid Crystalline Phases", Mol. Cryst. Liq. Cryst., 69, 273-280 (1981).

9. C. Balbi, E. Bianchi, A Ciferri, W. R. Krigbaum, "Equilibria of Extended-chain Polymers Exhibiting Crystalline and Liquid Crystalline Phases", J. Polym. Sci., Polym. Phys. Ed., 18, 2037-2053, (1980).

10. S. P. Papkov, "Liquid Crystalline Order in Solutions of Rigid Polymers", Adv. Polym. Sci., 59, 76-102 (1983).

11. M. M. Iovleva, S. P. Papkov, "Polymer Crystallosolvates - Review", Polym. Sci. U.S.S.R., 24, 236-257 (1982).

12. K. H. Gardner, R. R. Matheson, P. Avakian, Y. T. Chia, T. D. Gierke, "A Partial Phase Diagram and Crystal Solvate for the Poly(p-phenylene terephthalamide)/Sulfuric Acid System", Abs. Pap. ACS, 186(Aug), 37 (1983).

13. M Takase, W. R. Krigbaum, H. Hacker, "Poly(benzamide): Magnetic Field Orientation, Solvation and Crystal-Crystal Transformations", J. Polym. Sci., Polym. Phys. Ed., 24, 1115-1119 (1986).

14. M. Takase, A. Ciferri, W. R. Krigbaum, H. Hacker, "Poly(benzamide) II: Thermal Behavior and Crystal Transformations" J. Polym. Sci., Polym. Phys. Ed., 24, 1675-1682 (1986).

15. J. F. Wolfe, B. H. Loo, F. E. Arnold, "Rigid Rod Polymers 2. Synthesis and Thermal Properties of Para-Aromatic Polyamides with 2,6 Benzobisthiazole Units in the Main Chain", Macromol., 14, 915-920 (1981).

16. C. C. Lee, S. G. Chu, G. C. Berry, "Studies on Dilute Solutions of Rodlike Macroions, 1. Light Scattering, Densitometry and Cryoscopy", J. Polym. Sci., Polym. Phys. Ed., 21, 1573-1597 (1983).

17. D. B. Cotts, G. C. Berry, "Polycondensation of Poly([benzo(1,2-d:5,4,d')bisoxazole -2,6 diyl]1,4 phenylene)", Macromol., 14, 930-934 (1981).

18. C. R. Crosby, W. C. Ford, F. E. Karasz, K. H. Langley, "Depolarized Light Scattering of a Rigid Macromolecule Poly(p-phenylene benzobisthiazole)", J. Chem. Phys., 75, 4298-4306 (1981).

19. C. P. Wong, H. Ohnuma, G. C. Berry, "xx", J. Polym Sci., Polym. Symp., 65, 173-192 (1978).

20. S. Venkatraman, Studies on the Thermodynamics, Rheological and Rheooptical Properties of a Rigid Rod Polymer in Solution, Ph.D. Thesis, Carnegie-Mellon University, Pittsburgh (1981).

21. H. H. Tsai, Phase Equilibrium and Rheological Studies of Solutions of Rodlike Articulated Polymers and their Mixtures, Ph.D. Thesis, Carnegie-Mellon University, Pittsburgh (1983).

22. S. G. Chu, S. Venkatraman, G. C. Berry Y. Einaga, "Rheological Properties of Rodlike Polymers in Solution, 1. Linear and Non-linear Steady State Behavior", Macromol., 14, 939-946 (1981).

23. Y. Einaga, G. C. Berry, S. G. Chu, "Rheological Properties of Rodlike Polymers in Solution, 3. Transient and Steady State Studies on Nematic Solutions", Polym. J., 17, 239-251 (1985).

24. S. Venkatraman, G. C. Berry, Y. Einaga, "Rheological Properties of Rodlike Polymers in Solution, 2. Linear and Non-linear Transient Behavior", J. Polym. Sci., Polym. Phys. Ed., 23, 1275-1295 (1985).

25. S. R. Allen, A. G. Filippov, R. J. Farris, E. L. Thomas, C. P. Wong, G. C. Berry, E. C. Chenevey, "Mechanical Studies of High Strength, High Modulus Poly(p-phenylene benzobisthiazole) Fibers, Macromol., 14, 1135-1138 (1981).

26. E. J. Roche, T. Takahashi, E. L. Thomas, "Structure of High Modulus Fibers of Poly(p-phenylene benzobisthiazole)", in A. D. French, K. H. Gardner, eds., Fiber Diffraction Methods", ACS Symp. Series, 141, 303-313 (1980).

27. J. A. Odell, A. Keller, E. D. T. Atkins, M. J. Miles, "Structural Studies of Poly(p-phenylene benzobisthiazole) Films", J. Mater. Sci., 16, 3309-3318 (1981).

28. J. R. Minter, Structural Investigations of Fibers and Films of Poly(p-phenylene benzobisthiazole), Ph.D. Thesis, University of Massachusetts, Amherst (1982).

29. K. Shimamura, J. R. Minter, E. L. Thomas, "Lattice Imaging of High Modulus Poly(p-phenylene benzobisthiazole) Fibers", J. Mater. Sci. (Lett.), 2, 54-58 (1983).

30. T. Granier, E. L. Thomas, to be published.

31. S. R. Allen, Mechanical and Morphological Correlations in Poly(p-phenylene benzobisthiazole) Fibers, Ph.D. Thesis, University of Masachusetts, Amherst (1983).

32. L. A. Pottick, The Influence of Drying on the Structure and Mechanics of Poly(p-phenylene benzobisthiazole Fibers, Ph.D. Thesis, University of Massachusetts, Amherst (1986).

33. S. J. DeTeresa, Axial Compressive Strength of High Performance Polymer Fibers, Ph.D. Thesis, University of Massachusetts, Amherst (1985).

34. J. R. Minter, K. Shimamura, E. L. Thomas, "Microstructural Study of As-Extruded and Heat-Treated Ribbons of Poly(p-phenylene benzobisthiazole)", J. Mater. Sci., 16, 3303-3308 (1981).

35. S. R. Allen, R. J. Farris, E. L. Thomas, "High Modulus, High Strength Poly(p-phenylene benzobisthiazole) Fibers", J. Mater. Sci., 20, 4583-4592 (1985).

36. L. A. Pottick, R. J. Farris, "Alterations in the Structure and Mechanics of Poly(p-phenylene benzobisthiazole) Fibers due to the Collapse Process During Drying", TAPPI Nonwovens Symp. 65-71 (1985).

37. H. H. Frost, Microstructure and Phase Behavior of Poly(p-phenylene benzobisthiazole)/Methane-sulfonic acid Crystal Solvates, M.S. Thesis, University of Massachusetts, Amherst (1984).

38. Y. Cohen, H. H. Frost, E. L. Thomas, "Structure Formation and Phase Transformations in Solutions of a Rigid Polymer", accepted for publication in P. S. Russo ed., Reversible Gelation in Polymers, ACS Symp. Series (1987).

39. M. F. Perutz, "New X-Ray Evidence on the Configuration of Polypeptide Chains", Nature 167, 1053-1054 (1951).

40. C. Robinson, "Liquid Crystalline Structures in Solutions of a Polypeptide", Trans. Faraday Soc., 52, 571-592 (1956).

41. W. G. Miller, "Stiff Chain Polymer Lyotropic Liquid Crystals", Ann. Rev. Phys. Chem., 29, 519-535 (1978).

42. V. Luzzati, M. Cesari, G. Spach, F. Masson, J. M. Vincent, "La Structure du Poly-L-γ-Glutamate de Benzyle en Solution. Configuration en Helice Differente de l'Helice α et Transitions entre Formes Helicoidales", J. Mol. Biol., 3, 566-584 (1961).

43. P. Doty, J. H. Bradbury, A. M. Holtzer, "Polypeptides IV. The Molecular Weight, Configurations and Association of Poly(γ-benzyl-L-glutamate) in Various Solvents", J. Amer. Chem. Soc., 78, 947-954, (1956).

44. J. C. Powers, W. L. Peticolas, "Aggregation of Poly(γ-benzyl-L-glutamate) in Mixed Solvent Systems", Biopolym., 9, 195-203 (1970)

45. S. Chakrabarti, W. G. Miller, "Aggregation of Poly(γ-benzyl-L-glutamate)", Biopolym., 23, 719-734 (1984).

46. W. G. Miller, C. C. Wu, E. L. Wee, G. L. Santee, J. H. Rai, K. G. Goebel, "Thermodynamics and Dynamics of Polypeptide Liquid Crystals", Pure Appl. Chem., 38, 37-58 (1974).

47. D. Parry, A. Elliott, "The Structure of a Paracrystalline Phase of Poly(γ-benzyl-L-glutamate) in Dimethylformamide", J. Mol. Biol., 25, 1-13 (1967).

48. P. S. Russo, W. G. Miller, "On the Nature of the Poly(γ-benzyl-L-glutamate)-Dimethylformamide 'Complex Phase'", Macromol., 17, 1324-1331 (1984).

49. W. G. Miller, L. Kou, K. Tohyama, V. Voltaggio, "Kinetic Aspects of the Formation of the Ordered Phase in Stiff-Chain Helical Polyamino Acids", J. Polym. Sci., Polym. Symp., 65, 91-106 (1978).

50. W. G. Miller, S. Chakrabarti, K. M. Seibel, "Aggregation, Phase Behavior and the Nature of Networks Formed by some Rodlike Polymers", in P. L. Dubin, ed., Microdomains in Polymer Solutions, Plenum Press, New York (1985).

51. W. G. Miller, P. S. Russo, S. Chakrabarti, "Composition, Phase Behavior and Morphology in Poly(amino acids) Forming Lyotropic Liquid Crystals", J. Appl. Polym. sci., Appl. Polym. Symp., 41, 49-63 (1985).

52. S. Sasaki, M. Hikata, C. Shiraki, I. Uematsu, "Molecular Aggregation and Gelation in Poly(γ-benzyl-L-glutamate) Solutions", Polym. J., 14, 205-213 (1982).

53. S. Sasaki, K. Tokuma, I. Uematsu, "Phase Behavior of Poly(γ-benzyl-L-glutamate)", Polym. Bull., 10, 539-546 (1983).

54. A. K. Murthy, M. Muthukumar, "Dynamic Mechanical Properties of Poly(γ-benzyl-L-glutamate) Gels in Benzyl Alcohol", submitted to Macromolecules.

55. M. Doi, S. F. Edwards, "Dynamics of Rodlike Macromolecules in Concentrated Solutions", J. Chem. Soc., Faraday Trans. II, 74, 560-570 (1978).

56. M. Doi, S. F. Edwards, "Dynamics of Rodlike Macromolecules in Concentrated Solutions", J. Chem. Soc., Faraday Trans. II, 74, 918-932 (1978).

57. M. Doi, N. Y. kuzuu, "Non-Linear Viscoelasticity of Rodlike Macromolecules in Condensed State", J. Polym. Sci., Polym. Phys. Ed., 18, 409-419 (1980).

58. F. Rybnikar, P. H. Geil, " Fibrillar Aggregates of Poly(γ-benzyl-L-glutamate)", Biopolym., 11, 271-278 (1972).

59. J. J. B. P. Blais, P. H. Geil, "Fibrillar Polypeptide Aggregates", J. Ultrastruct. Res., 22, 303-311 (1968).

60. K. Tohyama, W. G. Miller, "Network Structure in Gels of Rodlike Polypeptides", Nature, 289, 813-814 (1981).

61. P. S. Russo, P. Magestro, M. Mustafa, M. J. Saunders, W. G. Miller, "Kinetics of Gelation of Rodlike Polymers by Light Scattering and Optical Microscopy Methods", Polymer Preprints, 27(1), 229 (1986).

62. A. R. Spurr, "A Low Viscosity Epoxy Resin Embedding Medium for Electron Microscopy", J. Ultrastruct. Res., 26, 31-43 (1969).

63. D. J. Kinning, Micelle Formation in Block Copolymer-Homopolymer Blends, Ph.D. Thesis, University of Massachusetts, Amherst (1986).

64. O. Kratky, I. Pilz, P. J. Schmitz, "Absolute Intensity Measurements of Small-Angle X-Ray Scattering by Means of a Standard Sample", J. Coll. Int. Sci., 21, 24-34 (1966).

65. I. Pilz, O. Kratky, "Absolute Intensity Measurements of Small-Angle X-Ray Scattering by Means of a Standard Sample, Part II", J. Coll. Int. Sci., 24, 211-218 (1967).

66. I. Pilz, "Absolute Intensity Measurements of Small-Angle X-Ray Scattering by Means of a Standard Sample, Part III", J. Coll. Int. Sci., 30, 140-144 (1969).

67. J. Dubochet, A. W. McDowall, "Vitrification of Pure Water for Electron Microscopy", J. Micros. (Oxford), 124, RP3-4 (1981).

68. Y. Talmon, H. T. Davis, L. E. Scriven, E. L. Thomas, "Cold Stage Microscopy System for Fast Frozen Liquids", Rev. Sci. Instr., 50, 698-704 (1979).

69. G. Perlov, Y. Talmon, A. H. Falls, An Improved Transfer Module and Variable Temerature Controller for a Simple Commercial Cooling Holder", Ultramicroscopy, 11, 283-288 (1983).

70. J. Dubochet, M. Adrian, J. Teixera, C. M. Alba, R. K. Kadiyala, D. R. McFarlane, C. A. Angell, "Glass Forming Microemulsions-Vitrification of Simple Liquids and Electron Microscope Probing of Droplet Packing Modes", J. Phys. Chem., 88, 6727-6732 (1984).

71. H. J. Purz, M. Schwalne, A. Buchtemann, J. Hartmann, "Some Methodological Aspects and Applications of Freeze-Etching in Polymer Research", Acta Histochimica, Suppl. Band XXIII,S, 89-109 (1981).

72. O. Glatter, O. Kratky, Small Angle X-Ray Scattering, Academic Press, New York (1982).

73. R. Perret, W.Ruland, "Single and Multiple X-Ray Small-Angle Scattering of Carbon Fibers", J. Appl. Cryst., 2, 209-218 (1969).

74. R. Perret, W. Ruland, Smal-Angle X-Ray Scattering of Non-Graphitizable CArbons", J. Appl. Cryst., 1, 308-313 (1968).

75. M. Dettenmaier, "Intrinsic Crazes in Polycarbonate: Phenomenology, and Molecular Interpretation of a New phenomenon", Adv. Polym. Sci., 52/53, 57-104 (1983).

76. E. Paredes, E. W. Fischer, "Rontgenkleinwinkel-Untersuchungen zur Struktur der Crazes (Fleisszonen) in Polycarbonat und Polymethylmethacrylat", Makromol. Chem. 180, 2707-2722 (1979).

77. H. R. Brown, E. J. Kramer, Craze Microstructure from Small-Angle X-Ray Scattering", J. Macromol. Sci. Phys., B19, 487-522 (1981).

78. P. Debye, A. M. Bueche, "Scattering by an Inhomogeneous Solid", J. Appl. Phys., 20, 518-525 (1949).

79. G. Oster, D. P. Riley, "Scattering fron Cylindrically Symmetric Systems", Acta Cryst., 5, 272-276 (1952).

80. P. Debye, H. R. Anderson, H. Brumberger, "Scattering by an Inhomogeneous Solid II. The Correlation Function and its Application", J. Appl. Phys., 28, 679-683 (1957).

81. G. Porod, "Die Rontgenkleinwinkelstreuung von Dichtgepackten Kolloiden Systemen" I. Teil, Kolloid-Z., 124, 83-114 (1951); II. Teil, Kolloid-Z., 125, 51-57 (1952); III. Teil, Kolloid Z., 125, 108-122 (1952).

82. R. Kirste, G. Porod, "Rontgenkleinwinkelstreuung an Kolloiden Systemen. Assymptotisches Verhalten der Streukurven", Kolloid Z. u Z. Polymere, 184, 1-7 (1962).

83. I. S. Gradshteyn, I. M. Rhyzik, Tables of Integrals, Academic Press, New York (1983), page 711.

84. A. Guinier, G. Fournet, Small-Angle Scattering of X-Rays, J. Wiley and Sons, New York (1955).

85. F. Zernike, J. A. Prins, "Die Bengung von Rontgenstrahlen an Flussigkeiten als Effekt der Molekulanordnung", Z. Physik, 41, 184-194 (1927).

86. P. Debye, "Zerstreuung von Rontgenstrahlen", Ann. Physik, 46, 809-823 (1915).

87. D. G. Chae, F. H. Ree, T. Ree, "Radial Distribution Functions and Equation of State of the Hard Disc Fluid", J. Chem. Phys., 50, 1581-1589 (1969).

88. L. S. Ornstein, F. Zernike, "Accidental Deviations of Density and Opalescence at the Critical Point of a Single Substance", Proc. Akad. Sci. (Amsterdam), 17, 793-806 (1914).

89. J. K. Percus, G. J. Yevick, "Analysis of Classical Statistical Mechanics by Means of Collective Coordinates", Phys. Rev., 110, 1-13 (1958).

90. Y. Cohen, E. L. Thomas, "Structure Formation During Spinning of Poly(p-phenylene benzobisthiazole) Fiber", Polym. Eng. Sci., 25, 1093-1096 (1985).

91. D. L. Misell, Image Analysis, Enhancement and Interpretation, North Holland, Amsterdam (1978).

92. W. Ruland, "Small-Angle Scattering of Two-Phase Systems: Determination and Significance of Systematic Deviations from Porod's Law", J. Appl. Cryst., 4, 70-73 (1971).

93. R. F. Jameson, "Polyphosphoric Acid", in A. V. Slack, ed., Phosphoric Acid, Vol. 1, Part 2, Marcel Dekker, New York (1968).

94. E. Thilo, "Condensed Phosphates and Arsenates", Adv. Inorg. Chem. Radiochem., 4, 1-75 (1962).

95. V. A. Kabanov, O. V. Kargina, L. A. Mishustina, S. Y. Lubanov, "A New Family of Crystallizable Polyelectrolyte Complexes", Makromol. Chem. Rapid Comm., 2, 343-346 (1981).

96. E. Tsuchide, K. Abe, "Interactions Between Macromolecules in Solution and Intermacromolecular Complexes", Adv. Polym. Sci., 45, 1-119 (1982).

97. K. E. W. Reihert, "Models of Coupled Cooperative Polymer Association and Protonation as Mediated by pK Shifts", Bio-electrochem. Bioenergetics, 8, 301-308 (1981).

98. S. Kozunori, G. C. Berry, "Nematic Solutions of Rodlike Polymers 1. Light Scattering from Nematic Solutions with Complex Texture, and Phase Separation in Poor Solvents", accepted for publication in P. S. Russo, ed., Reversible Gelation in Polymers, ACS Symp. Series (1987).

99. V. Luzzati, "Interpretations des Measures Absolues de Diffusion Centrale des Rayons X en Collimation Ponctuelle ou Lineare: Solutions de Particules Globulaires et Batonnets", Acta Cryst. 13, 939-945 (1960).

100. B. B. Mandelbrot, Fractals- Form, Chance and Dimension, W. H. Freeman, San Fransisco (1977).

101. M. Kolb, R. Botet, R. Jullien, "Scaling of Kinetically Growing Clusters", Phys. Rev. Lett., 51, 1123-1126 (1983).

102. P. Meakin, "Formation of Fractal Clusters and Networks by Irreversible Diffusion-Limited Aggregation", Phys. Rev. Lett., 51, 1119-1122 (1983).

103. L. D. Landau, E. M. Lifshitz, Statistical Physics, Pergamon Press, Oxford (1985).

104. J. W. Cahn, J. E. Hilliard, "Free Energy of a Non-Uniform System. I. Interfacial Free Energy", J. Chem. Phys., 28, 258-267 (1958).

105. F. P. Price, "Nucleation in Polymer Crystallization", in A. C. Zettlemoyer, ed., Nucleation, Marcel Dekker, New York (1969).

106. F. Family, D. P. Landau, Kinetics of Aggregation and Gelation, North Holland, New York (1984).

107. T. Witten, L. Sander, "Diffusion-Limited Aggregation- A kinetic Critical Phenomenon", Phys. Rev. Lett., 47, 1400-1403 (1981)

108. M. Muthukumar, "Mean Field Theory for Diffusion-Limited Cluster Formation", Phys. Rev. Lett., 50, 839-842 (1983).

109. P. Meakin, "Diffusion-Controlled Cluster Formation in Two, Three and Four Dimensions", Phys. Rev. A, 27, 604-607 (1983).

110. P. Meakin, "Effects of Cluster Trajectories on Cluster-Cluster Aggregation: A Comparison of Linear and Brownian Trajectories in Two- and Three- Dimensional Simulations", Phys. Rev. A, 29, 997-999 (1984).

111. G. Nicolis, I. Prigogine, Self Organization in Non-Equilibrium Systems, J. Wiley and Sons, New York (1977).

112. A. Nakajima, T. Hayishi, M. Ohmori, "Phase Equilibria of Rodlike Molecules in Binary Solvent Systems", Biopolym. 6, 973-982 (1968).

113. C. Cohen, G. B. Tanny, S. Prager, "Diffusion-Controlled Formation of Porous Structures in Ternary Polymer Systems", J. Polym. Sci., Polym. Phys. Ed., 17, 477-489 (1979).

114. E. L. Wee, W. G. Miller, "Lattice Model Treatments of Ordered Phases in Stiff Chain Polymer-Diluent Systems", in J. F. Johnson, R. S. Porter, eds., Liquid Crystals and Ordered Fluids, Vol. 3, Plenum Press, New York (1978).

115. M. Muthukumar, J. H. Ho, Private Communication.

116. E. Iizuka, "Properties of Liquid Crystals of Polypeptides, with Stress on the Electromagnetic Orientation", Adv. Polym. Sci., 20, 80-107 (1976).